Università di Bologna

Facoltà di Scienze Matematiche, Fisiche e Naturali

Dottorato di Ricerca in Geofisica

Ciclo XXI

Attenuation tomography of the main volcanic regions of the Campanian Plain

Dott. Luca De Siena
matr. n. 266425
Settore scientifico disciplinare: GEO/10

Esame finale anno 2009

Relatore:
Prof. Edoardo Del Pezzo

Referente:
Prof. Andrea Morelli

Coordinatore:
Prof. Michele Dragoni

Introduction

Imaging techniques applied to the study of the rocks composing the lithosphere are powerful tools for the interpretation of geological evidences as well as for the development of numerical models and for the exact determination of seismic risk. This is particularly true in tectonically active zones, like fault areas and volcanoes. The extreme heterogeneity of the seismic properties characterizing this media yields to difficult measures of the seismic attributes that must be employed in the inversion process. Velocity and attenuation tomographies are the two main tomographic techniques applied to image the Earth structure, both at small and large scales. As compared with velocity tomography, attenuation imaging is a complementary method that better resolves heterogeneity, and better constrain the interpretation in terms of lithologic characteristics of rock (De Lorenzo et al., 2001a, Hansen et al., 2004, Eberhart-Phillips et al., 2005). On the other hand, attenuation tomography is a much more difficult subject: the seismic attributes used to perform attenuation tomography usually require direct measures of wave amplitude in the time or frequency domains (Evans and Zucca, 1993, Rietbrock, 2001, Wu and Lees, 1996). S-wave attenuation tomography assumes a key role for a correct imaging of the structures beneath volcanoes, as S-waves are particularly sensitive to the presence of fluids like magmas or hydrothermal basins.

The main goal of this Ph.D. thesis is to develop new imaging techniques to be applied to the study of the attenuation of seismic body waves; the attention is particularly focused on the method used to retrieve seismic attributes from the seismic waveform amplitudes. Direct wave spectra are mainly influenced by source, path and site effect (Aki and Richards, 1980); the seismic attribute for attenuation tomography must be independent of the source and site terms in order to be used. For S-wave, this goal is achieved by using the Coda-Normalization (CN) method

(Aki, 1980a), a spectral ratio technique. The CN method divides the direct-S wave spectra with the S-wave coda (Sato and Fehler, 1998) measured at a given lapse time (the time elapsed from the onset of the seismic event). S-coda waves are the most prominent evidence for the short-wavelength random heterogeneity of the Earth, causing incoherent scattering of the direct-S waves (Zeng, 1996). Coda spectrum is affected by the same source intensity and site terms of direct-S wave spectrum (Tsujiura, 1978, Rautian and Khalturin, 1978). When the CN method is applied to single-path attenuation measures, associated with attenuation tomography, the site effects (and the source intensity) are completely removed, while the source radiation pattern is not (Aki, 1980a). Thus, in order to adapt the CN method to single-path measures of S-wave attenuation, the source radiation pattern must be removed from the spectral amplitude measures. To perform such a task the method developed in this Ph.D. thesis is based on the estimate of early-coda spectrum, mainly affected by forward scattering (Hoshiba, 1995, Gusev and Abubakirov, 1996, Gusev and Abubakirov, 1999): this modified CN method results to be independent of radiation pattern.

The development of a multi-resolution inversion scheme applied to the single-path measures of P- and S-wave attenuation, obtained with the classical (Scherbaum, 1990, Lees and Lindley, 1994) and CN methods, respectively, is the second main argument of this Ph.D. thesis. The inversion scheme, developed utilizing ideas coming from velocity tomography (Bai and Greenhalgh, 2005), is able to measure the attenuation parameters in blocks of different sizes, and, jointly, to constrain the data vector of the inversion scheme at higher resolution with the results obtained at lower resolution in order to obtain, when possible, a resolution comparable with the one of velocity tomography.

The P- and S-wave attenuation tomography results (ecspecially the S-wave results, obtained with the CN method) show that the techniques developed furnish a robust and stable image of total attenuation of high frequency body waves. Together with P- and S- velocity images, the attenuation images add further information for the correct interpretation of physical state of the rocks composing the highly heterogeneous media, possibly showing features that are not evident with the sole velocity tomography.

The studies described in this thesis yielded to the preparation of four articles (three already published and one submitted) on international journals: (Del Pezzo et al., 2006a, Petrosino et al., 2008, De Siena et al., 2008, De Siena et al., submitted to JGR).

Contents

Chapter 1

Seismic Wave Attenuation and Scattering

1.1 Attenuation

An earthquake produces elastic waves, starting from its hypocenter, following, as a first approximation, the laws of optical geometry (Aki and Richards, 1980). Let's consider an idealized, purely elastic Earth. First, the amplitude of a seismic pulse is affected by the geometric spreading. Then, the wave-front interacts with the boundaries and heterogeneity of the ongoing medium, producing reflected, refracted and surface waves, solutions of the elastic wave equation with particular boundary conditions (Lay and Wallace, 1995). In the real world, the amplitude of this waves is also influenced by the fact that the Earth is not perfectly elastic (Anderson, 1964): the mechanical behavior of a more or less saturated rock is assumed to be linear viscoelastic (Shon, 1996, Wei and Muraleetharan, 2007). Amplitude attenuation phenomena come from inelasticity of the Earth and from the inhomogeneities of the medium (Heinz and Jeanloz, 1983). Propagating waves attenuate with time due to various energy-loss mechanisms; the seismic energy is continuously employed in the heating of the propagation medium and in the making of secondary waves (Sato and Fehler, 1998). In both cases, the amplitude decrease is usually exponentially related to travel distance (Lay and Wallace, 1995).

The quantity used to parametrize attenuation is the total quality factor Q

(section 1.1.1). This quantity can be separated in an intrinsic and a scattering attenuation (section 1.1.2), parametrizing different attenuation processes. The frequency dependence of the total quality factor is discussed in section 1.1.3. A brief summary of the variations of Q into the Earth is given in section 1.1.4.

1.1.1 The total quality factor (Q)

In physics, the quality factor is a dimensionless parameter that compares the time constant for decay of an oscillating physical system's amplitude to its oscillation period. Equivalently, it compares the frequency at which a system oscillates to the rate at which it dissipates its energy. An higher quality factor indicates a lower rate of energy dissipation relative to the oscillation frequency, so the oscillations die out more slowly. For example, a pendulum suspended from a high-quality bearing, oscillating in air, would have a high quality factor, while a pendulum immersed in oil would have a low one. The concept originated in electronic engineering, as a measure of the 'quality' desired in a good tuned circuit or other resonator.

The concept of quality factor has been applied to seismology, and popularized in earth-sciences by the fundamental paper of Knopoff (1964), named "Q", where the basis of the theory overwhelming this quantity have been posed. The seismic total quality factor is a measure of how Earth rocks attenuate and disperse acoustic (seismic) energy. As an intrinsic property of rock, Q is the ratio of stored energy to dissipated energy, and is associated with a viscoelastic or a non-linear stress-strain constitutive relation for a material. Seismologists have had a long tradition of utilizing a quality factor for P-, S-, and coda-waves (respectively labeled Q_P, Q_S and Q_C), because this quantity can be actually related to the amplitude of a seismic wave.

Q is in principle dependent on frequency (Aki, 1980a), and can can be defined through the relative energy loss per cycle as:

$$\frac{1}{Q(\omega)} = -\frac{\Delta E}{2\pi E}, \tag{1.1}$$

where E is the peak strain energy stored in the volume. ΔE (≤ 0) is part of the energy lost in each cycle because of the anelasticity of the medium and the heterogeneities interacting with the wavefront, in the hypothesis $|\Delta E| << E$ (Aki and Richards, 1980).

Using the exact definition of ΔE, defining ΔE_R as the energy lost for the length ΔR, it comes out:

$$\frac{\Delta E}{\lambda} = \frac{\Delta E_R}{\Delta R}, \tag{1.2}$$

giving:

$$\frac{\Delta E_R}{E} = \frac{\Delta E \Delta R}{\lambda E} = -\frac{2\pi}{Q\lambda}\Delta R = -\eta \Delta R, \tag{1.3}$$

where λ is the wavelength and η is called "attenuation coefficient" (Lay and Wallace, 1995).

It is clear from (1.1) that the increase of the quality factor takes to a decrease of the dissipated energy. In the hypothesis of low anelasticity of the Earth filter ($Q > 100$), let's consider a monochromatic wave (e. g. characterized by a single frequency component). The energy of a wave train (seismogram) is proportional to the squared wave amplitude (Aki and Richards, 1980):

$$E = \chi A^2, \tag{1.4}$$

from which:

$$\frac{dE}{E} = \frac{2dA}{A}, \tag{1.5}$$

and approximating the differentials with the finite differences:

$$\frac{\Delta E}{E} \cong \frac{2\Delta A}{A} \cong -\frac{2\pi}{Q(f)} \Longrightarrow \frac{1}{Q} \cong -\frac{\Delta A}{\pi A}, \tag{1.6}$$

where ΔA is the amplitude variation per cycle and ΔE is positive.

If x is the spatial coordinate in any direction, it can be written:

$$\Delta A = \frac{dA}{dx}\lambda, \tag{1.7}$$

and using formula (1.7) in formula (1.6):

$$\frac{dA}{dx}\lambda = -\frac{\pi A}{Q}. \tag{1.8}$$

which can be solved to obtain A. Being $\lambda = vT = 2\pi v/\omega$, where v is the wave velocity, T is the period and ω the angular frequency, the amplitude is:

$$A(x, Q, \omega) = A_0 \exp(-\frac{\omega x}{2vQ}). \tag{1.9}$$

1.1.2 Intrinsic and scattering attenuation

Q-seismic is a dimensionless factor whose inverse (Q^{-1}) indicates the percentage of energy lost by a seismic wave due to various (and sometimes disputed) mechanisms of attenuation in the rock mass at many possible scales (Barton, 2006). The attenuation is mainly caused by scattering from geostructures of different scales, and by absorption in intrinsic micro-mechanisms. This mechanisms can be normal and shear micro-displacements across micro-cracks and joints, therefore involving friction to some degree, and relative micro-movement of fluids between the pore-space, the micro-cracks and the jointing of fracturing (Lay and Wallace, 1995).

The energy lost by anelastic dissipation in the propagation is usually measured with the intrinsic attenuation coefficient η_I, obtained using the amplitude decay of body and surface waves with time and frequency. The loose of energy due to heating of the medium is one of the principal causes of attenuation; an intrinsic quality factor, Q_I, can be defined, strictly dependent on the energy lost by anelastic dissipation, through the formula:

$$\frac{\Delta E_R^I}{E} = -\frac{2\pi \Delta R}{\lambda Q_I}. \tag{1.10}$$

The apparent frequency-independence of the total Q^{-1} at low frequencies was first used to model intrinsic absorption (Dziewonski, 1979, Jackson and Anderson, 1970). For seismic waves to remain causal in the presence of attenuation there must be frequency-dependent amplitude and phase changes (Aki and Richards, 1980).

Heat transfer is not the only cause of attenuation; scattering due to the heterogeneities distributed in the Earth also causes a decrease in the seismic energy with travel distance (Aki, 1980a), and a contemporary redistribution of the wave energy by reflection, refraction and conversion, generating secondary "coda" waves (Lay and Wallace, 1995, Sato and Fehler, 1998). Scattering phenomena depend on the size of the heterogeneities in the medium. Different phenomenologies, relatives to the different sizes of the heterogeneities, can be accounted for, and will be discussed in the following sections.

Here, the scattering quality factor, Q_{Sc}, a measure of the energy transferred from the primary wave to the scattered waves, is defined as a function of the mean free path. This quantity is seismologically defined as the mean path covered by a wavetrain before encountering a scattering centre. It is obviously dependent on the scattering centre density in the medium. Defining the numerical density of the scattering centers for unit volume, n_0, in order to parametrize the scattering, as well as the scattering cross-section, σ (Sato and Fehler, 1998) we obtain:

$$\frac{\Delta E_R^{Sc}}{E} = -\sigma n_0 \Delta R. \tag{1.11}$$

Thus, recalling formula (1.3), the scattering quality factor can be defined:

$$\frac{\Delta E_R^{Sc}}{E} = -\frac{2\pi}{\lambda Q_{Sc}} \Delta R = -\sigma n_0 \Delta R. \tag{1.12}$$

Scattering attenuation can produce both frequency-dependent and non-frequency-dependent effects (Jacobson, 1987). The Q_S^{-1} value predicted from the usual mean wave formalism (Born approximation) monotonously increases with frequency even in the high frequency limit (Sato and Fehler, 1998).

The intrinsic and scattering quality factors are generally assumed to be independent (Frankel and Wennerberg, 1987, Sato and Fehler, 1998). Thus, the total energy lost for the length ΔR (ΔE_R^T) is related to intrinsic and scattering quality factors by:

$$\frac{\Delta E_R^T}{E} = -(\frac{2\pi \Delta R}{Q_I \lambda} + \frac{2\pi \Delta R}{Q_{Sc} \lambda}) = -2\pi \frac{\Delta R}{\lambda}[Q_I^{-1} + Q_{Sc}^{-1}] = -2\pi \frac{\Delta R}{\lambda} Q_T^{-1}, \tag{1.13}$$

from which a simple relationships can be obtained:

$$Q^{-1} = Q_I^{-1} + Q_{Sc}^{-1}. \tag{1.14}$$

Determining the relative amount of attenuation caused by scattering and intrinsic absorption is important for understanding the wave propagation and attenuation phenomena in the heterogeneous lithosphere. In the past, the scattering attenuation in the 1–20 Hz frequency band was considered the main cause of attenuation for seismic waves (Aki, 1980a, Aki, 1982). Recent works (Yoshimoto and Jin, 2008) show that the ratio between scattering and total attenuation gets to 1/2 at about 5 Hz, indicating that scattering and intrinsic attenuation give the same contribution to the total attenuation at this frequency. This ratio decreases with increasing frequency, showing that intrinsic attenuation dominates over the scattering one for frequencies above 5 Hz. This trend is due to the different frequency dependence of Q_I^{-1} and Q_{Sc}^{-1}, as both decrease with frequency, but the decreasing rate is weaker for Q_I^{-1}.

Anyway the relative amount of intrinsic and scattering attenuation shows quite different trends from one area to another as the scattering attenuation is strongly dependent on the size of the heterogeneities that characterize the area. Many techniques have been developed with the aim of separating intrinsic and scattering attenuation. Starting from radiative transfer theory Wu (1985) was able to quantify the ratio of scattering loss to total attenuation, which is called seismic albedo. An improvement in the method used by Wu resulted in more reliable estimates of seismic albedo and Q^{-1}, that can be used to calculate the losses due to scattering and intrinsic absorption: the multiple lapse-time window analysis (MLTWA) (Fehler et al., 1992, Hoshiba, 1993). Yoshimoto et al. (2008) compile the contribution from intrinsic and scattering attenuation measured in various seismic regions by different investigations with this techniques. The MLTWA and other separation method have been applied to various Italian volcanic region (Bianco et al., 1999, Del Pezzo et al., 2001, Del Pezzo et al., 2006b) and in various parts of the Italian Peninsula (Bianco et al., 2002, Giampiccolo et al., 2004, Bianco et al., 2005). Results obtained by these authors show a low Q_{Sc}^{-1} and a relatively higher Q_I^{-1}, characterizing the lithosphere of the areas without volcanism. An opposite behavior was found in the volcanic areas of Vesuvius, Campi Flegrei and Etna, confirming the importance of the scattering phenomena in volcano seismology (Del Pezzo, 2008).

1.1.3 Frequency dependence of Q

Seismic wave attenuation has been measured in many rock types over wide ranges of physical conditions and frequencies, and by various techniques. Studies of crustal Q require data at shorter periods than those used for mantle studies; short-period waves are more likely affected by lateral variations in elastic and anelastic structure than are the longer-period waves used to study the mantle. The result of Q_P^{-1} and Q_S^{-1} measurements from various continental region of the world are shown in Sato and Fehler (1998).

In the 1960's, the seismologists considered attenuation coefficient η as a frequency dependent parameter, linearly growing with frequency, and assumed Q to be frequency independent. Despite many attenuation measurements which indicate a linear functional frequency dependence of absorption or constant Q^{-1} in sediments (Dziewonski, 1979), several theories do not predict such linear dependence. The primary justification for rejecting a first-power frequency dependence of attenuation is that it implies that seismic waves cannot propagate causally (Futterman, 1962). To satisfy the causality, the seismic waves should travel with velocity dispersion, but there is a lack of velocity dispersion measurements in sediments (Jacobson, 1987). In the 1970's important developments with regard to anelasticity of rocks were summarized by Brennan (1981) , who concluded that Q vary as a power of frequency, and that the anelastic behavior can be considered linear only at low strain. In addition, anelasticity decreases progressively with frequency (Brennan and Stacey, 1977), and the empirical measures of this dependency are dependent of the region where the experiment is done. In their fundamental works Rautian and Khalturin (1978) (for the Garm area in central Asia and the 2-12 Hz frequency band) and Aki (1980) (for the Kanto region in Japan and the 1-25 Hz frequency band) empirically found that Q shows a strong dependence on frequency. Q increases with frequency proportionally to f^y, where y is 0.5 in the Garm area and between 0.6 and 0.8 in Japan. In Mexico, Ordaz and Singh (1992) estimated $Q_S^{-1} \simeq 0.037 f^{-0.66}$ for $0.2 - 10$ Hz. Jackson and Paterson (1993) and many other authors concluded their experiments based on laboratory measurements asserting the linear dependence of Q_S^{-1} with ω^{-y}, where y was about 1/6. Starting from an assumption of Aki (1980), Kinoshita (1994) confirmed that Q_S^{-1}

shows a peaked structure in the high frequency range on the assumption that the geometrical spreading exponent is -1 (body waves), and found $Q_S^{-1} = 0.0077 f^{-0.7}$ for 2-16 Hz. Almost nothing is known of the nature of the frequency dependence of Q in oceanic region (Mitchell, 2005). Measures on the frequency dependence of attenuation have been made by different authors in different regions of the Italian Peninsula (e.g. Del Pezzo et al. (2006b) and Petrosino et al. (2008)), and will be discussed in the following chapters, particularly regarding the Campi Flegrei area. Despite of regional variations, it is clear that Q_S^{-1} is of the order of 10^{-2} at 1 Hz and decreases with increasing frequency to 10^{-3} at 20 Hz. The frequency dependence at $0.1 \sim 1$ Hz remains poorly understood as seismic measurements are difficult to make in this band (Yoshimoto and Jin, 2008). The frequency dependence of Q_S^{-1} can be experimentally considered as proportional to f^{-y} for frequencies higher than 1 Hz, the values of y ranging from 0.5 to 1. A similar decrease of Q_P^{-1} with increasing frequency is observed above 1 Hz. The ratio Q_P^{-1}/Q_S^{-1} is smaller than 1 under 1 Hz, and becomes larger than 1 above this frequency (Sato and Fehler, 1998).

1.1.4 Q into the Earth: global experimental investigations

The structure of the Earth has been extensively studied using seismic waves generated by natural earthquakes and man made sources (Sato and Fehler, 1998). An understanding of the attenuative properties of the Earth has two major motivations. First, as it was described in previous sections, seismic wave amplitudes are reduced as waves propagate through an anelastic medium, and this reduction is usually frequency dependent. Second, attenuation characteristics reveal much information, such as lithology, physical state, and degree of saturation of rocks. Thus, resolving anelastic attenuation, its spatial and depth variations, can provide important constraints on the composition and dynamics of the Earth. The phenomenon of attenuation is much more complex than the elastic aspects of seismic wave propagation (Shon, 1996): measuring Q is difficult because of interfering non-linear elastic effects which contribute to the amplitudes of seismic waves (Anderson and Hart, 1978).

Seismic wave attenuation decreases with increasing rock cementation and depth, showing an opposite behavior respect to seismic wave velocity (Johnston, 1981). There is a general agreement that lateral variations of Q are strongest in the crust and the uppermost mantle, where they correlate with past and present tectonic activity (Karato, 2001). The recent progress in the determination of global Q-structure in the Earth using seismic data allowed the 1D profile of Q, which appears to be reasonably well constrained in the upper-mantle and transition zone (Mitchell, 2005), less so in the lower mantle (Anderson and Hart, 1978, Stacey, 1995).

The first estimates of Q_S from seismic data were reported by Press (1957) on a global scale. He compared the relative amplitude of multiple ScS phases and concluded that the Q_S of the whole mantle was of order of 500, for the period range 14 - 70 s. Anderson and Kovack (1964) and Kovack and Anderson (1964) used a larger data-set, estimating $Q_S = 600$ for the whole mantle and $Q_S = 200$ for the upper mantle and transition zone. The maximum departure from perfect elasticity occurs in the region of the upper mantle from 100 to 400 km depth (Anderson, 1964): the same authors estimate the lower mantle Q_S to be about 2200. There are a number of models showing a higher Q in the lithosphere over a lower Q in the asthenosphere. The characteristic features of Q_S models are the rapid decrease in Q_S between depths of 60 to 150 km, and the slower increase in Q_S between depths of 200 and 400 km (Fuchs, 1997). Q_S of different models vary by as much as a factor of 10 in the upper mantle at depths reaching 200 km (Mitchell, 2005). Anderson and Hart (1978) proposed Q models of the whole Earth, having $Q_S^{-1} \cong 0.002$ and $Q_P^{-1} \cong 0.0009$.

The 3-D Q distribution in the crust is much more easy to be obtained than the one of the mantle or the core. Anderson et al.(1965) in their MM8 model proposed a low frequencies Q_P^{-1}/Q_S^{-1} ratio of 0.4-0.47. Teleseismic and regional attenuation studies commonly find that S-waves are more attenuated than P-waves (Romanowicz and Durek, 2000) in the crust. Data recorded in deep boreholes (800 m to 2500 m) seismograms, however, find the opposite result for ray paths that sample the seismogenic crust: P-waves are more strongly attenuated than S-waves (Imanishi et al., 2004). The difference in Q_S/Q_P in the borehole, regional, and teleseismic studies reflects the depth dependence of attenuation in the crust. It has long been known from studies of fundamental-mode surface waves (Mitchell, 2005), as well as from regional phases (Aki, 1980a), that seismic attenuation is related to the degree of tectonic activity in continents, tectonically active regions being characterized by lower Q than stable regions. Regional variations of Q in the upper crust are actually and most easily explained by the movement of fluids in cracks that are abundant during and following periods of deformation and that decrease in number with time following the deformation (Mitchell, 2005). The fluids may be present because of metamorphic reactions that were produced by elevated temperatures from frictional heating or internal deformation (Newton, 1989). After the cessation of deformation, fluids will be slowly lost either by migration to the surface or by retrograde metamorphisms, cracks will close, and Q will increase.

Q has been used as a direct indicator of the presence of hydrocarbons, among other uses (Bourbie, 1985). Estimation of attenuation of pressure and shear waves is as important as the estimation of interval velocities in the field of seismic data interpretation. These estimates also provide an additional perspective of the lithology (rock mineral composition) and reservoir characteristics (rock pore space fluid content, fluid composition, fluid pressure and rock permeability to fluid flow) (Shon, 1996, Barton, 2006). A combined interpretation of velocity and total quality factor can be vital to investigate how material heterogeneity relates to subduction processes (Eberhart-Phillips et al. 2005), while the correct estimates of attenuation greatly improves the estimates of fault-plane direction, rupture velocity and seismic hazard (Watanabe and Sassa, 1996, Badawy and Fattah, 2001). In volcano seismology the presence (or the absence) of high attenuation of seismic waves below the volcano-structures may be attributed to the presence (or the absence) of magma and partial melting of rocks (Shapiro et al., 2000, Hansen et al. 2004). Large attenuation of high-frequency seismic waves may affect the estimates of the seismic hazard. The intrinsic loss of seismic wave energy, or seismic intrinsic attenuation, provides a proxy for temperature under certain conditions (Stachnick, 2004, De Lorenzo et al. 2001a).

The quality factor of the mantle is considerably more sensitive to temperature than elastic velocity, as shown by laboratory and theoretical studies and this sensitivity differs from that of elastic velocity (Jackson, 1998). The Arrhenius law, which masters the sensitivity of Q to temperature, implies that attenuation tomography should be able to resolve hot regions (high attenuation) better than elastic tomography. In addition, elastic velocity can be affected to a large degree by compositional variations, so, ultimately, mapping regions with various degrees of agreement between velocity and attenuation distributions help us constrain the distribution of chemical versus thermal heterogeneity in the shallow and deep mantle (Romanowicz and Durek, 2000).

The study of lateral variations in Q in the upper mantle at the global scale is generally addressed using isolated phases in the seismogram (for example fundamental mode surface wave spectra), which limits the sampling and therefore the resolution of Q structure that can be achieved. To measure attenuation in the deep mantle, one can use either low frequency surface wave and free-oscillation data, or deep turning body-wave data (Gung and Romanowicz, 2004). The use of isolated phases has the advantage of working directly with amplitudes, thus making it easier to detect contamination of the anelastic attenuation signal by elastic focusing and scattering, a key problem in attenuation tomography. Recent progress on a waveform modeling approach allows to work with entire seismograms and exploit the information contained both in fundamental mode surface waves, overtones and body waves (Romanowicz and Durek, 2000). These measurements fit waveforms significantly better when the frequency dependence of Q is taken into account, and, in the mantle, frequency dependence lies close to laboratory values (Stachnick, 2004).

Only few studies have proposed 3-D tomographic images of the deeper parts of the mantle and the core. While significant lateral variations are well documented, and appear to correlate with those of elastic heterogeneities, large uncertainties remain in the amplitudes of the lateral variations and their details (Romanowicz and Durek, 2000). Researchers used η measurements from individual P and PP spectra to invert for a frequency independent Q model, and find that the upper mantle is 5 times as attenuating as the lower mantle (Warren and Shearer, 2002). The majority of results of seismic attenuation can be attributed to the lateral variation in temperature when the effects of anelasticity is properly included: neither chemical variation nor partial melting is required in the majority of the lower mantle (Jackson, 1998). However, geophysical anomalies near the bottom of the lower mantle require chemical heterogeneity, in a layer confined to a very deep portion of the lower mantle (Karato, 2001). Waveform modeling suggests two different types of models for the two "hemispheres" of the top of the inner core, with a model in the eastern hemisphere having an average Q_P value of 250, and a model in the western hemisphere an average Q_P value of 600 (Wen and Niu, 2002).

In contrast to the liquid outer core, the Earth's inner core is mostly solid, and its composition is more pure iron. Based on dynamic arguments related to the freezing process of the inner core, and the observation of much lower P-wave quality factor in the inner core than in the outer core, it has been suggested that a mushy layer with liquid inclusions may exist at the top of the inner core (Cao and Romanowicz, 2004). Observations of high frequency PKnKP waves, multiply reflected by the underside of the core-mantle boundary, place a lower bound of 10^4 on the Q of the outer core. This is consistent with the expected behavior of a low viscosity fluid (Cormier and Li, 2002). In contrast to the outer core, a mean Q at 1 Hz of 307 is determined for the inner core by (Li and Cormier, 2002), using waveform modeling of PKIKP in the distance range 130° to 180°. A strong depth dependence of Q is observed, with attenuation much stronger in the upper 300 km of the inner core (Niazi and Johnson, 1992). Observations of the backscattered coda of PKiKP suggest that a significant fraction of the attenuation in the short-period (1 Hz) band may be due to scattering. The depth dependence of attenuation inferred from a scattering mechanism is roughly similar to that inferred from a viscoelastic mechanism, except a more abrupt transition is seen between higher attenuation in the upper inner core and lower attenuation in the lower inner core. Scattering attenuation is the predominant mechanism of attenuation in the inner core in the 0.02–2 Hz frequency band (Cormier and Li, 2002).

1.2 Scattering phenomena into the Earth: early and late coda

Seismic scattering is a process in which a primary wave interacts with a heterogeneity of the medium and produces new secondary waves. The energy of direct high frequency seismic waves, propagating from local earthquake, is strongly influenced by scattering phenomena. Scattering (as attenuation) is not explicable without accepting lateral heterogeneity (Sato, 1977). The main effect of scattering on high frequency seismic waves in the lithosphere is the presence of coda waves (section 1.2.1). The high sensitivity of these waves to the details of source and path effects increases their importance; for the same reason, the effect of path heterogeneity increases the difficulties in their study. The latter problem motivated the development of new models, designed to deal with seismic waves in a laterally heterogeneous medium (section 1.2.2); among them the Zeng multiple scattering model (1996) is the one which more efficiently describes scattering phenomena into the Earth. Experimental methods have been developed, using coda waves phenomenological properties, to remove source, site or path effects from the direct S-waves energy (section 1.2.3): the coda-normalization (CN) method (section 1.2.4) is widely the most useful and utilized tool for this sake (Sato and Fehler, 1998). Its application to attenuation tomography, in the following chapters, is based on the fundamental work of Aki (1980a), who first applied this technique to the average attenuation factor of the Earth and on the phenomenological properties of the early coda (section 1.2.5).

1.2.1 Main effect of scattering on high frequency seismic waves: Coda Waves

The Earth lithosphere properties are randomly varying in time and space (Aki and Richards, 1980); the high frequency seismic waves in such a medium vary randomly both in amplitude and in phase. They have to be described in terms of statistical averages and probability density. The portion of seismograms of local earthquake following the passage of all primary waves, where this phenomena are more evident, is typically a wavetrain whose amplitude decreases with increasing time. This wavetrain is commonly known as P- and S-wave coda (Aki, 1969). The term coda waves is commonly used to indicate the S-coda wave. Aki (1969) and Aki & Chouet (1975) first described the observable properties of coda waves for earthquakes having distance from station less than 100 km, interpreting them as generated by the scattering of the S-waves on the small scale heterogeneity into the medium. The most important experimental properties of this waves can be summarized with the following points:

1. the spectral content of coda waves at large lapse time t (the time elapsed from the origin time) is independent of source station direction.
2. the total length of the seismogram, calculated from the P-wave onset, is a valid measure for the estimate of seismic magnitude.
3. the coda power spectrum for different small magnitude (< 6) earthquakes is a function of lapse time, having the same frequency shape independently of the epicentral distance.
4. coda waves amplitude is dependent on the local geology of the registration site.

The main formula in coda wave analysis is:

$$P(\omega \mid t) = S(\omega) C(\omega \mid t) \tag{1.15}$$

where $P(\omega \mid t)$ is the power running spectrum of the coda for the angular frequency ω at lapse time t, the time measured from the origin time of the earthquake. $S(\omega)$ is the source spectrum and $C(\omega \mid t)$ represents the effect that a large geographical area surrounding the source has on the propagation of the waves. $C(\omega \mid t)$ is both independent of distance and details the path connecting source and station. Numerous studies demonstrated that, in formula (1.15), a term representing the recording site response, $R(\omega)$, can also be included (Sato and Fehler, 1998):

$$P(\omega \mid t) = S(\omega) R(\omega) C(\omega \mid t) \tag{1.16}$$

for lapse-time t grater than about twice the travel time of S waves, Δt_S.

After 1975, various observations studied coda waves site factors as well as their dependence on frequency and lapse time. Tsujiura (1978) evidenced that the site effect for direct-S and coda waves was the same in the frequency range 1–25 Hz in the Kanto region; moreover, the spectral content at large lapse times was the same at different stations. Rautian & Khalturin (1978) recognize that the temporal decay of the coda amplitude is independent of magnitude, for small (<6) magnitude earthquakes, for lapse time starting at twice Δt_S.

In the "early-coda" (Gusev and Abubakirov, 1999) the effects of the source radiation pattern can distinguished, whereas in the late coda those effects vanish (see also section 2.2.2). The "early coda" starts immediately after the direct-S wave, ending at about twice the S wave travel-time; the "late coda" starts approximately after $1.5 - 2$ times the S wave travel-time from source to receiver. The late S coda waves are composed of wavelets leaving the source region in a variety of directions (Sato and Fehler, 1998).

In the following section, the most general available model to explain the generation of coda-waves will be described (Zeng, 1991, Hoshiba, 1995, Zeng, 1996). Anyway, regardless of the scattering model, the total scattering coefficient g_0 always parametrizes the intensity of coda. g_0 does not allow to distinguish between a small number of strong scattering centers and a large number of weak ones (Sato, 1977).

The formulation commonly used by different researchers and resumed by Sato and Fehler (1998) in his fundamental textbook, models the Earth lithosphere as an homogeneous background media having propagation velocity V_0, filled with distributed point-like scatterers with number density n. J_0 is the energy flux density of an incident wave which produces a scattered spherical outgoing wave with energy flux J_1. The differential scattering cross-section for a given solid angle $d\Omega$ element at a given distance r is:

$$\frac{d\sigma}{d\Omega} = \frac{J_1 r^2}{J_0}. \tag{1.17}$$

Aki and Chouet (1975) define the scattering coefficient, or scattering power per unit volume, as

$$g = 4\pi n \frac{d\sigma}{d\Omega}, \tag{1.18}$$

which can be used as the only measure to characterize the scattering power.

The total scattering coefficient g_0 is defined as the average of g over all directions:

$$g_0 = \frac{1}{4\pi} \oint g d\Omega = n\sigma_0 = l^{-1} = Q_{Sc}^{-1} k, \tag{1.19}$$

where σ_0 is the total scattering cross-section, l is the mean free path and k the wavenumber.

1.2.2 Models of coda wave excitation

Random media may be grouped into three categories: random scatterers, random continua, and rough surfaces. The first one must be studied, in order to describe efficiently the scattering of seismic waves on the heterogeneities into the Earth. The characteristics of the real Earth heterogeneities must account for multiple scattering effects (Gao et al., 1983).

Zeng et al. (1991a,b) formulated the scattered wave energy formula, which extends the stationary energy transport theory described by Wu (1985) to the time dependent case. Scattered wave energy propagation in a random isotropic scattering medium is implemented for the seismic case, starting from the work of Ishimaru (1987). Zeng (1991) obtained a general solution of temporal variation of scattered energy density as Neumann series expansion, with each term characterized by a power of scattering coefficient η_{Sc}. The first-order term gives the wave energy scattered once from all possible scatterer points $\mathbf{r}_1$ to the receiver point $\mathbf{r}$. That is the formula used in the single scattering model (Sato, 1995).

The complete multiple scattering model formulated by Zeng (1991) assumes an impulsive spherical source. The scattered wave energies in a 3-D elastic medium with unperturbed velocity v and randomly distributed scatterers are additive. The energy formula at time t can be written as:

$$\begin{aligned} E(r,t) &= E_{in}(\mathbf{r}_0,\mathbf{r},t-\frac{|\mathbf{r}-\mathbf{r}_0|}{v})\frac{e^{-\eta|\mathbf{r}-\mathbf{r}_0|}}{4\pi\left|\mathbf{r}-\mathbf{r}_0\right|^2} \\ &\quad + \int_V \eta_{Sc}E(\mathbf{r}_1,t-\frac{|\mathbf{r}_1-\mathbf{r}|}{v})\frac{e^{-\eta|\mathbf{r}_1-\mathbf{r}|}}{4\pi\left|\mathbf{r}_1-\mathbf{r}\right|^2}dV_1 \end{aligned} \tag{1.20}$$

The source is located in $\mathbf{r}_0$, while the receiver point is in $\mathbf{r}$. The first term on the right-hand side is the incident wave energy. The second term is the sum of all the incoherent wave energies generated by the incident wave. The vector $\mathbf{r}_1$ indicates all possible scatterer points. In this scattering medium the scattered wave energy is expressed as the product of different factors. This factors are the scattering cross section, σ, the energy density at the scattering point, $E(\mathbf{r}_1,t-\frac{|\mathbf{r}_1-\mathbf{r}|}{v})$, and the total attenuation, including geometrical attenuation, $\frac{e^{-\eta|\mathbf{r}_1-\mathbf{r}|}}{4\pi|\mathbf{r}_1-\mathbf{r}|^2}$. The parameters used to describe the incident wave energy dissipation are also the geometrical spreading and attenuation.

Paasschens (1997) and Zeng (1991) found different analytical approximations of formula (1.20). Using numerical examples Zeng et al. (1991) showed that multiple scattering becomes very important as the scattering coefficient increases. The single scattering model (Sato, 1977) is able to describe scattering phenomena in case of very low scattering, the diffusion formula describes the other extreme of the radiative transfer theory: the strong multiple scattering case (Weaver, 1990, Zeng et al., 1991). The diffusive solution was used to explain the seismograms recorded on the Moon (Nakamura, 1970), the late coda of local earthquakes (Margerin et al., 1998) and seismograms recorded on volcanoes (Wegler, 2004).

In the above models the scatterers are always considered as point-like heterogeneities, but the linear dimension of the heterogeneities in the crust spans eight order of magnitude, and have different effects on the seismic waves (Wu and Aki, 1988). When a wavefront is incident upon a scatterer, different phenomenologies can be defined considering the relative dimensions between the incident wave length end the heterogeneity (or scatterer). Defining with a the mean dimension of the heterogeneity and with k the incident wave number their relation defines the scattering range. If $ka \cong 1$ it is called the Mie scattering; the effects of this kind of scattering range on propagating waves are strong. If $ka < 1$ the so-called Rayleigh scattering is characterized by a linear dependency between scattered power and k^2. If $ka << 1$ the wave does not see any obstacle, travelling like in an homogeneous medium.

1.2.3 Application of coda techniques to the measure of different seismological quantities

The most widely used coda measurements is the determination of earthquake magnitude from the S-coda duration (Sato and Fehler, 1998). The logarithm of the lapse time measured from the P-wave onset for local earthquakes is actually proportional to the magnitude of the event. Coda waves have been used to measure source function (Mayeda and Walter, 1996) as well as to discriminate the quarry blasts from earthquakes (Su et al., 1991). They are also a useful tool for mapping site amplification effects (Malagnini et al., 2004), as well as to study the heterogeneity of the Earth (Li et al., 2002, Li te al. 2004). Coda waves are commonly used to estimate the attenuation quality factors with array or single station techniques (Aki, 1980a, Mayeda et al., 1992). The time variations in the shape of the coda envelopes are associated with the time variations of the elastic properties and hence with the changes in the stress field acting on an area (Snieder, 2006). In addition, scattering causes a broadening of the pulse width with increasing travel distance while it preserves the high-frequency content of waveform. The pulse broadening around the direct S wave was explained by Abubakirov and Gusev (1990, see also section 2.2.2) using the forward scattering approximation (large angle between incident and scattered wave direction). Such a modulation effect has been studied as a tool for characterizing random media (Lerche and Menke, 1986) and as a way to measure attenuation parameters (De Lorenzo et al., 2001b).

A new inversion method of coda waveforms from local earthquake has been used to localize the not homogeneous spatial distribution of scattering coefficient in the crust and upper mantle (Nishigami, 1991); with this method strong correlation between the major active faults and the presence of strong scatterers has been demonstrated (Nishigami, 2006). Nishigami's technique has been used to construct an image of the distribution of the scattering coefficient in the medium, that is commonly called scattering tomography (Tramelli et al., 2006). Back-scattering tomography can be considered as an extension of the techniques used in reflection seismology. Reflection seismology considers wavelets reflected by discontinuities; scattering imaging, instead, assumes isotropic scattering and locate the position of the scatterers emitting more energy (Tramelli, 2008). In Italy, La Rocca et al. (2001) analyzed the seismograms from explosive sources recorded from an array located on Mt. Vesuvius. They found a high concentration of scatterers in and around the volcanic edifice, suggesting that topographical irregularities play an important role in the generation of the scattering phenomena.

Regional measurements of Q_C^{-1} (the coda quality factor) have been correlated to total attenuation by Aki (1980), who measured Q_C^{-1} and Q_S^{-1} in Kanto region, Japan. Generally, active regions are characterized by low values of Q_C^{-1} and strong frequency dependence (Matsumoto, 1995). Several experiments and theoretical studies reported that, for large lapse-time, Q_C^{-1} corresponds only to the intrinsic absorption (Frankel and Clayton, 1986, Shang and Gao, 1988, Matsunami, 1991).

More recently, several studies bound Q_C^{-1} values between Q_I^{-1} and Q^{-1} (Hoshiba, 1993, Jin et al., 1994, Mayeda et al. 1992). Both g_0 and Q_c^{-1} were used to monitor the temporal change in the coda characteristics. The temporal changes of Q_C^{-1} have been used as precursors of earthquake and eruptions (Jin and Aki, 1986, Sato and Fehler, 1998, Hong and Wu, 2005).

Coda waves have been recently used to retrieve Green functions in the medium (Campillo and Paul, 2003). The late seismic coda contains coherent information about the elastic response of Earth. The correlations of the seismic codas of different distant earthquakes were recorded at stations that were tens of kilometers apart. By stacking cross-correlation functions of codas, Campillo and Paul (2003) found a low-frequency coherent part in the diffuse field. The extracted pulses have the polarization characteristics and group velocities expected for Rayleigh and Love waves, and the set of cross-correlations has the symmetries of the surface-wave part of the Green tensor. This phenomenon is due to the diffusive properties of random incoherent media, like the ones of ultrasonic waves (Weaver and Lobkis, 2006). Diffuse waves produced by distant sources are sufficient to retrieve direct waves between two perfectly located points of observation (Derode et al., 2003). Following the studies on coda waves, random fields, and particularly noise have been applied in other fields. The application of coda and noise cross-correlation to retrieve Green function represents the new frontier in the field of velocity tomography and volcanic eruptions forecasting (Brenguier et al., 2007, Brenguier et al., 2008).

1.2.4 Coda-normalization Method

Coda waves provide a reliable way to separate source, site and propagation effects from the seismic signal: the coda-normalization (CN) method. The CN method can estimate important physical parameters. It is the most widely used method regarding coda waves; it is based on the empirical observation that the coda energy is uniformly distributed within a region surrounding the source for wide lapse times (Rautian and Khalturin, 1978). The limits of this assumptions can be investigated in the matter of multiple scattering, which dominates at greater lapse-time. The "energy-flux" model (Frankel and Wennerberg, 1987), describing the spatial and temporal distribution of the seismic radiation energy density, is consistent with this assumption. Anyway, the CN method is a totally empirical method, so it is not based on any of the propagation models in the Earth, described in section 1.2.2.

Average path effects measured using CN method

The application of the coda-normalization method to attenuation tomography, described in chapter 2, requires a brief description of the work of Aki (1980a); this author used the phenomenological observations on coda waves discussed by several authors to measure the average S-waves quality factor of an extended area in Japan in a wide frequency range. The Aki's method was designed to normalize the source spectral amplitude using coda spectra at some fixed lapse time, using single station data. Later Yoshimoto et al. (1993) extended the method to measure the attenuation of the direct P-waves with travel distance.

A displacement signal $u_{i,j}(t)$ (referred to the i-event and j-station) can be factorized in a convolution of three fundamental factors (Herraiz and Espinosa, 1987):

$$u_i(t) = W_i(t,\theta) * N_j(t,\theta) * P(t,Q,v), \tag{1.21}$$

where $W(t,\theta)$, $N(t,\theta)$ and $P(t,Q,v)$ are respectively the source, site and propagation contributions, and v is the wave velocity. The angle θ is referred to the source-station direction in a given reference system. According to the Fourier Transform properties, the relationship (1.21) becomes a simple product in the frequency space. In particular, taking into account formula (1.9) to parametrize the frequency dependent path-attenuation for S-waves, formula (1.21) may be written:

$$u_i^S(f) = W_i^S(f,\theta)\frac{r}{r_0}N_j^S(f,\theta)\frac{\exp(-\pi f r/Q_S v)}{r}, \tag{1.22}$$

where r is the radius of the spherical wave and r_0 the radius at the source where the radiation first began, i.e. the critical distance for the far field condition (Shearer, 1999). The quality factor and the source spectra are considered frequency independent quantities. In the assumption $t > 2t_S$ (lapse-time more than twice the S-wave arrival time), the coda spectral amplitude is, in analogy with the

S-wave spectrum:

$$u^C(f) = W^C(f)N^C(f)P(f,t_c), \tag{1.23}$$

where the three coda factors are independent of the source-station direction.

Aki (1980a) assumed that:

1. for his database the quantity $\ln(W_i(f,\theta)/W_i^C(f))$ becomes independent of θ, after averaging on an adequate number of events, localized in a wide area around stations.
2. the same hypothesis states for the quantity $\ln(N(f,\theta)/N^C(f))$.

The spectral ratio of S and coda spectrum, averaged over events whose distance from the station is in the interval $[r-\Delta r, r+\Delta r]$, $\left\langle \frac{\ln(u_i^S(f))r}{\ln(u_i^C(f))} \right\rangle_{r\pm\Delta r}$,is defined by:

$$\left\langle \frac{\ln(u_i^S(f))r}{\ln(u_i^C(f))} \right\rangle_{r\pm\Delta r} = a(g_0, Q_C) - \frac{\pi f}{Q_S v} r. \tag{1.24}$$

A simple linear fit gives both the average quality factor of the area and the frequency independent constant $a(g_0, Q_C)$.

Source and site effects measured using CN method

The coda normalization method can be easily applied to the estimate of source and site amplification factors, that, on the contrary, at regional distances, usually relay only on the use of direct P- or S-waveforms. At lapse time t large enough the energy is uniformly distributed in a volume surrounding the seismic source. If this volume contains two recording site, the relative amplitude of the seismograms recorded at the two sites should be the same except for the influence of the near-recording site amplification (Sato and Fehler, 1998). The relative amplitude of the coda spectra at the sites h and l, for the earthquake i, can be expressed as:

$$\frac{u_{i,h}^C(\omega, t_c)}{u_{i,l}^C(\omega, t_c)} = \frac{N_h^C(\omega)}{N_l^C(\omega)} \tag{1.25}$$

where $u_{i,j}^C(\omega, t)$ is the coda amplitude of the i-th event registered at the j (or k)-th station. Using formula (1.25) and defining a "reference site" one can measure the "relative amplitude" of different sites respect to this one. The coda amplitude is usually substituted with the bandpass filtered coda envelope, calculated using the Hilbert transform, to obtain a more robust measure. Tsujiura (1978) first used this method, demonstrating that the relative site amplification calculated with this method equals the one calculated using the S waves. Phillips and Aki (1986) presented a method for inverting relative amplitudes determined at a suite of sites using a series of time windows to measure a site amplification factor for each site in an array. Assuming a common shape in the coda decay curves for all sites and sources, they developed an expression relating source factor, site amplification factor and the shape of the common decay curve. They also observed, for a few station, a lapse time dependence of the site function; this is one of the first observation of the so called "coda localization" phenomena (Aki and Ferrazzini, 2000, Wegler and Luhr, 2001). An increased amount of energy, trapped near the recording site, causes the violation of the basic assumptions of the coda normalization method, which is not applicable on this sites. First maps of site amplification factors obtained using coda-normalized spectra were built by Mayeda et al. (1991).

The coda normalization method provides an easy method to characterize the spectral differences in source radiation among seismic sources without requiring knowledge of source radiation pattern or propagation effects (Sato and Fehler, 1998). The expression used to retrieve the relative seismic moment, or magnitude, is similar to the one used to measure site effects, using two different events recorded at the same site:

$$\frac{u^C_{i,j}(\omega,t)}{u^C_{k,j}(\omega,t)} = \frac{W^C_i(\omega)}{W^C_k(\omega)} \tag{1.26}$$

where $u^C_{i,j}(\omega,t)$ is the amplitude at lapse time t_c of the seismogram recorded at the site j for the i (k)-th event. A "reference" source must be chosen, in order to measure the "relative moment" of different sources respect to this one. A coda-amplitude vs. seismic moment scale for Alaska was first developed by Biswas and Aki (1984) (Biswas and Aki, 1984). Mayeda and Walter (1996) showed that there is a more consistent relationship between the measurement made on coda waves respect to the ones made with the direct waves even though there is a large station separation of 500 km. Important applications of the CN method have been made to distinguish between explosions and natural earthquake (Su et al. 1991).

1.2.5 The radiation pattern dependency: early-coda properties

Radiative transfer is often introduced as a phenomenological theory; however, in condensed matter physics, radiative transfer emerges as a rigorous consequence of correlation theory (Margerin, 2006). The effects of the random medium on wave propagation can actually be described in terms of "coherence time" and "coherence bandwidth". A wave propagated at frequency f in a random medium produces, in general, a wave fluctuating in time. The correlation of the output waves at two different times t_1 and t_2 decreases as the separation $t_1 - t_2$ increases. The time difference Δt at which the correlation decreases to a specified level is called "coherence time", which describes how a wave at frequency f is correlated in time. The inverse of the coherence time is the "spectrum broadening" of a wave in a random medium (Ishimaru, 1997). It can be defined separating a random field $u(r, t)$ of position r and time t in a sum of an average field $\langle u(r, t)\rangle$ and a fluctuating field $u_f(r, t)$:

$$\begin{aligned} u(r,t) &= \langle u(r,t)\rangle + u_f(r,t) \qquad (1.27) \\ &\langle u_f(r,t)\rangle = 0 \end{aligned}$$

Considering two waves at different frequencies ω_1 and ω_2, with associated the two fluctuating field $u_f^1(r, t)$ and $u_f^2(r, t)$, and observing the fields at a fixed time, we can define the separation or "coherence" frequency at which the correlation function almost disappears:

$$\Delta f = (\omega_1 - \omega_2)/2\pi. \qquad (1.28)$$

Physically, the broadening of a pulse due to a random medium is the inverse of the coherence bandwidth. A piece of evidence, supporting not only the existence of heterogeneities in the lithosphere, but also the derivation of the radiative transfer from correlation theory, is the broadening of the envelopes of the S-waves seismograms (Sato and Fehler, 1998): the duration of the incoherent wave group increases with distance. This effect is evident in the seismograms of the high frequency seismic waves: even if the source duration of a small magnitude earthquakes is shorter than 1 s, the duration of the observed direct S-waves packets is much longer than 1 s.

In section 1.2.2, the Zeng's model, which efficiently describes and predicts the features of high frequency seismic waves propagating in random media, was quickly described. The radiative transfer theory usually takes into account both forward and backward scattering, and is discussed using isotropic scattering, because of its relative mathematical simplicity. In the isotropic case, the scattering properties of the Earth can be specified by a single parameter describing both forward scattering manifested in pulse broadening and backscattering manifested in coda formation, the turbidity g, or the mean free path $l = 1/g$ (Hoshiba, 1991, Margerin et al. 1998). However, isotropic scattering correctly models the development of the coda, whereas it cannot model the envelope broadening. When studying a non-uniformly scattering medium, the pulse broadening of a 'direct' body wave is the most direct approach, since the broadening effect, being produced by forward scattering, mainly reflects the properties of a tubular volume in the vicinity of the ray (Gusev and Abubakirov, 1999, Margerin, 2006) (see also section 2.2.2, Figure 2.2). Imagine that the anisotropic medium contains scatterers that look like small segments whit a preferential orientation; while at a microscopic scale the medium is perfectly isotropic (namely, it is characterized by a spherical indicatrix, using the definition of Gusev et al., 1996), at the macroscopic scale, that is beyond the mean free path, the random medium displays anisotropic attenuation and transport properties. This corresponds to large-scale inhomogeneities; so, in that case, the scattering indicatrix is a narrow lobe along the wave vector of an incident ray (prominent 'forward' scattering) with an angular width of the order of $\frac{1}{ka}$ (Gusev and Abubakirov, 1999), where a is the correlation length. In their study, Gusev and Abubakirov (1996) simulated envelopes of anisotropically scattered body waves at various distances from an instant point source, embedded in a random uniformly scattering medium, by means of direct Monte-Carlo modelling of wave energy transport. The authors look for a model that could qualitatively reproduce the broadening of real direct S-wave with distance and the monotonously decaying shape of the coda envelope, for near earthquakes. They observed, as other authors had done before (Hoshiba, 1993, Hoshiba, 1995), that the isotropic model realistically describes the coda features, while it fails to predict pulse broadening. On the contrary the model of large-scale inhomogeneities, which takes into account non-isotropic scattering coefficients with strong forward scattering, predicts the pulse broadening. So, they generalized the turbidity for the more realistic model of non-isotropic scattering, defining the effective turbidity, $g_e = D/2$, where D is the diffusion constant of the medium (see e. g. Chernov , 1960). Starting from the observations of Abubakirov & Gusev (1990), it was noted that the mean cosine of cumulative angular deflection h of a ray decreases with distance r as:

$$\cos(h) = \exp(-2g_e r). \tag{1.29}$$

Thus, after propagating a certain critical distance r_0, the rays suffer significant angular deflection (of the order of one to two radians). Therefore, defining the effective mean free path l_e, one can write:

$$r_0 = l_e = \frac{1}{g_e}, \tag{1.30}$$

up to which the wave energy propagates within some gradually widening tube along the initial ray. At distances of the order of r_0 and larger, the low-angle approximation breaks down. As the rays continue to propagate, they soon ‘forget’ their initial direction and begin to wander almost isotropically (Gusev and Abubakirov, 1996). In the asymptotic case of large propagation time, $t >> l_e/v_0$, the behavior of rays is essentially a sort of random walk. In this case, the theory (Ishimaru, 1997) predicts the space–time distribution of wave energy according to the diffusion law, similar to the case of isotropic scattering. The asymptotic energy density distribution for this case coincides with that for the case of isotropic scattering, with the value of g equal to g_e. Applications and complements to this theory can be found in many other papers (Hoshiba, 1995, Yoshimoto, 2000, Margerin, 2006), which used Monte-Carlo simulations for statistically anisotropic random media to describe the attenuation and multiple scattering of a scalar wavefield, or to retrieve vertical profiles of turbidity in a given area. Gusev & Abubakirov (1999) synthetically found that the limit time t_e at which the forward scattering effect brakes down is dependent of the seismological characteristics of the medium. In section 2.2.2, the properties of the early-coda will be used as a tool to remove the effects of radiation pattern from the coda-normalized spectra in the application of the CN method to attenuation tomography. The limit time t_e, that is dependent of the seismological properties of the area, will assume a main role, and will be experimentally and statistically investigated.

Chapter 2

Seismic attenuation tomography

"Tomography" means "imaging method" and is in general used to retrieve the inner distribution of physical parameters characterizing the body under study. Tomography revealed its importance at the end of the last century, when its medical application, computing tomography (CT), became a routine tool. In the same period, the application of the tomographic method to geophysical data became one of the most useful and widely studied method for the deterministic characterization of small and long-scale heterogeneities into the Earth. The "velocity" tomography is widely the most applied seismic tomography method today. Travel times, the basic measurement of seismology, can be expressed as the product of the average slowness times the ray length, and can therefore be inverted, in principle at least, to obtain the Earth's seismic velocity. Travel times are predicted with remarkable accuracy by geometrical ray theory, simply by applying Snell's laws (Lay and Wallace, 1995). Today, their measure is a routine tool, accomplished by the increasing computer facilities. Compared with its medical applications, the seismic tomography differs in two ways. First, the rays are not straight, because of the strong refraction within the Earth: their path must be recovered using seismic ray theory (Cherveny, 2001). Second, the receivers must be placed on the Earth surface, and sources with poorly known location are often used. There are many examples of velocity tomography. They cover a wide range of geometries and applications, from imaging global Earth structures to characterizing small tectonic or volcanic areas. In the following sections the second category will be prevalently discussed.

Interpretation of the full waveform of a seismogram is a relatively recent innovation in tomography, following the development of new digital, high dynamic range seismometers, and the computing power needed to compute the complex waveforms produced by even simple Earth structures. When applied to the high frequency waveforms, the tomographic method has been able to image the seismic attenuation [total attenuation and/or scattering attenuation]. The so called "scattering tomography", described in the previous chapter, is able to measure the scattering coefficient in a given heterogeneous area.

As depicted in formula (1.21) of section 1.2.4 for the average total-Q, the attenuation factor must be separated from the source and site factors to perform attenuation tomography. The seismologists developed different separation methods to be used in attenuation tomography, each one to be adapted to the area under study. In section 2.1 the separation methods applied to volcanic areas will be quickly resumed. In section 2.2 a general inversion scheme for attenuation tomography will be described: the quantities imaged by this technique are the attenuation parameter, η, or the total quality factor, Q. The ray tracing methods to be applied in the real data experiments of chapter 3 are described in section 2.2.1. In the end, the application of the CN method to attenuation tomography (section 2.2.2) will be described, with the aim of furnishing an efficient attenuation tomography method to volcanic areas. Moreover, in section 2.4, the multi-resolution (or multi-step) technique applied to seismic tomography is described. It is a field recently developed for the improvement of the imaging resolution in volcanic and fault areas. Section 2.4.1 quickly resumes the main results obtained applying this technique to travel time data. The multi-resolution attenuation tomography is a newer application (see e. g. De Siena et al. (2008)). Section 2.4.2 focuses on the problems encountered in applying such a technique to spectral data.

2.1 The estimates of the seismic attributes for the attenuation tomography in volcanic areas

The knowledge of the internal structure of the volcanoes represents a crucial task to properly constrain the physical models of eruption. Passive tomography is one of the easiest and cheapest way to achieve this goal and is consequently widely applied for the study of volcano structures at several depths (Chouet, 1996). Travel-time tomography is the most commonly used approach to obtain detailed images (Chouet, 2003); attenuation imaging has been used less, despite the increasing number of studies on this subject appearing in the specialized literature (Schurr et al., 2003, Hansen et al. 2004, Eberhart-Phillips et al. 2005, De Gori et al., 1999). The waves that travel short paths, like the ones used in volcanic attenuation imaging, are less likely to be contaminated by the effects of lateral refraction and multipathing, but have the additional requirement that the mechanism and depth of the earthquake must be known (Haberland and Rietbrock, 2001).

In section 1.2.4, both formula (1.21) and formula (1.22) illustrate the main problem of attenuation tomography, in the time and frequency domains respectively: the cut of the source and site effects from the signal. The approach used by seismologists for calculating the spatial distribution of attenuation may strongly vary depending on whether one considers the inversion scheme (back projection (Ho-Liu et al., 1988) and damped least squares (Al-Shukri and Mitchell, 1990)) or the calculation of the whole path attenuation (spectral inversion (Scherbaum, 1990, Lees and Lindley, 1994, Rietbrock, 2001), spectral ratios (Evans and Zucca, 1993, Romero et al., 1997), frequency shift and pulse widths or rise time (Wu and Lees, 1996, De Lorenzo et al. 2001b)). Among the different methods, the *ordinary* or *slope-decay* spectral inversion method (see also section 2.3)requires the knowledge of the source and site factors of formula (1.22), which leads to a direct measure of the attenuation coefficient η, made using different source-station registrations, imaging different blocks (Scherbaum, 1990, Sanders, 1993, Lees and Lindley, 1994). The researcher may assume the source function frequency dependence, parametrized using quantity as the corner frequency (f_{Corn}), the spectral decay (γ) and the low-frequency amplitude level Ω_0 (Abercrombie, 1995). The source function of each earthquake of the data-set can also be inverted together with the attenuation parameters (Haberland and Rietbrock, 2001). The cut of the site factor from formula (1.22) is the main problem of attenuation tomography in volcanic areas, causing the higher uncertainties in the estimates of attenuation. A priory information on this factor is critical for the application of the classical spectral method; researchers usually assume a frequency independence of the site factor (Haberland and Rietbrock, 2001), or an assumed form of frequency dependence (Hansen et al. 2004). Radiation pattern effects are often difficult to parametrize, and, usually, they are assumed to be regrettable; anyway, using local seismicity, their effect may be of the order of attenuation.

An important and frequently applied method to estimate the single path attenuation coefficient is the *spectral ratio.* In this approach the quality factor is always assumed as frequency independent. This method can be applied once that independent estimates of average site effects and source spectrum are carried out (Romero et al. 1997). The average site spectrum is estimated at any single receiver using different earthquakes; the average source spectrum can be obtained using different registrations of a single earthquake. A second version of the spectral ratio technique was proposed by Roth et al. (1999) and Shito et al. (2004). This authors measure the spectral ratios between spectra of different phases, removing the site and source factors and obtaining the sole attenuation factor. The "S-P method" measures the differences in spectral decay between this two phases at the same station; the ray path is the same, as obviously the instrument and site factor and the source function. The ”radiation pattern” effect and the geometrical attenuation are included in a constant of the inversion problem, having as unknown the difference in attenuation between P and S waves. If the mean $\frac{Q_P}{Q_S}$ ratio is known, the frequency independent quality factor can be obtained in the inversion problem. The "P-P method" uses the same ideas, measuring the ratio between P-waves spectra measured at different stations. The only difference is that the differential P-wave quality factor is obtained, for waves travelling different ray-paths.

The *frequency shift* method allows the estimate of the attenuation coefficient from the shift of the frequency at which the spectral amplitude peak is present. In particular, Quan and Harris (1996), assuming different forms for the source (S) and receiver (R) spectra (Gaussian, boxcar and triangular), show that the attenuation coefficient η for an inhomogeneous medium can be obtained by measuring the centroid frequency downshift $[f_S - f_R]$ between signals. A measure of the maximum centroid frequency recorded in the data-set can be a good initial estimated for the source centroid frequency, which can be subsequently inverted with the attenuation parameters.

Both the *pulse-width* and *rise-time* methods are based on measures directly performed on seismograms. This effect is directly related to the presence of forward scattering, testified by the enlargement of the pulses constituting the early coda. Stacey et al. (1975) first derived a formula for rise times of acoustic signals propagating linearly in elastic media with frequency-independent quality factors:

$$\tau = \tau_0 + C \int_{ray} \frac{ds}{vQ} = \tau_0 + C \int_{ray} \frac{dT}{Q}, \tag{2.1}$$

where τ is the pulse rise time, τ_0 is the original pulse rise time at the source, v is velocity, C is a constant, ds is an arc segment along ray path, and dT is the incremental travel time. The pulse rise time is defined as the amplitude of the first arriving pulse divided by the steepest rising slope. On displacement records, the rise time is approximately the pulse width used by Zucca et al. (1994), namely the time difference from onset of initial arrival to initial peak. When the average Q (Q_0) is not well known, formula (2.1) can be used to invert for Q and τ_0 jointly (Zucca et al., 1994). Wu and Lees (1996) use a slightly different approach, measuring pulse width and estimating first C/Q_0 and τ_0 directly from formula (2.1) with a linear fit:

$$\tau = \tau_0 + \frac{C}{Q_0}.$$

The final inversion problem involves the unknown path-dependent Q and a data vector comprehending the measured travel-time and τ_0 obtained in the previous steps:

$$\frac{\tau - \tau_0}{C} = \int_{ray} \frac{dT}{Q}.$$

The changes from a reference rise time are linearly related to the travel time: their measures can be applied to attenuation tomography in analogy with what has been done in the pulse-width method. This seismic attributes can be used both for contemporary inversions of the attenuation parameter and source parameters (De Lorenzo et al. 2001b).

Volcanic zones are among the most heterogeneous media, causing high seismic attenuation in both laboratory and real Earth experiments (Tondi and Franco, 2003, De Lorenzo et al. 2001b); the attenuation of elastic waves depends on a number of factors that affect the lithology, the most important of which are the temperature and the presence of fractures permeated by hydrothermal or magmatic fluids. Many tomographies show a general increase of the quality factors with depth, corresponding to the general increase in seismic velocity (Scherbaum, 1990, Sanders, 1993). Ponko and Sanders (1994) attributed a lowering of the quality factors at a certain depth to the presence of magmatic chambers. Anyway, as it is described in section (1.1.2), the total quality factor images changes of both Q_{Sc} and Q_I. Recent studies (Gudmundsson et al., 2004, Hansen et al. 2004, Eberhart-Phillips et al. 2005) show that a low quality factor at depth can also highlight the presence of fractured zones, H_2O vapor and gas reservoirs; a combined study of the velocity and attenuation features is able to discriminate between different geological characteristics. In addition, the response of the rocks to the propagation of longitudinal waves is different to that for shear waves; consequently, the contemporary knowledge of Q_P and Q_S is crucial for the characterization of the physical state of the rocks inside a volcano. The wave propagation in volcanic areas is intensely affected by the attenuation caused by scattering (see section 1.1.2 for a complete handling). Unfortunately, in single-path estimates of the attenuation coefficient, separation between the two kinds of contribution (scattering and intrinsic) is practically impossible. Consequently, in attenuation tomography, the seismic attribute is the total Q, or the corresponding attenuation coefficient. This is a limit for univocal interpretations of the attenuation imaging. In addition, one needs a suitable source space distribution (sources as much as possible uniformly distributed in the volume, and an as dense as possible network of receivers), to reach this minimum cell size. This almost never happens in central cone volcanos, where the seismicity is usually concentrated under the central cone (Scarpa et al., 2002, Bai and Greenhalgh, 2005).

2.2 The CN attenuation tomography

Although not yet a routine tool, attenuation tomography using local or regional seismicity and artificial sources has been well known for a number of years (Sanders, 1993). Models of Q determined using single-station measurements usually have an advantage over methods that use station pairs along a great-circle path in that they are more likely able to utilize relatively short paths. In single-station attenuation tomography, formula (1.9) is considered to parametrize the spectral amplitude decrease of a single seismic wave due to its interaction with the medium. In this formula, the factor $\exp(-\frac{\omega x}{2vQ})$ may be rewritten:

$$\exp(-\frac{\omega x}{2vQ(f)}) = \exp(-\frac{\pi f t}{Q(f)}) = \exp(-\pi f t^*(f)), \tag{2.2}$$

where the attenuation parameter $t^*(f) = \frac{t}{Q(f)}$ is function of both the ray-path and frequency. $t^*(f)$ may be defined:

$$t^*(f) = \int_{ray} \frac{1}{Q(l,f)v(l)} dl, \tag{2.3}$$

where l is the curvilinear coordinate measured along the seismic ray (see section 2.2.1). $Q(f)$ represents the total quality factor.

The discretization of formula (2.3) is accomplished dividing the medium into parts. A volume of linear dimension Y may be divided into a number of volumes dependent on their dimension $y \leq Y$. From now on *cubic volumes* will always be considered: the entire medium is contained in a cubic block which can be divided in cubic blocks of smaller linear size. The resolution at which the medium is imaged corresponds to the length size of the block. A seismic velocity is "a priory" assigned at each block for each resolution. Formula (2.3) becomes:

$$t^* = \int_{ray} \frac{1}{Q(l)v(l)} dl \tilde{=} \sum_{b=1}^{B} s(b)l(b)Q^{-1}(b), \tag{2.4}$$

where $s(b)$, $Q^{-1}(b)$ and $l(b)$ are the slowness, the total quality factor and the length of the segment of ray contained in the block b, while B is the total number of blocks crossed by the single ray.

2.2.1 Tracing rays in highly heterogeneous media

Seismic rays are general 3-D curves connecting seismic sources to receivers. In any high frequency, body-wave velocity or attenuation tomography it's of paramount importance to accurately calculate the rays. The selection of the appropriate procedure to compute seismic rays and the relative travel times is greatly influenced by such factor as the dimensionality of the model under consideration (1-D, 2-D, 3-D), its complexity, the source-station configuration, and many others. The high-frequency asymptotic methods applied to acoustic and elastodynamic wave equations are by far the most commonly applied to the problem of knowing the path of a wavefront in a given medium (Cherveny, 2001). In the acoustic case, the high-frequency asymptotic methods use the eikonal equation $(\nabla T)^2 = 1/c^2$, where T is the travel time and c the wave velocity, as the basic equation to calculate travel times and ray-paths (Aki and Richards, 1980). The eikonal equation is a nonlinear partial differential equation of the first order, usually solved for travel time T in terms of its characteristics (Bleistein, 1984) and represents the basic equation of the ray theory. In seismic ray theory the characteristics of the eikonal equation are the *rays* and the system of ordinary differential equations for the characteristics is the *ray tracing system* (Cherveny, 2001).

The procedures created to compute rays and travel times can be divided in two main categories: the initial-value ray tracing and the boundary-value ray tracing (Cherveny, 2001). In the initial-value ray tracing, the direction of the ray is known at some point of the ray, or, at least, it may be simply determined from some other data. The position and direction of the ray at that point are the initial conditions of the ray tracing system and many methods can be used to calculate the ray trajectory. Boundary-value three-dimensional ray tracing plays a considerably more important role in tomography; in this case, the direction of the ray is unknown at any of its point, but some other condition is known. As an example, one can search the ray-path of a wave connecting two points, defining a two-point ray tracing, without knowing the direction of the ray at any of these two point (the problem corresponds to the definition of the ray by Fermat's principle). The most important methods developed for this kind of ray tracing are the shooting method, the bending method and the methods based on structural perturbations (see Červený, 2001 for a complete review). Both the "parabolic" and "numeric" ray tracing, described in the following sections, are two point ray-bending methods.

Parabolic and numerical ray tracing

In the parabolic ray tracing the real ray passing through the source and the receiver is approximated by a quadratic polynomial. Moreover, the parabolic rays are bidimensional and they are contained in the vertical plane connecting source and station. A code was developed to search for the best-adapted parabola numerically, satisfying the Fermat's principle of minimum travel time, in the same velocity model utilized in the location procedure. A "storing" algorithm was added to the code, allowing quick storing of the coefficients of the parabolas and of the position of the vertical planes containing the rays. In the code, it was checked that the travel times for the parabolas are smaller than the ones for the segments connecting the sources and the receivers, namely using Fermat's principle. This bidimensional parabolic ray tracing technique is weak, because the real rays in the velocity model of a volcanic area usually deviate strongly from the assumptions above discussed, and can only be effective at low resolutions. Anyway, in this case an analytic expression of the ray is available, allowing quick storing of the ray parameters.

In the numerical method, an initial ray path is guessed and then perturbed iteratively, yielding to the relevant boundary value ray. The guessed trajectory need not, in general, correspond to any actual ray; it may just be an auxiliary curve connecting source and receiver (Figure 2.1).

The numerical method does not represent a complete solution of the boundary-value ray tracing problem. First, an independent algorithm to estimate the guessed trajectories must be used (the *ray estimator).* After the ray estimator has generated the preliminary ray trajectories for all the sources and receivers, the numerical method corrects the preliminary trajectories. The numerical method used in this Ph.D. thesis is the Thurber-modified (or *pseudo-bending*) method, based on minimizing the travel time on the ray path, first proposed by Um and Thurber (1987) and developed in Block et al. (1991) for media having sharp velocity variations. In this case, the ray elements between blocks are straight lines, and the ray of

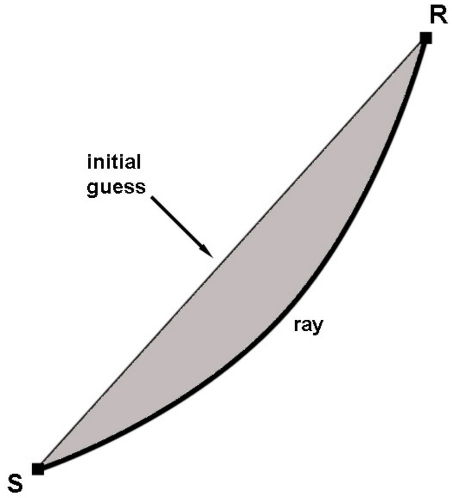

Figure 2.1: The solution of two-point ray tracing by the bending method. The initial guess ray path is guessed and then perturbed iteratively. The final ray is shown as the bold line. (From Čhervený, 2001)

any elementary wave may be fully specified by the coordinates of points of contact with the individual structural interfaces. In the optimization procedure, the coordinates of the points of contact of the ray trajectory with structural interfaces are sought, and the final rays satisfy Snell's laws at any of this point. Then, the final ray is made of segments, each one included in a block at the chosen resolution. Finally, the source coordinate, the receiver coordinate and the point of contact of each segment with the sides of the blocks are stored.

2.2.2 Inversion scheme for the CN method

The CN method, described in section 1.2.4 as a method to measure the average attenuation path effects, is adapted to estimate single path S-wave attenuation. The estimates of S-wave attenuation for the whole set of ray-paths define an inversion problem, as described in Del Pezzo et al. (2006a) and in the first year activity report of my Ph.D. The method uses the scattering effects as a way to remove the source, site and instrumental effects from the signal. It has been applied to two different volcanic areas, as described in chapter 3. The results show that this method is particularly efficient when applied to highly heterogeneous media.

The S-wave seismic energy density spectrum, as well as the spectral amplitude of formula (1.22), is:

$$E_{ij}(f,r) = S_i(f)\theta_{ij}(\vartheta,\phi)I_j(f)T_j(f)\frac{1}{r_{ij}^2}\exp(-2\pi f\frac{t_{ij}(r)}{Q_T^{ij}(r)}), \tag{2.5}$$

where $E(f,r)$ is the energy density spectrum of the S-wave radiation emitted by the source i at total distance r measured along the ray-path connecting source(i) and station (j) ; f is the frequency. $S_i(f)$ is the energy spectrum at source, modulated by the radiation pattern function $\theta(\vartheta,\phi)$, which in principle depends on source azimuth ϕ and incidence angle ϑ. I_j is the instrument transfer function and T_j is the site transfer function. t_{ij} is the travel time along the ray whose length is r_{ij} and Q_T^{ij} is the total quality factor measured along the ray-path.

The coda energy spectrum evaluated around a given lapse time, t_c, can be considered as a function of the "average" medium properties and expressed as in Sato and Fehler (1998):

$$E^C(f,t) = S_i(f)I_j(f)T_j(f)P(f,t_c), \tag{2.6}$$

where $P(f,t_c)$, is independent on both source-receiver distance and directional azimuth and depends only by the Earth medium. The radiation pattern term $\theta_{ij}(\vartheta,\phi)$ disappears due to the well known property of natural space averaging of coda waves (Aki, 1980b). In principle, the coda power $P(f,t_c)$ can take any analytical form, as it is independent of the assumed scattering model. For sake of simplicity, the validity of the single scattering model is assumed, but in principle formula (2.6) is independent of any scattering model. Hence:

$$P(f,t_c) = \frac{2g_0}{t_c^2V_0^2}\exp(\frac{-2\pi f}{Q_c(f)}),$$

where Q_c is the coda-Q, depending on frequency, g_0 is the scattering coefficient (averaged on the volume encompassed by the coda waves) and V_0 is the average velocity. Dividing formula (2.5) for formula (2.6) for each source-station pair, at lapse time t_c:

$$\frac{E_{ij}(f,r)}{E^C(f,t)} r_{ij}^2 = \frac{\theta_{ij}(\vartheta,\phi)}{P(f,t_c)} \exp\left[-2\pi f \int\limits_{rij} \frac{dl}{v(l)Q^{ij}(l)}\right], \tag{2.7}$$

which is independent of the energy level at source, site and instrument transfer function. In formula (2.7) the attenuation operator has been substituted with the path integral along the seismic ray, where $v(l)$ is the velocity along the path l. The spectral ratio at the left side of formula (2.7) is independent of energy level at source, site and instrument transfer function.

The right side of formula (2.7) must be made independent of the radiation pattern $\theta_{ij}(\vartheta,\phi)$ to be used in attenuation tomography.

Test of independence from radiation pattern effects

If the source radiation pattern would have spherical symmetry, and/or the effect of the forward scattering could be removed, the CN method would be an efficient method to retrieve attenuation. The S-wave radiation pattern should vary only slightly over angles of the order of the cumulative angle of multiple scattering to apply the method. This is clearly not true for small earthquakes at regional distances, where double-couple sources have lobes of comparable angular size (the source radiation pattern). In high frequency seismograms, the early-coda (namely coda waves at short lapse time, less than twice the S-wave travel time) retains information about this source radiation pattern. Forward scattering models can explain the formation of early codas (Gusev and Abubakirov, 1996). Gusev and Abubakirov (1999) demonstrated that early-coda can be used as a tool to remove radiation pattern effects from the seismic attribute described by formula (2.7). These authors observed that, as the rays propagate into the medium, there is a limit time t_e at which the forward scattering effect, which causes anisotropy (see section 1.2.5) breaks down and the scattering field becomes isotropic, forgetting the initial anisotropy of the source radiation pattern. The existence of this limit time allowed Del Pezzo et al. (2006a) to develop a new empirical method to test the effective independence of the S-wave spectra from radiation-pattern, when the spectrum is estimated on a time window of duration much greater than the source duration. At a certain temporal length, as ensured by the limit time t_e, the term $\theta_{ij}(\vartheta, \phi)$ will become a constant θ.

The physical process involved in measuring the direct S-wave energy with temporal windows of increasing lengths is described phenomenologically using Figure 2.2. Consider an anisotropic medium, characterized by small heterogeneities, and deploy two seismic stations on surface (A and B). Moreover, suppose that an earthquake takes place at 0 km depth; assuming a given P- (blue) and S-(red) source radiation pattern, the source-station S-wave rays can be traced, with one of the ray-bending methods described in section 2.2.1. Two high frequency seismograms (vertical component) recorded at each station, where early and late codas are evident, are also plotted. The seismograms of Figure 2.2 are real seismograms recorded at different stations in the Campi Flegrei area; they are shown only to illustrate the different window length considered in a) and b). In Figure 2.2a the energy of a narrow time window (say 1 s) is measured, starting 0.1 s before the S-wave onset and containing the maximum amplitude of the entire seismogram for station A. The wave energy contained in this time window is strongly affected by a minimum of the source S-wave radiation pattern, due to the source-station directivity. The wave energy contained in the same window applied to the seismogram of station B is strongly affected by a maximum of the source radiation pattern. Whatever the considered station, the pulses contained in this narrow time window are the ones produced by the scattering centers located near the S-wave ray path. Each scattered energy flux will be characterized by a strong contribution of the source radiation pattern. Measuring the direct-S wave energy at station B on such a time window, the term $\theta_{ij}(\vartheta, \phi)$ of formula (2.7) is still different from the one measured at station A for different combination of θ and ϕ, creating a bias with the attenuation tomography results (e. g. imaging an higher Q where a maximum of the source radiation pattern is present).

Let's consider a longer time window to measure the S-wave energy at stations A and B (3 seconds, Figure 2.2b); from the work of Gusev and Abubakirov (1999), the length of the time window will not overcome twice the S-wave arrival time, in order to consider early-codas. The wave energies contained in both the time windows are no more affected by the two different source S-wave radiation patterns. Figure 2.2b shows the energy tubes corresponding to the window lengths now considered.

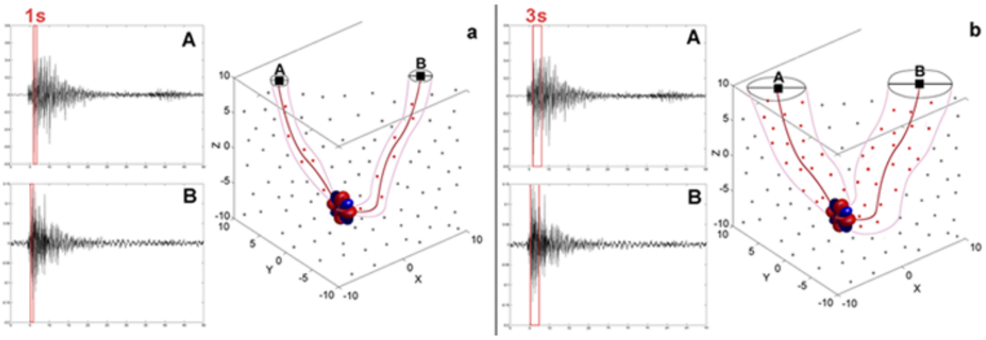

Figure 2.2: The energy tubes corresponding to a time-window of 1 s (a) and 3 s (b) for a single earthquake at two different stations. The scattered energy considered in each time window is the one scattered by the scattering centers colored in red. For the 1 s window (a), the total energy is deeply influenced by the source radiation pattern and the scattering centers are located near the seismic ray. The scattered energy considered in a 3 s time window (b) is produced by scattering centers at a larger distance from the ray, so that the contribution of the source radiation pattern on the spectral amplitude measures is lower.

The scattering centers contained in the energy tube surround the source, and the scattered energy is influenced by different parts of the radiation pattern. The wider window randomizes the source radiation pattern (as for late coda) and causes the radiation pattern at different station to be equal to a constant.

A measure of this process is the quantity defined by the spectral ratio of the coda normalization method, normalized for the source station density and for the average total attenuation of the area:

$$D = \frac{LR}{M}. \tag{2.8}$$

L is the ray length, R is the spectral ratio between energies of formula (2.7) and $M = \exp(-\pi f r/(V_0 Q_{mean}))$, with V_0 and Q_{mean} indicating the average S-wave velocity and the average anelastic attenuation in the area, respectively. D is implicitly only dependent on the radiation pattern, R being independent of site and instrument effects. One can measure this quantity at different stations and then compute the standard deviation (or the percent standard deviation) among the estimates. The measure can be accomplished for different window lengths. In the end, the standard deviation can be plotted as a function of the time window length. In the single scale and multi scale S-wave attenuation tomography of Mt. Vesuvius (section 3.2.2 and section 3.3.2, respectively) two applications of this test are shown. As expected, the standard deviation and the percent standard deviation dramatically decrease with the time length. The differences due to the radiation pattern effects at different station decrease, and, at the limit time t_e, the radiation pattern effect poorly influences the attenuation images; this threshold (t_e) for the window length must be established in order to maximize the resolution (this can be done practically or statistically, as described in the applications on real data in chapter 3).

The main problem of this approach is the possible bias that arise due to the indeterminateness of the ray tube section (Figure 2.2b) when such a long time window is considered. If the section of the ray-tube becomes too large, overcoming the size of a single cell at the imaging resolution, the velocity field will vary, causing a bias in the attenuation estimates. The section of the ray tube is assumed to be of the order of the cell dimension. The check of this assumption is done "a posteriori", looking at the attenuation tomography results obtained measuring the direct S-wave energy with different window lengths.

The inversion scheme

Following formula (1.5) the energy densities of formula (2.7) are transformed in spectral amplitudes of direct S-waves and coda waves (A^S_{ij}, A^C_{ij}). From the previous section, the radiation pattern term $\theta_{ij}(\vartheta, \phi)$ for an S-wave spectrum computed on an adequate time window is a constant θ. Assuming $\theta = 1$:

$$\frac{A^S_{ij}(f,r)^2}{A^C_{ij}(f,t)^2} r_{ij}^2 = \frac{1}{P(f,t_c)} \exp\left[-2\pi f \int_{rij} \frac{dl}{v(l)Q^{ij}(l)}\right]. \tag{2.9}$$

Taking the logarithm of formula (2.9):

$$\ln\left[\frac{|A^S_{ij}(f)|}{|A^C_{ij}(f,t_c)|} \cdot r_{ij}\right] = K(f,t_c) - \pi f \int_{r_{ij}} \frac{dl}{v(l)Q^{ij}(l)}, \tag{2.10}$$

where $K(f, t_c)$ is constant for each frequency band, depending only on the average properties of the Earth medium and of the seismic ray for the couple ij. The constant $K(f, t_c)$ in the assumption of single scattering is given by:

$$K(f) = \frac{t_c^2 V_0^2}{2g_0} \exp(\frac{2\pi f t_c}{Q_c}), \tag{2.11}$$

and can be independently estimated from the already determined estimates of Q_c in the area. Introducing the slowness, $s(l) = 1/v(l)$, and discretizing:

$$R_{ij} = K(f) - \pi f \sum_{b=1}^{B} l_{ijb} s_b Q_b^{-1}, \tag{2.12}$$

where R_{ij} represents the log of the amplitude spectral ratio premultiplied by r; index b indicates the b-th block in which the Earth medium is divided and B is the number of blocks. s_b and l_{ijb} are the slowness and the length of the ray-segment crossing the b-th block, respectively.

The inversion scheme expressed by formula (2.12) can be solved simultaneously for $K(f)$ and the set of Q^{-1}, or K can be a priori set to some value already estimated in the area, so that the inversion scheme is solved only for the set of Q^{-1}. The inversion problem can be rewritten for sake of compactness in a simpler way, changing the couple of indexes ij in a single integer index, k. k ranges from 1 to N_pairs where N_pairs is the number of source station pairs, and designates the corresponding ray-path. Analogously, N_cells indicates the total number of blocks crossed by the k-th ray. Denoting:

$$C(f) = \frac{K(f)}{\pi f}, \tag{2.13}$$

formula (2.12) becomes:

$$C(f) - \frac{R_k(f)}{\pi f} = \sum_{b=1}^{N\_cells} l_{kb} s_b Q_b^{-1}. \tag{2.14}$$

In matrix form, representing the suite of the ray-paths, formula (2.14) is:

$$\mathbf{d}(f)= \mathbf{Gm}(f), \tag{2.15}$$

where the vector **d** contains the calculated spectral ratios for each frequency band for all the ray-paths. **G** is a rectangular sparse matrix:

$$\mathbf{G} = \begin{bmatrix} l_{11}s_1 & l_{12}s_2 & \cdot & l_{1b}s_b & 0 & \cdot & l_{1N\_cells}s_{N\_cells} \\ l_{21}s_1 & l_{22}s_2 & \cdot & 0 & 0 & \cdot & l_{2N\_cells}s_{N\_cells} \\ \cdot & \cdot & \cdot & \cdot & \cdot & \cdot & \cdot \\ \cdot & 0 & \cdot & l_{kb}s_b & \cdot & 0 & \cdot \\ \cdot & \cdot & \cdot & \cdot & \cdot & \cdot & 0 \\ 0 & \cdot & \cdot & \cdot & \cdot & \cdot & \cdot \\ \cdot & \cdot & \cdot & \cdot & \cdot & \cdot & \cdot \\ l_{N\_pairs1}s_1 & l_{N\_pairs2}s_2 & \cdot & 0 & \cdot & \cdot & l_{N\_pairsN\_cells}s_{N\_cells} \end{bmatrix}, \tag{2.16}$$

and **m** is the column vector containing the estimates of Q^{-1} for each volume cell. The linear discrete inverse problem can be solved separately for each frequency band; from now on the data vectors are always calculated in a given frequency band.

The least square solution to the linear inverse problem of formula (2.15) can be found minimizing the 2-norm:

$$\min \|\mathbf{Gm} - \mathbf{d}\|_2 \,. \tag{2.17}$$

The error associated to each data element in the linear discrete inversion problem of formula 2.15 is assumed to be due only to the spectral ratios between the direct-S and coda spectra (see formula (2.10)). The least square solution turns out to be statistically the most likely solution if data errors are normally distributed, like in this inversion (Aster et al., 2005). In the physical problem, the model parameters (Q^{-1}) are inherently nonnegative, and their lower bound is zero. The inversion problem defined by formula (2.17) needs to be constrained to obtain only positive values of Q^{-1}; it can be rewritten:

$$\min \|\mathbf{Gm} - \mathbf{d}\|_2, \mathbf{m} \geq \mathbf{0}. \tag{2.18}$$

The non negative least square algorithm, described by Lawson and Hanson (1974) , is a useful tool to solve this kind of problem, implemented in MATLAB with the name "lsqnonneg". It starts with a set of possible vector basis ($\mathbf{m}$), and computes the associated dual vector $\mathbf{w}$:

$$\mathbf{w} = \mathbf{G}^T(\mathbf{d} - \mathbf{Gm}). \tag{2.19}$$

It then selects the basis vector corresponding to the maximum value in $\mathbf{w}$ in order to swap out of the basis in exchange for another possible candidate. This continues until $\mathbf{w} \leq \mathbf{0}$, which takes to $\mathbf{m} \geq \mathbf{0}$. At this point a covariance matrix that contains the variance of each unknown and the covariance of each pair of unknowns may be defined; else a bootstrap approach may be applied to the data, like in the application to real data of section 3.2.3.

2.3 Alternative methods for the estimate of the seismic attributes

The slope-decay (SD) method is used in chapter 3 both to check the results obtained with the CN method for the S-waves and to obtain P-wave attenuation images. Two slightly different applications of this method, that will be applied to the Mt. Vesuvius (2.3.1) and Campi Flegrei (2.3.2) areas are described in the following sections. Moreover, in order to avoid the effect of coda localization in both the volcanic areas (Tramelli, 2008) the inversion scheme for the CN method (see section 2.2.2) can be slightly changed, considering as model parameters the variations respect to the average quality factor. Taking logs of both sides of formula (2.9) and approximating the line integral with a sum, it becomes:

$$d_k^C = \frac{1}{2\pi f}\ln(\frac{1}{P(f,t_c)}) - \sum_{b=1}^{N\_cells} l_{kb} s_b Q_b^{-1} \tag{2.20}$$

where d_k^C represents the log of amplitude spectral ratio between S and coda, premultiplied for the ray-length, and divided for $2\pi f$. In this formulation the suffix k is used to indicate the k-th ray of the suite of rays connecting stations to sources. Formula (2.20) can be rewritten separating Q_b^{-1} into an average Q_b^{-1}, $<Q_b^{-1}>$, that is assumed to be equal to the average quality factor for the whole area (Q_T^{-1}), and an incremental δQ_b^{-1}. It results:

$$\widetilde{d_k^C} = \sum_{b=1}^{N\_cells} l_{kb} s_b \delta Q_b^{-1} \tag{2.21}$$

where:

$$\widetilde{d_k^C} = \frac{1}{2\pi f} \ln(\frac{1}{P(f,t_c)}) - d_k^C - Q_T^{-1} \sum_{b=1}^{N\_cells} l_{kb} s_b. \tag{2.22}$$

Both the inversion schemes described in the two following sections are formally identical to the one of formula (2.22),apart the constant values.

2.3.1 The modified slope-decay method

As well known, the amplitude spectral density for S and P waves, for frequencies higher than the corner frequency, can be expressed as the product of source, path and site effects as:

$$A_{ij}^{HF}(f,r) = S_i^A(f) I_j(f) T_j(f) G_{ij}(r) \exp(-\pi f \frac{t_{ij}(r)}{Q_T^{ij}(r)}), \tag{2.23}$$

where $A^{HF}(f,r)$ is the high-frequency spectral amplitude of the P- or S-wave radiation emitted by the source i at total distance r measured along the source(i)-station (j) ray-path; f is the frequency; $S_i^A(f)$ is the amplitude spectrum at source; I_j is the instrument transfer function; T_j is the site transfer function and G is the geometrical spreading term; t_{ij} is the travel time along the ray of length r and Q_T^{ij} is the total quality factor measured along the ray-path. In the present formulation it is assumed that the high frequency amplitude spectrum at the source can be described by a function $S_i^A = const_i \cdot f^{-\gamma}$, γ being a constant for the whole set of data utilized. Taking the natural logarithm and making the derivative of formula (2.23) with respect to frequency, f, it can be written for each ray-path:

$$D_f(\ln A_{ij}^{HF}) = D_f(\ln S_i^A) - \pi \frac{t_{ij}(r)}{Q_T^{ij}(r)}, \tag{2.24}$$

where D_f is the symbol of derivative. In obtaining formula (2.24), the site and instrument transfer function are assumed as independent of frequency. Transforming the couple of indexes ij in a single integer k associated with the single ray, as it was previously done for the CN method, formula (2.24) becomes:

$$D_f(\ln A_k^{HF}) = D_f(\ln S_i^A) - \pi \frac{t_k(r)}{Q_T^k(r)}. \tag{2.25}$$

Averaging the left hand quantity of the above formula over the rays considered (k index):

$$\begin{aligned} &< D_f(\ln A_k^{HF}) >_k = D_f^0(\ln A^{HF}) = \\ &\qquad < D_f(\ln S_i^A) - \pi \frac{t_k(r)}{Q_T^k(r)} >_k \quad = D_f^0(\ln S^A) - \pi < \frac{t(r)}{Q_T(r)} >_k . \end{aligned} \tag{2.26}$$

$D_f^0(\ln S^A)$ results to be the same of $D_f(\ln S_i^A)$ (the average of the source spectral derivative equals the spectral derivative for the single event), so that I can write:

$$D_f(\ln A_k^{HF}) - D_f^0(\ln A^{HF}) \tilde{=} \pi (< \frac{t(r)}{Q_T(r)} >_k - \frac{t_k(r)}{Q_T^k(r)}). \tag{2.27}$$

Indicating with d^D the quantity:

$$d_k^D = \frac{1}{\pi} \left[D_f(\ln A_k^{HF}) - D_f^0(\ln A^{HF}) \right] \tag{2.28}$$

and expressing the right hand side of formula (2.27) as already done in formula (2.20), it results:

$$d_k^D = \quad < \frac{t(r)}{Q_T(r)} >_k - \sum_{b=1}^{N\_cells} l_{kb} s_b Q_b^{-1} \tag{2.29}$$

where the index k is referred to the k-th ray.

Making the same assumption that leads to formula (2.21), the final inversion scheme is:

$$\widetilde{d}_k^D = \sum_{b=1}^{N\_cells} l_{kb} s_b \delta Q_b^{-1}, \tag{2.30}$$

where:

$$\widetilde{d}_k^D =< \frac{t_k}{Q_k} > -d_k^D - Q_T^{-1} \sum_{b=1}^{N\_cells} l_{kb} s_b. \tag{2.31}$$

that is formally identical to the inversion scheme of formula (2.30).

2.3.2 The ordinary slope-decay method

To estimate the single-path P-wave attenuation, the ordinary slope decay method (Gudmundsson et al. 2004, De Gori et al. 1999, Eberhart-Phillips et al. 2005) has also been considered. The amplitude spectral density for P-waves or S-waves of formula (2.20) can be also written as:

$$A_{ij}^{HF}(f,r) = S_i^A(f) I_j(f) T_j(f) G_{ij}(r) \exp(-\pi f \int_{rij} \frac{s(l)dl}{Q_T(l)}) \tag{2.32}$$

where the only difference is the substitution of t_{ij} with the slowness $(s(l))$ measured along the ray path l. In the present method, the formulation of Abercrombie (1995) is used, assuming that the high frequency amplitude spectrum at the source can be described by a function:

$$S_i^A = \frac{\Omega_0}{[1 + (f/f_{Corn})^{\gamma n}]^{1/\gamma}} \tag{2.33}$$

where Ω_0 is the long period amplitude, f_{Corn} the measured corner frequency, n the frequency (log-log) fall-off rate, and γ is a constant for the whole set of data used. The modified version of the spectral shape proposed by Boatwright (1980) ($n = 2$ and $\gamma = 2$) better fits the displacement spectra obtained from the dataset. Following the formulation of Anderson and Hough (1984) and Margaris and Boore (1998), the quantity $T(f)$ in formula (2.32) is factorized in the product of $T\prime(f)$, a path-independent site-transfer function, and a path-dependent term, $exp(-k_0 f)$, where k_0 is a coefficient characteristic of the site.

Taking the natural logarithm, making the derivative of the formula (2.32) with respect to frequency and transforming the pairs of indexes ij into a single integer k that is associated with the single ray, as in the previous section, it can be written:

$$D_f(\ln A_k^{HF}) = -2\frac{f^3}{f_{Corn}^4 + f^4} - \pi k_0 + D_f(\ln(T'(f)) - \pi f \sum_{b=1}^{N\_cells} l_{kb}s_bQ_b^{-1}). \quad (2.34)$$

where D_f is the symbol of the derivative. In obtaining formula (2.34), the independence of the frequency for the instrument transfer function, which is flat in the whole frequency range investigated, is assumed, and the integral is approximated with a sum. Moving to the left and indicating with d_k^S the measured quantities, it is derived:

$$d_k^S = \frac{1}{\pi}\left[-D_f(\ln A_k^{HF}) - 2\frac{f^3}{f_{Corn}^4 + f^4} - \pi k_0 + D_f(\ln(T'(f)\right], \quad (2.35)$$

through which it is obtained:

$$d_k^S = \sum_{b=1}^{N\_cells} l_{kb}s_bQ_b^{-1}, \quad (2.36)$$

where the index k is always referred to the k-th ray.

The final inversion scheme is:

$$\widetilde{d_k^S} = \sum_{b=1}^{N\_cells} l_{kb}s_b\delta Q_b^{-1}, \quad (2.37)$$

where:

$$\widetilde{d_k^S} = d_k^S - Q_T^{-1} \sum_{b=1}^{N\_cells} l_{kb}s_b. \quad (2.38)$$

The inversion schemes (3.9) and (2.37) are formally identical, apart the constant values.

2.4 Multi-resolution inversion

The main crustal imaging problem consists in creating a large $3D$ velocity model to include as many events as possible, with a dense cell size. In a tomographic study, the other factors to be considered in choosing the cell size are the seismic wavelength and the signal to noise ratio. Restrictions on source–receiver geometry, coupled with the limitations due to the quality of the seismic signals, may make it difficult to tomographically image deep crustal velocity structure on a local scale, such as beneath a volcano or a caldera (Bai and Greenhalgh, 2005). Starting from previous multi-resolution inversion algorithms applied to velocity tomography (Chiao and Kuo, 2001, Bai and Greenhalgh, 2005) the problem of creating a multi resolution inversion algorithm for attenuation tomography is approached. First, the multi-resolution velocity tomography methods will be resumed in section 2.4.1, extracting the results which can be applied to attenuation tomography. Second, the multi-resolution attenuation tomography algorithm, a joint application of a nonuniform cell size algorithm and an updating algorithm, will be described in section 2.4.2. The attention will be mainly pointed on the difficulties found in considering measures performed on the full waveform.

2.4.1 Multi-resolution velocity tomography

The resolution of seismic velocity structure depends on the number of rays that sample the single cell. A velocity tomography can use a nonuniform cell size model to maintain a relatively high resolution in a given area. Many authors (Thurber, 1987, Vesnaver, 1996, Sambridge and Gudmundusson, 1998) apply a fine cell size grid to a target or part of the area, and a coarse cell size outside the target. The solution in the target area can be directly obtained by multiple inversions; even if this procedure can make the problem tractable, sometimes it causes a loss of resolution (on the larger cells) or introduces large travel time errors, as demonstrated by Bai (2004). Moreover, the total number of velocity unknowns in the inversion scheme must be comparable to the total number of ray paths. This is a common problem for tomography, frequently solved increasing the number of available sources (using regional events and teleseisms) and/or stations (Iyer and Dawson, 1993, Bijwaard et al., 1998); anyway, because of the dispersion of the increased sources and/or stations, this approach takes sometimes to the problem of inverting for a $3D$ velocity field with an excessive number of velocity unknowns (Bai and Greenhalgh, 2005). This in turn slows the convergence rate and, even worse, may stall the convergence process of the optimization method. Eberhart et al. (1990) overcome this problem, constraining the update of the velocity field to be within the target volume only, using a small partial region in the whole area to reduce the large number of unknowns. In this way, the velocity field is updated in the target part of the area only, and the other parts are left unchanged.

So, a nonuniform cell size model can be obtained; moreover, an update of the velocity field can be made, considering only the target region (Thurber, 1987, Eberhart-Phillips, 1990). That is, the whole inversion scheme is constituted by a forward modeling for the regional model (outside the target region), in which the velocity field is unchanged, and a subsequent inversion for the target model (embedded in the whole model) where the velocity field needs to be updated. Bai and Greenhalgh (2005) extend the results obtained with this method, first performing the forward modeling on a large (regional) scale to obtain the crossing points where the ray paths intersect the boundaries of the local (small) volume; second, they compute the associated travel times from regional sources to these crossing points; finally, they perform tomographic processing to obtain the small model using local earthquakes, plus the predicted crossing points as the new sources from the regional events. The original large model is reduced to a small model around which the regional ray crossing points (new sources) have been delineated. With this procedure, one can select a smaller cell size to divide the large model because there is only one forward modeling run. Moreover the large model can be separated into several sub-regions without dramatically increasing the computational effort to obtain travel times and ray paths to greater accuracy. An interesting method used to reduce the relatively large source parameter uncertainty of regional events is to relocate them in the multi-step procedure, before the final local inversion is undertaken (Bai and Greenhalgh, 2005). So, the information that pertains to the velocity structures on a regional scale is removed after relocation, and only information on local velocity anomalies remains.

Anyway, whichever the method, there are always some disadvantages in a multi-step procedure: first, it causes some artifacts in the target region because of the travel time errors in the forward modeling through the large model, having a coarse grid spacing. Second, when the velocity structure outside the target model is poorly estimated, any unknown “structure” or complexity in the regional velocity model will corrupt the target model. In such circumstances, Bai and Greenhalgh (2005) proceed obtaining a relatively smooth, but realistic ‘a priory‘ model from the large model inversion scheme, with coarse grid nodes. They assume that the background velocity on the regional scale can be roughly estimated, and the whole tomographic procedure (the case with a large model length and a small cell size) can be separated into two (or more) consecutive processes. The other factors to be considered in choosing the cell size are the seismic wavelength and the signal to noise ratio. It is pointless specifying too dense a grid if the sharpness (onset) of the waveform and the amplitude of the pulse are insufficient to reliably pick arrival times.

2.4.2 Multi-resolution attenuation tomography

In attenuation tomography studies, some of the techniques developed by multi-resolution velocity tomography may be applied, especially the ones referring to a nonuniform cell size model. The seismic attributes in an attenuation tomography can be obtained in the time and spectral spaces (see section 2.1). Then, the co-variances of the data are usually bigger than the one associated with travel time data. This obviously takes to a smaller data-set than the one used for the necessary and previously accomplished velocity tomography of the area. Consequently, the data quality and the seismic wavelength assume the main role in attenuation tomography. A data-set which is efficient using the classical spectral methods may fail to measure the attenuation parameters with the coda-normalization method, because of the scarce lengths of the codas, which do not allow to consider coda spectra at a sufficient lapse time. The measure of attenuation in a low frequency band may not be possible because of data noise; higher frequency waves may better solve small structures, but are also limited by the presence of high frequency noise and aliasing filters (Aki and Richards, 1980). Generally the smallest wavelength characterizes the minimum cell size, and this can be considered as the thumb rule for this constraint. The wavelength is also directly associated with the kind of events that are used as input. For a local tomography on a volcano with a volume of the order of 10 km of linear dimensions, local VT earthquakes, with their associate wavelengths that ordinary span from some kilometers to hundreds of meters (Chouet, 2003) are a suitable input. Measuring the spectral content at a central frequency f_c corresponds to limit the maximum resolution achievable in the an area of velocity V_0. This limit is:

$$\lambda = \frac{V_0}{f_C}. \tag{2.39}$$

The multi-step process applied to attenuation tomography defines an inversion problem for each considered resolution. It may be schematized as the sum of a non-uniform inversion problem, similar to the one described for velocity tomography, and a problem of updating of the data vector at higher resolutions.

First, let's define the non-uniform inversion problem in an heterogeneous medium with a known average quality factor (Q_{mean}), where a seismic event takes places. The direct S-wave is recorded at a station on surface, after travelling along a known ray path (Figure 2.3a). The initial volume can be divided in a grid with step u, defining as model parameters ($\mathbf{m}_u$=Q_u^{-1}) the quality factors in the blocks with block size u (Figure 2.3b):

$$\mathbf{d} = \mathbf{G}_u\mathbf{m}_u. \tag{2.40}$$

If the data vector for the inversion scheme, $\mathbf{d}$, can be measured (e. g. with the CN method) the model parameters at the u resolution can be obtained (e. g. with the least-squared method, or the singular value decomposition (Menke, 1984)) for the blocks illuminated by the seismic rays, applying a positivity constrain. The quality factors of the other blocks are constrained to Q_{mean}. At smaller scale, the inversion scheme, with $\mathbf{m}_y$=Q_y^{-1}, $y < u$, and the same data vector, can be written as:

$$\mathbf{d} = \mathbf{G}_y\mathbf{m}_y. \tag{2.41}$$

Being $y < u$, the resolution is higher, as well as the number of blocks that must be solved. Some part of the area may not be solved at the higher resolution; the non-uniform cell inversion scheme allows to preserve the quality factors obtained in the previous steps for these volumes. The two inversion schemes of formula (2.40)

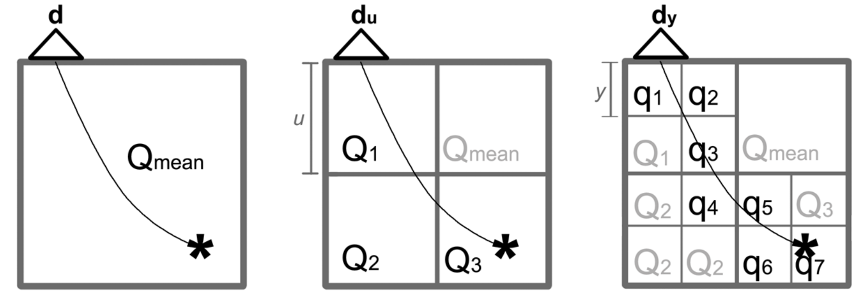

Figure 2.3: The multi-scale algorithm is described using a single earthquake (asterisk) and station (triangle). (left)The starting data vector of the multi-step process, d, can be used to obtain the average quality factor of the entire medium (Q_{mean}). (center) At the u resolution, the data vector d_u is updated with the "attenuation per ray" measurable from the previous step. The quality factor of the blocks crossed by the ray are measured, while the other quality factors remain Q_{mean}. (right) The same as (b) for the y resolution. d_y is updated with the "attenuation per ray" measurable from the previous step.

and formula (2.41) may be defined as a single inversion problem, to be solved with the singular value decomposition (Menke, 1984).

A process of updating of the data vector is included in the inversion scheme at higher resolutions, with the aim of adding the information acquired at a lower resolution to the higher resolution inversion problem. Referring to Figure 2.3b, at the u resolution, a data vector affected by the average attenuation (e. g. obtained in a previous step) is considered. So, the data vector $\mathbf{d}_u$ can be defined as the sum of the data vector ($\mathbf{d}$) obtained with the CN method and the "attenuation per ray" due to the average quality factor ($\boldsymbol{\varphi}_u$):

$$\mathbf{d}_u = \mathbf{d} - \boldsymbol{\varphi}_u = \mathbf{G}_u\mathbf{m}_u. \tag{2.42}$$

The model parameters ($\mathbf{m}_u$) at this step are the variation of the quality factors in each block respect to the average quality factors. The "attenuation per ray" at this step is a function of the average quality factor and the ratio of the length of the segments in the blocks of side u with the slowness in the same blocks (look at Appendix A for more details). In the same way, an higher resolution data, $\mathbf{d}_y$ (Figure 2.3c), can be defined as the sum of the data from the CN method ($\mathbf{d}$) and the "attenuation per ray", caused by the distribution of the quality factors at the lower resolution ($\boldsymbol{\varphi}_y$):

$$\mathbf{d}_u = \mathbf{d} - \boldsymbol{\varphi}_y = \mathbf{G}_y \mathbf{m}_y. \tag{2.43}$$

$\mathbf{m}_y = \mathbf{q}_y = \Delta Q_y^{-1}$ is the variation of the quality factors from the quality factor found at a lower resolution. The "attenuation per ray" at this step is a function of the quality factors obtained at the u resolution and the ratio of the length of the segments in the blocks of side y with the slowness in the same blocks (look at Appendix A for more details). This process allows the solution of the inversion problem at a low resolution, with poor ray coverage, and the solution of the inversion problem in a smaller area with high ray-coverage.

At each step, a minimum number of rays (n_R) crossing the blocks to allow an over-determined problem must be defined. The number of rays considered at each resolution is defined using an empirical master equation, dependent on the wavelength used to image the area:

$$n_R \geq \Upsilon \frac{Block\_side}{\lambda}. \tag{2.44}$$

The coefficient Υ is empirically determined in each area, because of the source-station distribution and the data quality. The updating algorithm requires a finer inversion technique than the one required by the single scale problem. A Newton method for minimizing the 2-norm subject to lower bounds (the total quality factors must always be positive) is adopted. This reflective Newton approach (widely described in Coleman and Li (1992)) which is not sensitive to starting value, is particularly suitable for the large-scale problems, that arise considering matrices that are sparser as one increases resolution. The algorithm generates a sequence of strictly feasible iterates, which converges under standard assumptions to a local solution at a quadratic rate. The 2-norm problem is rewritten in an equivalent form:

$$\min_{m} \{ q(\mathbf{m}_q) = -\mathbf{G}^T \mathbf{d}_q \mathbf{m}_q + \frac{1}{2} m^T \mathbf{G}^T \mathbf{m}_q : \mathbf{l} \leq \mathbf{m}_q \}, \tag{2.45}$$

where $\mathbf{l}$ is a vector whose components are the lower bounds that constrain the total quality factor of each block to be positive. The algorithm then generates a descent direction for $q(\mathbf{m}_q)$, and follows a piecewise linear path, reflecting off constraints as they are encountered. The nonnegative least square method applied to single scale tomography requires strict decrease in a piecewise quadratic dual function, whereas the new method generates feasible iterates, requiring strict decrease in the original quadratic function q.

The covariance matrix associated to this inversion contains the variance of each unknown and the covariance of each pair of unknowns. The semidefinite least-square covariance, anyway, is not easy to be found, even if some algorithm for calibration and adjustment of the covariance matrix for this problem have been developed in recent years (Malick, 2005, Boyd and Xiao, 2005). For sake of simplicity a bootstrap approach is adopted in order to estimate the error on the model parameters in any application of multi-resolution tomography (sections 3.3.5 and section 3.6.5).

In Appendix A, the three-step and two-step tomography algorithms applied to the data obtained at Mt. Vesuvius and Campi Flegrei, respectively, are fully described.

Chapter 3

Attenuation tomography of the Neapolitan volcanoes

This chapter develops and details the results obtained in four accepted or submitted publications in journals (Del Pezzo et al. 2006a, Petrosino et al. 2008, De Siena et al. 2008, De Siena et al. submitted to JGR); these papers are aimed at giving an image of the shallow crust materials at Mt. Vesuvius and Campi Flegrei volcanic areas, using P- and S-wave attenuation tomography at high frequency. The Mt. Vesuvius attenuation tomography has been performed first at a single scale resolution. Successive development of the multi-resolution technique led to a nonuniform cell size image of the area. The seismic attributes (total-Q inverse for each single path) are obtained using the CN method (Aki, 1980a), and checked with the ordinary spectral-slope method (Sanders, 1993). Spectral slope is also used to estimate P-wave total Q-inverse. The same multi-resolution techniques applied to Mt. Vesuvius dataset has been applied to the Campi Flegrei area, using the CN method and the slope decay method for the S- and P- waves, respectively. The attenuation images for both areas are eventually compared with the available high resolution passive velocity tomography images (Scarpa et al. 2002, Battaglia et al., 2006). In each of these studies, the results achieved are widely discussed, in the framework of geological and seismological observations available from other sources.

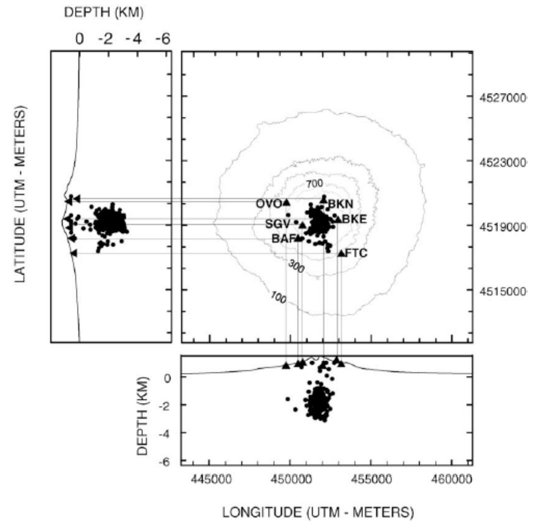

Figure 3.1: Map of Mt. Vesuvius with station positions (black triangles) and hypocentral locations (black circles). Upper-left and downward panels

3.1 Mt. Vesuvius

Mt. Vesuvius is a stratovolcano formed by an ancient caldera (Mt. Somma) and by a younger volcanic cone (Mt. Vesuvius). The volcanic complex is located in the Campanian plain (southern Italy) at the intersection of two main fault systems oriented NNW–SSE and NE–SW (Bianco et al., 1997); its formation is part of a wider convergence between the Euroasiatic and Hellenic plates, and is due in particular to the subduction of the Hellenic plate under the Hellenic and Calabrian arcs, while its structure is surrounded by carbonatic rocks of the Mesozoic Era (Tondi and Franco, 2003). The entire caldera presents annular faults formed in the last 18 ky (Cioni et al., 1994). The volcanic structure of Mt. Somma, which collapsed in five different phases, is mainly composed of residual lava, and minor wastes. The oldest surface products date back to 25 ky ago (Andronico et al., 1995), while the oldest lava found at a maximum depth of 1125 m dates back to 373 ky ago. The Mt. Vesuvius volcanic cone raised because of the volcanic activity following eruption in 472 a. C. The height of the volcano is 1200 m above sea level (a. s. l.); the diameter and depth of the crater contained in the volcanic structure are about 450 m and 330 m depth, respectively. The form of the volcanic

Station	Latitude (°)	Longitude (°)	altitude (a.s.l.) (m)
BKEM	40.4909	14.2633	0.863
FTCM	40.4778	14.2636	0.350
BAFM	40.4872	14.2471	0.594
SGVM	40.4906	14.2485	0.734
BKNM	40.4977	14.2578	0.865
OVO	40.4965	14.2380	0.584

Table 3.1: Seismic stations used in the single scale tomography.

complex presents two spires, with the crater axis shifted south-west of the axis of Mt. Somma, that surrounds the cone of Mt. Vesuvius by means of two valleys.

The volcanic activity is dated back to 300–500 ky (Sanntacroce, 1993) and is characterized by both effusive and explosive regimes , in strong correlation with the status of the magmatic conduit; its obstruction provokes a momentary interruption of the eruptive activity, followed by explosive eruptions (Scandone et al., 1993)). Three different eruptive cycle may be reconstructed through the volcanological studies at Mt. Vesuvius volcanic complex (Andronico et al. 1995). The first one caused the formation of Mt. Somma and is comprehended between 23000 y and 9500 y b. C. The second cycle took place between 9500 y b. C. and 79 y a. C., and presented by three Plinian and six sub-Plinian eruptions, spaced out with lengthy open conduits periods (Scandone et al. 1993). The eruption of Avellino (1500 b. C.) is the main event of this period, that gave to Mt. Vesuvius the shape of a caldera for the first time; it shattered the western part cone of the volcano,as a consequence of the outflow of a magmatic and water vapor filled flux from the conduit just before unblocked. The following landslide in the eastern part of the complex gave to the volcano a single spire form. The third cycle (79 a. C. - today) presents three sub-Plinian eruptions (472, 512, 1631 a. C.); each of this events was preceded by quiescent stages, effusive and explosive eruptions and strombolian activity. After a long quiescent stage, the eruption in 1631 a. C. (the first one foreseen by the observation of the new seismic activity (W., 1756–1794)) caused the fracture of the feeding conduit, that became an open conduit between the magmatic chambers and the surface. The following 300 years are characterized by 17 minor cycles of strombolian and mixed effusive-explosive type, variable during 7 and 30 y (Bonasia et al., 1985). The last eruption, in March 1944, was effusive

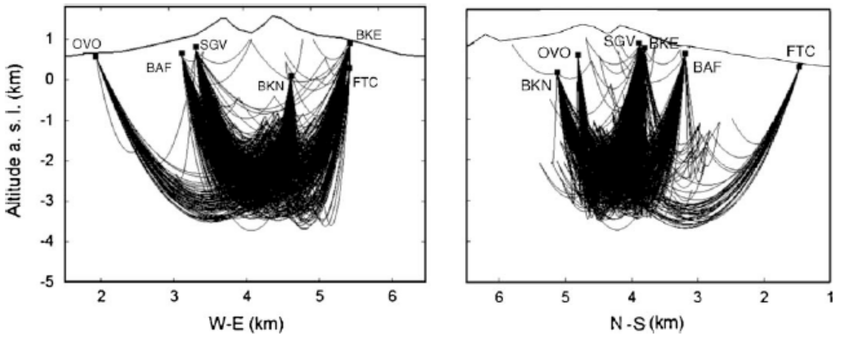

Figure 3.2: Ray-path projections on E-W and N-S sections of Mt. Vesuvius

(Berrino et al., 1993). It may have started a new obstructed conduct phase and hence a quiescent stage.

The seismic activity is at now the unique indicator of the internal dynamics (see e.g. De Natale et al. (1998)). Seismicity studies are of extreme importance for the high risk volcanic area of Mt. Vesuvius. As an overall, the seismicity of Mt. Vesuvius is characterized by a mean rate of approximately 300 events per year. The largest earthquake in the area [reasonably since the last eruption -1944- see Del Pezzo et al. (2004)] occurred in 1999, and has been associated with regional and local stress fields (Bianco et al. 1997). The main features of the earthquake space and time distribution are described in the papers by Scarpa et al. (2002) and Del Pezzo et al. (2004). In the study of Scarpa et al. (2002) the relocated seismicity appears to extend down to 5 km below the central crater, with most of the energy (up to local magnitude 3.6) clustered in a volume spanning 2 km in depth, positioned at the border between the limestone basement and the volcanic edifice. The hypocentral locations for the data used at Mt. Vesuvius in the present chapter show the same pattern of the overall seismicity (Figure 3.1). The earthquakes recorded at Mt. Vesuvius are mostly of volcano-tectonic type (VT) (Chouet, 2003), with fault-plane orientations, showing an highly non-regular spatial pattern. The spectral content of the P- and S-wave trains of the VT events is compatible with stress drops spanning a range between 1 and 100 bars (100 bars for the largest magnitude) and focal dimensions of the order of 100 m (Del Pezzo et al., 2004).

The velocity structure beneath Mt. Vesuvius, in the depth range from the Earth surface to 10 km, has been deduced by seismic tomography (Auger et al., 2001, Scarpa et al. 2002). Auger et al. (2001) suggest the presence of a melting zone at a depth of about 8 km, on the base of the TOMOVES experiment results (see the book by Capuano et al. (2003) and the numerous references therein). At smaller scale (resolution of 300 m), between the topographical surface and 5 km of depth, Scarpa et al. (2002) evidence a low velocity contrast between 1 and 2 km depth, possibly associated with the presence of aquifers. No shallow and small magma chambers are visible at the resolution scale reached by Scarpa et al. (2002). A carbonatic basement having its top at around 2 km depth has been imaged by the tomographic studies, and confirms the observations of Zollo et al. (1996), based on an experiment on the seismic reflection of S-waves. The top of the basement has been constrained by perforation data.

An high positive magnetization zone has been imaged below the central cone (Fedi et al., 1998), and has been correlated with the high susceptivity of highly mineralized volcanic rocks at low temperature. Electromagnetic and magnetotellurics studies on Mt. Somma evidenced a migration of the volcanic activity along an east-west fractured system, together with a strong positive anomaly between 600 m and 2000 m (Di Maio et al., 1998). No significant variations in the gravimetric and deformation fields have been observed in the last 27 y.

3.2 Single scale attenuation tomography

In section 2.2.2 the CN method is adapted to estimate single path S-wave attenuation. In this section [see also Del Pezzo et al., 2006a] an application of this method to the volcanic structure of Mt. Vesuvius is presented. An high resolution

$-\Delta f$	$f_c(Hz)$	$+\Delta f$
2.4	3	3.6
4.7	6	7.2
8.2	12	15.8
12.4	18	23.6

Table 3.2: Frequency bands in which the results have been obtained

$3D$ model of the S-wave attenuation is obtained using 332 volcano-tectonic earthquakes located close to the crater axis in a depth range between 1 and 4 km (below the sea level). A parabolic ray-tracing is used, in the high resolution $3D$ velocity model which was previously estimated using almost the same data set. A linear inversion scheme is solved using the 2-squared norm with positive constraints in 900 m-side cubic blocks, obtaining the estimate of Q_S^{-1} for each block. Robustness and stability of the results are tested changing in turn the input data set and the inversion technique. Resolution is tested with both checkerboard and spike tests. Results show that the attenuation structure resembles the velocity structure at this resolution, reproducing well the interface between the carbonates and the overlying volcanic rocks which form the volcano. Analysis is well resolved till to a depth of about 4 km. Higher Q contrast is found for the block overlying the carbonate basement and close to the crater axis, almost coincident with a positive P-wave velocity contrast located in the same volume and previously interpreted as the residual high density body related to the last eruptions of Mt. Vesuvius. This high-Q zone is interpreted as the upper part of carbonate basement, in which most of the high energy seismicity takes place. The low-Q values found at shallow depth are interpreted as due to the high heterogeneity of the volcanic rocks, mainly caused by the mixing of lava layers and pyroclastic materials extruded during the last eruptions.

Station	fc = 3Hz	fc = 6Hz	fc = 12 Hz	fc = 18 Hz
BKEM	7.7	4.9	5.2	3.9
FTCM	8.1	5.3	3.7	4.2
SGVM	6.4	7.1	5.6	4.7
BKNM	8.0	4.7	5.9	4.7
OVO	7.0	6.8	6.5	6.4
-	-	-	-	-
g_0	1.9	2.1	1.6	1.5

Table 3.3: Q-coda inverse (x1000) estimated by Bianco et al. (1999b), and g, the average scattering coefficient, estimated by Del Pezzo et al. (2006b).

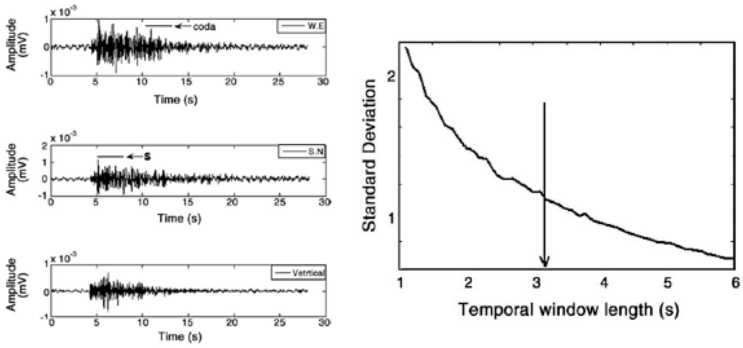

Figure 3.3: The standard deviation, σ, obtained calculating the average (over stations) of the log of spectral ratio between direct S radiation and coda radiation, after correcting the amplitudes for geometrical spreading and for the average Q, is represented in the lower panel as a function of the time window duration, for a quake recorded at all the stations (an example at BKE station is reported in the upper panel). Downward arrow indicate the empirically determined optimal window length.

3.2.1 Data selection and ray-tracing

The waveforms used in the single resolution tomography of Mt. Vesuvius are recorded at five digital, high dynamic (120 dB, gain ranging), 1 Hz, three component seismic stations with the addition of the data coming from the analogical station OVO (66 dB dynamic range, three component), in operation since 1972 at the historical building of Vesuvius Observatory. Digital stations are sampled at 125 s.p.s. whereas at OVO the sampling rate is set at 100 s.p.s. Analog antialiasing filter with 25 Hz cut-off frequency operated on all the data logger prior to sampling. The time period investigated is January – September 1999 and January – June 2000. The total number of waveforms resulted to be 959 (a sample registration of a three component earthquake is presented in Figure 3.3). In Table 3.1 station names and coordinates are reported. Location of the 332 earthquakes (Figure 3.1) are obtained with a non linear procedure which uses a gridsearch algorithm (Lomax et al., 2001) using a $3D$ velocity model based on results by Scarpa et al. (2002). The 332 earthquakes are selected on the base of the best signal to noise ratio, absence in the waveforms of spikes and other disturbances, coda lasting at least till to 15 s lapse time from earthquake origin time. In doing this selection, all the events with a localization error larger than 0.3 km are discarded;

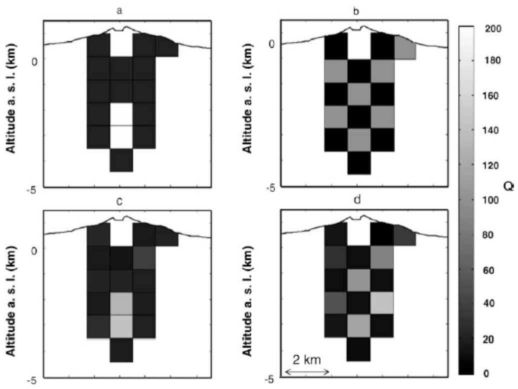

Figure 3.4: Resolution tests based on two synthetic images. Panel a represents a high Q-contrast block, 0.9 km×1.8 km located in central position respect to the crater; panel b represents a checkerboard structure, with high Q-contrast among the blocks. Test results (respectively panels c and d) reproduce the input values within less than 30% of uncertainty for cells crossed by a minimum of 40 rays. Grey scale represents the Q-value scale utilized.

the magnitude of all the events is implicitly restricted in the range from 1.8 to 3.0, as in the coda of the earthquakes with $M > 3.0$ small aftershocks are often present.

The parabolic ray-tracing technique described in section 2.2.1 is used to compute wave trajectories in the same velocity model utilized in the location procedure. The best-adapted parabolas are numerically searched in the vertical plane connecting source and station, satisfying the Fermat's principle of minimum travel time (Figure 3.2). Ray length range from 0.5 to 7 km, corresponding to S-travel times from 0.3 to 3.9 s. An analytical representation of the ray-paths (three coefficients for each ray) is obtained, allowing to save computer time in the inversion process. The parabola coefficients for each source–receiver pair are stored in a data base, successively used for calculations.

3.2.2 Test of independence from radiation pattern

The variations of the logarithm of spectral ratio (pre-multiplied for the ray-lengths) in formula 2.12, R_{ij}, are visually observed changing the direct S-wave window duration. For duration of more than 3 s, R_{ij} does not significantly vary with the window length. This should imply that:

Block#	1	2	3	4	5	6	7	8
Robustness								
Q	33	29	185	72	122	139	262	440
σ (from Covariance)	1	1	3	8	20	14	20	110
σ, 5% of data reduction	1	1	5	16	17	34	35	119
σ, 10% of data reduction	1	1	7	19	27	42	43	169
σ, 20% of data reduction	4	7	7	23	57	64	76	220
σ, 30% of data reduction	304	97	157	29	349	202	115	283
Stability test								
Q	33	29	185	72	122	139	262	440
Q, $g_{\min}$	33	29	185	72	122	139	262	439
Q, $g_{\min}$	33	29	185	72	121	138	263	440

Table 3.4: Robusteness and stability. The upper table reports for eight blocks the estimate of Q from the inversion process applied to the entire data set (first row), the variance of this estimate (second row) and the variances calculated from the tests applied to a reducted number of equations. Till to a 20 per cent of reduction results show robusteness in the solution. The lower table reports for the same eight blocks the values of Q from the inversion process (upper row) and those obtained fixing the g0 value at the extremes of the confidence interval.

- a certain stability for the estimate of R_{ij} is reached for 3 s window duration,
- the phenomenological model described in section 2.2.2 is confirmed in the area of Mt. Vesuvius.

As a second test, the measure of the variation in the spectral energy due to the source radiation pattern (the quantity defined by formula 2.8 in section 2.2.2) can be defined. Few events among those with high signal to noise ratio are selected at all the stations. The amplitudes are corrected for geometrical spreading and for the average Q already estimated for the same area by Bianco et al. (1999) (see Table 3.3).

The log of spectral ratio between direct S radiation and coda radiation are estimated for each station, averaging over the two horizontal components of the ground motion. Coda windows started at lapse time of 8 s and ended at 12 s. After averaging over the stations the standard deviation was estimated. This procedure was repeated for different values of time duration of the S-wave window. As an example, in Figure 3.3, σ is plotted as a function of the time window duration for a quake recorded at all stations. From the pattern of σ it was visually deduced that,

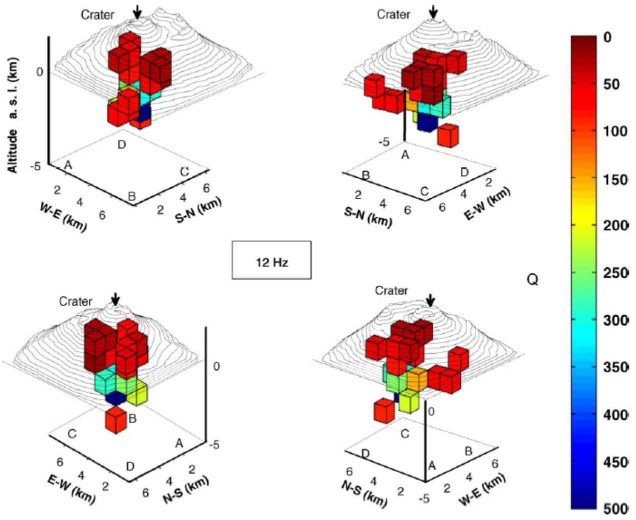

Figure 3.5: Tomography results, obtained for the frequency band centered at 12 Hz. We use four different perspectives, each one shifted by 90○. The main features of the attenuation structure of Mt. Vesuvius are essentially a laterally uniform low Q region in the first 1.8 km of crust (from the top) under the volcano, and a heterogeneous Q-structure below this depth.

after around 3 s of duration, the standard deviation of the spectral ratio averaged over the stations falled below 70% of the maximum. Interpreting the fluctuations around the average as mainly produced by radiation pattern effects, this pattern was interpreted as an indirect confirmation of validity for the assumption made in the conceptual model described in section 2.2.2.

3.2.3 Robustness, stability and resolution tests

The optimal dimension of the cubic cell, together with the resolution of the method, are determined with a trial and error approach. The test is based on two synthetic images, the first consisting of a high Q-contrast block, 0.9 km×1.8 km located in central position respect to the crater (see Figure 3.4,a) and the second of a checkerboard structure, with high Q-contrast among the blocks (Fig. 3.4,b).

The ray-tracing is accomplished using the same configuration of sources and stations as that associated with the real data. The synthetic S-to-coda spectral ratios are calculated, adding log-normally distributed noise with a percent standard deviation of 15%. Finally, the inversion scheme described in section 2.2.2 is

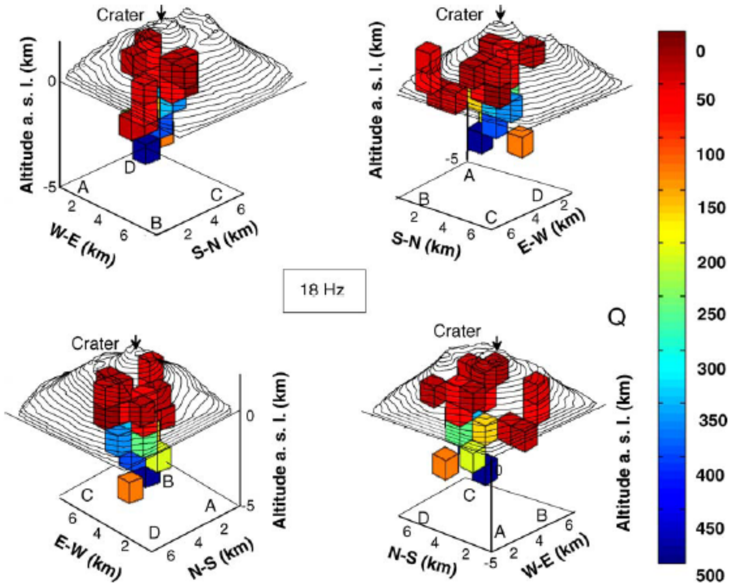

Figure 3.6: The same of Figure 3.5, for the frequency band centered at 18 Hz. In this frequency band, the high-Q zone located at approximately 3 km b.s.l.

applied and the minimum cell dimension is determined by trial and error (fulfilling the restriction that must be greater than the maximum wavelength, as already discussed above). The minimum cell dimension selected is the one that reasonably well reproduces the input image. In these test, it is empirically observed that the cells crossed by a minimum of 40 rays reproduce the input values within less than 30% uncertainty. The cell dimension of 0.9 km results to be optimal.

Fixing this volume cell dimension and representing the results for the sole cells crossed by more than 40 rays, the two synthetic images result well resolved (Figure 3.4,c and 3.4,d).The robustness of the method is tested using a bootstrap approach (Lees and Crosson, 1989, Tichelaar and Ruff, 1989). The number of equations in the inversion problem is reduced of 5%, 10%, 20% and 30% with a random extraction, obtaining, for each percent group, 100 data set. For each of these data set the inversion process is solved. The Q factor and its standard deviation are estimated for each block from the average of the 100 solutions. Then, these solutions are compared with the solution obtained from the whole data set. A significative increase in standard deviation for the random extraction of 30% of data is observed, whereas for that obtained for 5%, 10% and 20% the standard deviation is comparable with that from the entire data set. In Table 3.4, the output of this test (obtained at 18 Hz central frequency) is reported for a number of eight selected blocks. Stability of the solution is indirectly tested by changing the value of the constant $C(f)$ in formula (2.14), letting g_0 of formula (2.11) to vary between the values of $g_{min} = 1$ and $g_{max} = 2.5$, that represent the error limits of this estimates as reported by Del Pezzo et al. (2006b). Results from these tests ensure that the solution obtained is practically insensitive to $C(f)$, as reported in Table 3.4 for the same suite of eight selected blocks to whom the robusteness test has been applied.

3.2.4 Results

In Figures 3.5 and 3.6, the results obtained for the frequency bands centered at 12 and 18 Hz are shown (the frequency bands are shown in Table 3.2). In the band centered at 6 Hz, the signal to noise ratio at 12 s lapse time is often below the threshold. This implies considering a limited data set for the inversion. Consequently, results for the band centered at 6 Hz show that, in this frequency range, only few blocks can be resolved, and consequently are not considered here. The main features of the attenuation structure of Mt. Vesuvius are essentially a laterally uniform low Q region in the first 1.8 km from the top of the volcano and an heterogeneous Q-structure below this depth. In the W-E sections (Figure 3.7) an high Q zone (blue and green colored blocks) centrally located respect to the crater axis, surrounded by lower-Q blocks can be easily visualized.

The results obtained at 18 Hz are better defined than those at 12 Hz, showing five additional resolved blocks. The high Q contrast blocks are distributed in space similarly to the high velocity zones inferred by the travel time velocity tomography (Scarpa et al. 2002) which has been utilized in the present study for the ray tracing. The velocity tomography was performed at a better resolution (300 m) and its results are reported in the same figures for sake of comparison. The high velocity zone has been interpreted by Scarpa et al. (2002) as the upper part of the limestone basement. It is consistent with the depth of the limestone top retrieved from active seismic tomography underneath Mt. Vesuvius using the TOMOVES data set (Zollo

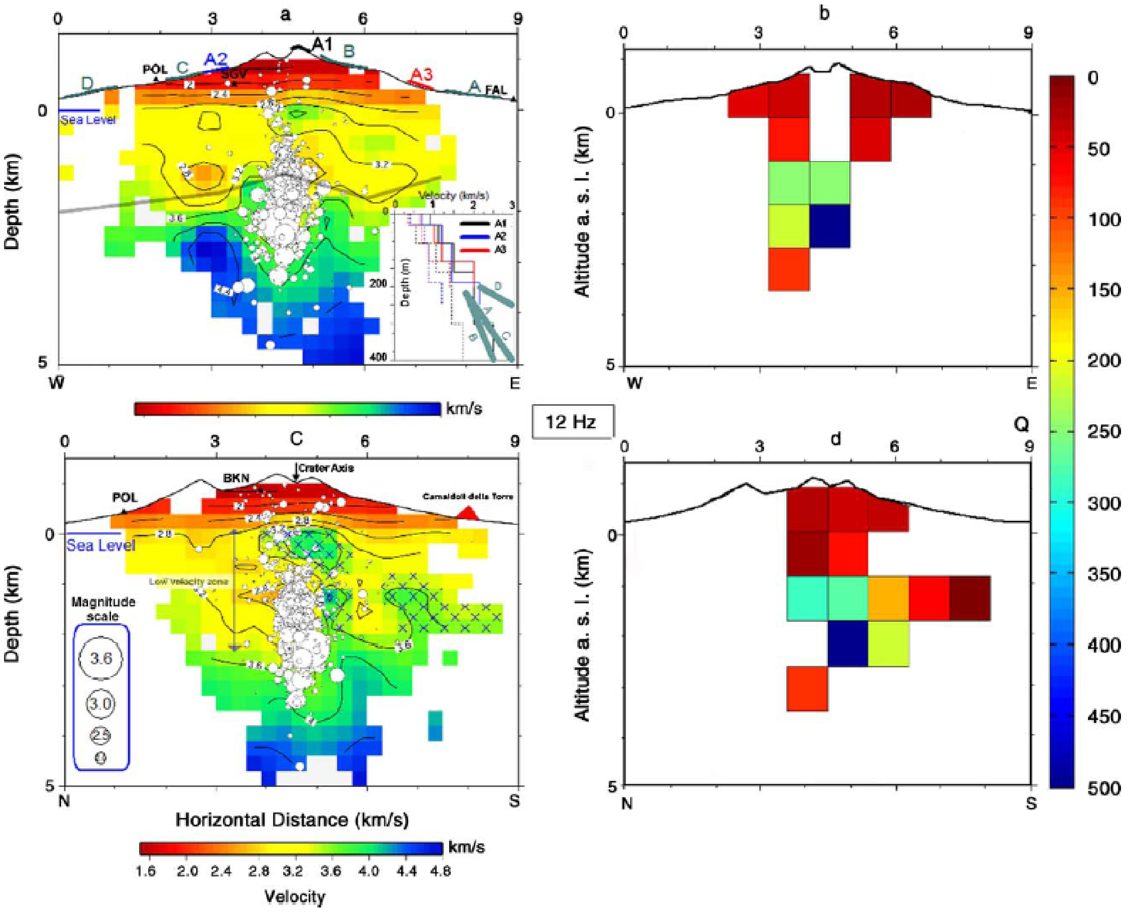

Figure 3.7: Q-tomography results, obtained for the frequency band centered at 12 Hz, representing W-E (panel b) and S-N (panel d) sections of the earth structure. The high Q contrast blocks have a pattern similar to that of the high velocity zones in the (a) W-E and (c) N-S cross sections of the P-wave velocity structure inferred by the travel time tomography (Scarpa et al. 2002). In panels a and c white circles show the relocated hypocenters having size proportional to magnitude and the low velocity layer toward N is linked to the deepening of the limestone basement.

et al., 2002).

3.3 Multi scale attenuation tomography

In the previous section, the three-dimensional S-wave attenuation tomography of Mt. Vesuvius has been obtained with multiple measurements of coda-normalized S-wave spectra of local small magnitude earthquakes. The resolution achieved in the whole area is 900 m, lower than the resolution of the velocity tomography (300 m). In this section, an application of the multi-resolution technique (section 2.4.2) to the seismic attributes obtained with the CN method in the same area is presented. The data-set has been strongly increased to apply the technique: 6609 waveforms, relative to 826 volcano-tectonic earthquakes, always located between 1 and 4 km (below the sea level) under the central cone have been used. A sixth 3-component digital seismic station (named POL) has also been added. Moreover, the two-point Thurber modified numeric ray-tracing, described in section 2.2.1 has been adopted; rays are traced in the same high resolution 3-D velocity model. The spatial resolution achieved in the attenuation tomography becomes now comparable with that of the velocity tomography (300 m side cubic cells are resolved). Moreover, a new statistical test performed on the results ensures that they are almost independent of the radiation pattern effects. The improvement of the ordinary spectral-slope method described in section (2.3.1) has also been applied both to P- and S-waves, in order to check the results of the coda-normalization method and compare the S attenuation image with the P attenuation image. The main innovation is the application of the multiple resolution approach to the inversion of the spectral data. The techniques and results in the following section are also discussed in De Siena et al. (2008).

3.3.1 Data selection and ray tracing

In the present work, 6609 waveforms were utilized, obtained from a selection of 826 earthquakes recorded from January 1996 to June 2000 at seven 3-component stations, that are the analogical station OVO (66 dB dynamic range, three component) sampled at 100 s.p.s. and 6 digital, high dynamic (120 dB, gain ranging),

Station	E-W (UTM)	N-S (UTM)	altitude (a.s.l.) (m)
BAFM	450372	4518076	594
BKEM	452677	4518762	850
BKNM	451875	4520020	865
FTCM	452692	4516337	350
OVO	449190	4519705	600
POLM	447910	4522499	181
SGVM	450568	4518706	734

Table 3.5: Seismic stations used in the multiple scale tomography.

1 Hz , seismic stations sampled at 125 s.p.s. (Table 3.5).

Analog anti-aliasing filter with 25 Hz cut-off frequency operated on all the data logger prior to sampling. The data selection has been made on the base of the the same pre-requisites described in section 3.2.1. The magnitude was also implicitly restricted in the range from 1.6 to 3.0, because small aftershocks are often present in the coda of larger events. Moreover, the location of the 826 earthquakes (Figure 3.8) was obtained using P-picking of all the available seismic stations constituting the monitoring network (www.ov.ingv.it) with the same non linear procedure used for the single resolution tomography (Lomax et al., 2001).

The Thurber-modified numeric approach (Block, 1991), described in section 2.2.1, has been used to trace the path of each ray in the 3-D velocity structure of Mt. Vesuvius obtained by Scarpa et al. (2002). This ray-bending method (Um and Thurber, 1987) works particularly well in velocity structures characterized by fairly sharp velocity variations, like that of Mt. Vesuvius. The only limitation is that the method does not compute reflected ray paths, that anyway are not taken into account in the present work. After dividing the whole structure to be investigated in three different grids (with 1800, 900 and 300 m cubic cell size, respectively) the length of each ray connecting each source to each receiver and the length of the ray-segments crossing each cell have been stored in a database.

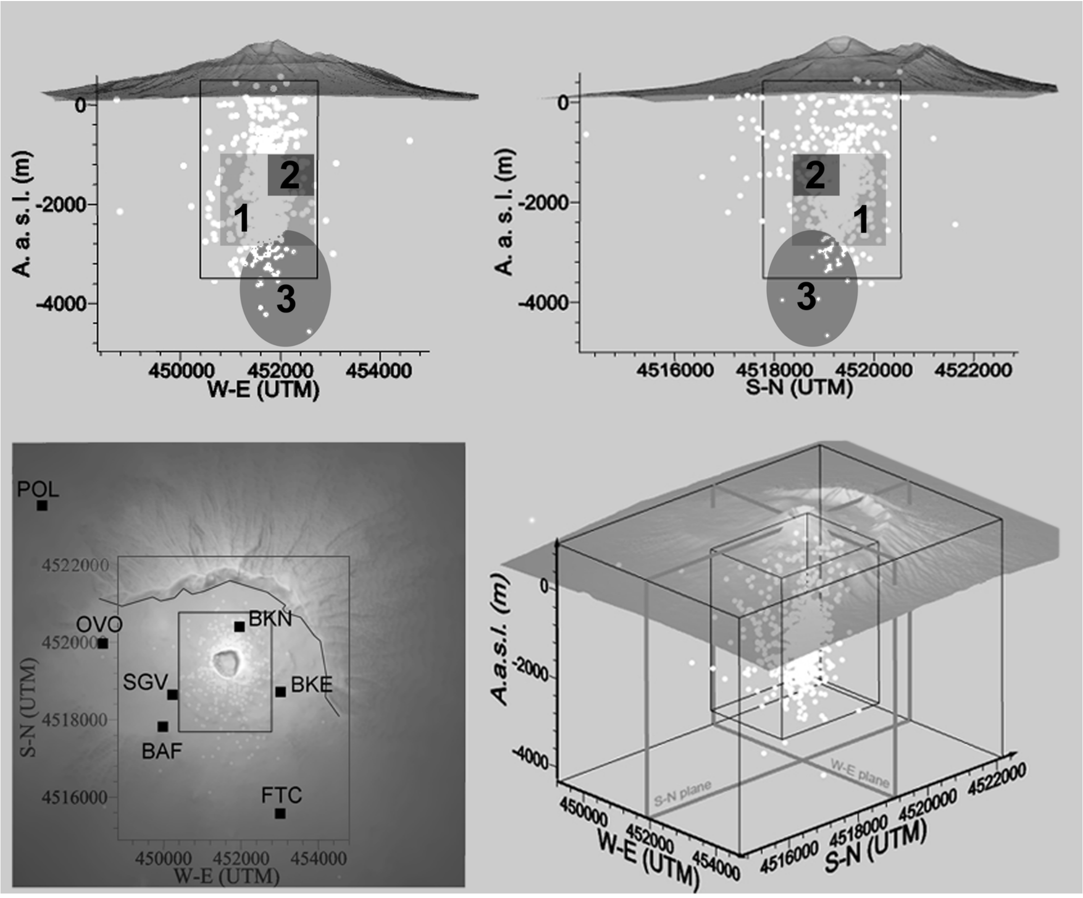

Figure 3.8: Lower-left panel: Map of Mt. Vesuvius with station positions (black squares) and hypocentral locations (white dots) of the seismic events used in the present work. Black broken line depicts the old caldera rim. Upper-left and upper-right panels represent respectively the W-E and S-N sections, also reported as "W-E plane" and "S-N plane" in the lower-right "wide angle" view. The High Resolution Region (HRR) is roughly depicted by the inner polyhedron in the wide angle view. The solid line rectangles in the upper left, upper right and lower left panels represent the sections of the HRR. The zones marked with 1and 2 represent the zone in which the robusteness test results are reported respectively in Table IV and V. The ellipsoidal zone marked with 3 shows the area with the maximum seismic energy release.

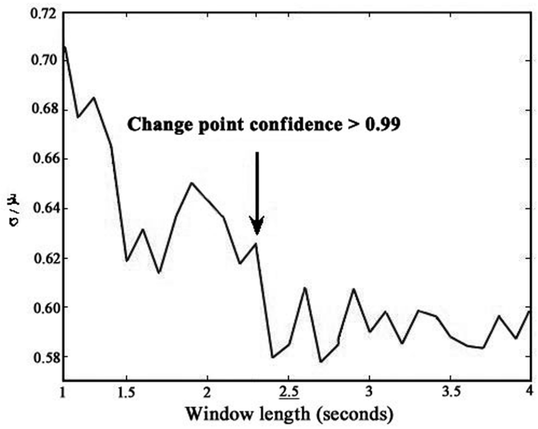

Figure 3.9: The percent standard deviation, σ/μ , as a function of the window duration for an earthquake recorded at all the stations. σ/μ is obtained calculating the average, μ [over stations], of the log of spectral ratio between direct S radiation and coda radiation, after correcting the amplitudes for geometrical spreading and for the average Q. Downward arrow indicates the change-point as discussed in the text.

3.3.2 The estimate of the seismic attributes with the CN method

The application of the CN method to attenuation tomography is fully described in section 2.2.2; we used the slightly modified inversion scheme described in section 2.3.1, where the model parameters are the variation respect to the average quality factor.This change is due to the presence of coda localization in the area (see e. g. Tramelli (2008b)), that do not affect the single path estimates of attenuation performed at Mt. Vesuvius, but could actually affect the estimate of average quality factor performed with this method.

Prior to the application of the CN method, the temporal stability of the S-wave time window for the radiation pattern effect has been checked with a statistical method. For each ray connecting the source to the receiver, the quantity D defined by formula 2.8 has been considered. D is implicitly only dependent on the radiation pattern effects. The percent standard deviation ($\sigma_D / < D >$) calculated averaging D over the stations for a single earthquake, is plotted for different time window durations in Figure 3.9; this quantity abruptly decreases with increasing duration of the time window, as it was also evident for the standard deviation of Figure

3.3. A statistical test [the "change point" test of (Mulargia and Tinti, 1985)] to estimate the "change point" of the pattern of D respect to the duration of the time window in which is calculated has been applied. The pattern results to be steady after 2.5 seconds at 99% confidence. Consequently, the radiation-pattern effects become negligible for time windows with a duration greater than 2.5 s. This result can be interpreted as due to the natural processes of averaging the radiation pattern effects that takes place in the ray-tube centered along the ray-path (Gusev and Abubakirov, 1999); the estimate of 2.5 s is different from the estimate of 3 s obtained on an empirical base in section (3.2.2). This is probably a more accurate estimate of the window length, due to the increase of the recording site and the effective accuracy of the new statistical test. For the above reasons $\theta_{ij}(\vartheta, \phi)$ of formula (2.7) may be assumed identically equal to unity. Accordingly, the duration of the S-wave time window has been set at 2.5 s, starting from 0.1 s before the S-wave arrival time.

The independence of frequency for the site term has been confirmed by Galluzzo et al. (2005), who studied the site transfer function at Mt. Vesuvius. The transfer function of the instruments is flat with frequency in the whole frequency range investigated. Formula (2.21) represents a linear system of N_k equations (the number of rays) in N_cells unknowns (the number of blocks to be solved) that can be inverted, as discussed in the next sections. Coda signal time window starts at 8 s lapse time and ends at 12 s, since most of our data show a favorable signal-to-noise ratio (>3) for lapse time smaller than 12 s. A Discrete Fourier Transform (DFT) is applied to the signals after windowing (a cosine taper window is used, with tapering at 10% both for S and coda) for both the horizontal components of the ground motion. The S spectral amplitude is calculated averaging in the frequency bands centered at the values of frequency, f_c, reported in Tab 3.6, with bandwidths ($\pm\Delta f$), and finally log-averaged over the components; thus the ratio between the S-wave spectrum and the coda spectrum is obtained. The natural logarithm of this ratio estimates d_k^C of formula (2.22). The constant in formula (2.20) has been already estimated by (Del Pezzo et al. 2006a) for the area under study.

$-\Delta f$	$f_c(Hz)$	$+\Delta f$
8.2	12	15.8
12.4	18	23.6

Table 3.6: Frequency bands in which the results have been obtained

3.3.3 The estimate of the seismic attributes with the SD method

The inversion scheme described in section 2.3.1 for the SD method has been applied to the same dataset to obtain the S- and P-wave attenuation images of the area. Direct S spectral amplitudes were obtained in the frequency band centered at $f_c = 18\ Hz$, with the same bandwidth used for the CN method (Table 3.6). The use of only this central frequency value is justified by the spectral features of the seismicity at Vesuvius like broadly discussed in section 3.2.4. A DFT is applied to windowed signals of length 2.5 seconds, starting from 0.1 s before the direct-S travel time, for both W-E and S-N components of the ground motion; then, the spectra are log-averaged over the components.

Spectral amplitude for P waves was calculated in a time window starting from the P-wave onset and ending at 0.1 s before the S-wave picking, tapering each spectrum with a 10% cosine taper function. The derivative was carried out for both S and P log-spectra, in the frequency band starting from corner frequency (around 10 Hz for the whole set of data) and ending at 23 Hz (before the cut-off frequency of the anti-alias filter that was set up at 25 Hz). The derivative was computed using MATLAB "diffnew" routine.

Block#	1	2	3	4	5	6	7	8	9	10	11	12
P^{1800}, 10%	1%	0%	0%	13%	7%	4%	0%	0,1%	0%	0%	0%	3%
P^{1800}, 20%	1%	0%	2%	29%	9%	11%	17%	1%	0%	0%	0%	3%
P^{1800}, 30%	2%	1%	3%	28%	9%	9%	50%	0,3%	0%	0%	0%	2%
P^{1800}, 40%	3%	3%	10%	29%	8%	16%	87%	2%	1%	0%	0%	8%
P^{1800}, 50%	6%	2%	11%	62%	20%	25%	87%	3%	1%	0%	0%	9%

Table 3.7: Robusteness Test - 1800 m: the average percentage of formula (3.14) is represented for all the blocks resolved.

3.3.4 Multi-resolution inversion

The resolution of the methods depends both on the wavelength (which has to be smaller than the cell size) and on the number of rays which sample the single cell, as discussed in section 2.4.2. A frequency $fc = 12$ Hz corresponds to a wavelength of about 200 m for S waves. For P waves (examined at 18 Hz only) the corresponding wavelength is of the order of 150 m. Taking a cell size of 300 m, it was evident that the blocks bordering the volume of investigation are crossed by a number of rays insufficient to ensure stability in the final solution, due to the distribution of the sources, concentrated along the crater axis and not uniformly distributed in space and depth inside the volume under investigation. This is the reason why it is not possible to invert the whole dataset using a uniform resolution of 300 m. Consequently, using the multi-resolution scheme, the solutions that can represent images in cells with a non-uniform size are searched, as other researchers do in velocity tomography (Thurber, 1987, Sambridge and Gudmundusson, 1998). In this approach, a relatively high-resolution can be obtained in a target area with a good ray coverage (this avoids linear dependence among the system formulas). To perform this task, the iterative process of updating of the data vector, also described in section 2.4.2 has been used in the inversion scheme. The idea of the iterative process of updating of the data vector has been fournished by its succesfull applications in velocity tomography (Thurber, 1987, Eberhart-Phillips, 1990, Bai and Greenhalgh, 2005), as also described in section 2.4.1. The results obtained

Block#	1	2	3	4	5	6	7	8
P^{900}, 10%	1%	15%	2%	1%	10%	1%	31%	1%
P^{900}, 20%	1%	13%	15%	1%	12%	8%	> 100%	1%
P^{900}, 30%	1%	21%	15%	1%	16%	9%	> 100%	1%
P^{900}, 40%	2%	53%	29%	2%	30%	7%	> 100%	2%
P^{900}, 50%	2%	58%	72%	2%	40%	11%	> 100%	2%

Table 3.8: Robusteness Test - 900 m: the average percentage of formula (3.14) is represented for the 8 blocks in which the single 1800 meters side block of Q-inverse = 0.0128 that includes the cone was divided. The increasing percentage in the first column is the data reduction.

in a lower resolution (LRR) are employed as input for highest resolution (HRR). Bai and Greenhalgh describe an inversion scheme of this kind, applied to velocity tomography. The application of the multi-resolution algorithm to the Mt. Vesuvius area is described in the following points.

1. The seismic attributes are calculated (both for the CN method and the SD method the same inversion procedure is applied) as described in the previous sections to obtain the data vectors.

2. The attenuation factor averaged over the whole volume under study, Q_T^{-1}, is estimated with the SD method. It results in a really good agreement with that estimated by the previous works in the same area (Bianco et al. 1999, Del Pezzo et al. 2006b).

3. The problem of formula (2.21) and (2.30) is solved for a volume divided in cubic blocks of 1800 m side, using a positivity constraint. Then, each 1800 m side block is divided in 8 blocks of 900 m side, and the inverse quality factors thus calculated, $(Q_b^{-1})^{1800}$, are assigned to each of this cubes.

4. The problem is solved for the 900 m cell size resolution, taking into consideration that each ray is characterized by the attenuation factor, which has been obtained by the solution of the previous step. In this way the new quantity $(\delta Q_b^{-1})^{900}$, which represents the variation from the inverse quality factor $(Q^{-1})^{1800}$assigned to the 900 meters block in the previous step, is obtained. As in the previous step, each 900 meters block is divided in 27 blocks of 300 m side, assigning to each of them the inverse quality factor $(Q_b^{-1})^{900}$. Also for this step a positivity constraint on the $(Q_b^{-1})^{900}$ is used.

5. Finally the problem for a 300 m side cell resolution is solved, obtaining $(\delta Q_b^{-1})^{300}$.

It is noteworthy that, whereas the data vectors and the coefficient matrices need to be recalculated at each scale, the inversion problem is always formally the same, and is given by formulas (2.21) and (2.30). The details regarding how the data vectors and coefficient matrices are upgraded at each scale are reported in Appendix A.1. It is also important to note that, at each step, the master equation is used. The coefficient $\Upsilon = 2$ is empirically determined. So, only the solutions for the blocks in which the number of ray-segments , n_R, is given by:

$$n_R \geq \frac{2Block\_side}{\lambda} \tag{3.1}$$

are obtained. This empirically determined threshold would ensure, in the assumption that the directions of ray-segments are randomly distributed in each block, that each block is homogeneously sampled.

3.3.5 Robustness, stability, checkerboard and synthetic anomaly tests

a) Robustness

The robustness of the method is tested using a bootstrap approach, reducing randomly the number of available formulas (rays), using the same test applied in section 3.2.3 to all the blocks at each cell size. The solutions for blocks of 1800 meters side were obtained for progressive reductions of the formulas used to solve the inverse problem; at each step the quantity:

$$P = \frac{Q_b(0) - Q_b(\%)}{Q_b(0)} \times 100 \tag{3.2}$$

is measured, where $Q_b(\%)$ is the total quality factor of the block b obtained for the reduced data set, whereas $Q_b(0)$ is the solution obtained using the whole database. The inversion is repeated 100 times for each data reduction, measuring then the

Block#	1	2	3	4	5	6	7	8
P^{300}, 10%	12%	16%	21%	59%	30%	5%	1%	14%
P^{300}, 20%	37%	90%	54%	99%	17%	48%	90%	70%
P^{300}, 30%	> 100%	> 100%	67%	> 100%	69%	> 100%	98%	> 100%

Table 3.9: Robusteness Test - 300 m: the average percentage of formula (3.14) is represented for the 8 blocks in which the single 900 meters side block of Q-inverse = 0.0110. The increasing percentage in the first column is the data reduction.

average percentage . In most of the cases, a significant increase of the percentage for a reduction of more then 40% of the data-set is observed. The results for all the blocks of 1800 meters side solved are reported in Table 3.7.

The increasing percentage in the first column is the data reduction.The same procedure is repeated for each scale, i.e. the quantity P of formula (3.2) is measured for all the 900 meters side blocks. A significant change in the value of P and a significant reduction of the average blocks resolved is evident for a random extraction of more than 40% of data. For sake of synthesis, in Table 3.8, the results obtained for 8 blocks contained in a single 1800-side block (which resulted to be characterized by $(Q_b^{1800})^{-1} = 0.0128$) are reported; its position is shown in the upper panels of Figure 3.8, using the light grey square evidenced by number **2**. The results for the other 900 m side blocks solved by the inversion are similar.

Finally, the variations of P calculated with formula (3.2) for all the 300 meters side blocks are compared. A significant change in the value of the parameter models and a significant reduction in the average number of blocks resolved is evident for the random extraction of more than 20% of data. In Table 3.9 a selection of 8 blocks of 300 meters, contained in the singular block of 900 meters side having $(Q_b^{900})^{-1} = 0.011$, is reported (the position of the 900 meters block is shown in the upper panels of Figure 3.8, using the dark grey square evidenced by number **1**).

b) Stability

The stability of the method is checked by changing the value of the constants in formulas (2.22) and (2.31). In formula (2.22) g_0 has been left able to vary between the values of $g_{\min} = 1$ and $g_{\max} = 2.5$, that represent the error limits of the average g, as reported in (Del Pezzo et al. 2006b). In formula (2.31) $< \frac{t_k}{Q_k} >$ has been left

Block#	1	2	3	4	5	6	7	8	9	12
$[(Q^{1800})^{-1}] \times 10^{-2}$	1,98	1,79	1,50	2,44	1,28	1,37	0,92	2,86	0,51	3,16
$[(Q^{1800})^{-1}] \times 10^{-2}, (Q_T^{\min})^{-1}$	1,83	1,67	1,72	1,84	1,28	1,43	1,15	2,72	0,49	3,21
$[(Q^{1800})^{-1}] \times 10^{-2}, (Q_T^{\max})^{-1}$	1,88	1.69	1,10	2,88	1,11	1,08	0,54	2,74	0,40	2,81

Table 3.10: Stability Test - 1800 m: the value of the inverse quality factor of each resolved block is dependent on the maximum (0.026) and minimum (0.008) average inverse quality factor allowed.

able to vary in the interval $[-3\sigma + <\frac{t_k}{Q_k}>\ ,\ +3\sigma + <\frac{t_k}{Q_k}>]$. The results do not change significantly.

A second stability test has been performed, varying Q_T^{-1} in both (2.22) and (2.31) in the interval $[-3\sigma + Q_T^{-1}\ ,\ +3\sigma + Q_T^{-1}]$. For the resolution of 1800 m, the variations of each parameter model obtained for the extreme values are reported in Table 3.10. For the intermediate resolution (900 meters) the same procedure is repeated, setting the maximum and minimum values of $(Q^{1800})^{-1}$ and ${Q_T}^{-1}$ sampled in their confidence interval (3σ). The 8 blocks considered in Table 3.11 are the same of Table 3.8. For the maximum available resolution (300 meters), the results obtained changing the values of Q_T^{-1}, $(Q_b^{1800})^{-1}$ and $(Q_b^{900})^{-1}$ in their confidence interval have been used with the same procedure. The results are shown in Table 3.12 for the 8 blocks considered in Table 3.9.

c) Checkerboard inside the HRR

The results of the CN inversion scheme have been tested imposing an a priori attenuation structure to the area: an homogeneous medium in the LRR and a checkerboard distribution of the quality factors in the volume where the HRR is located are assumed. The blocks crossed by at least 5 rays per block are the only one solved, following formula (3.1). Using the CN method, the true spectral ratios are calculated; then, a Gaussian random error calculated with a random number generator with zero mean and 10% sigma is added to these values.

The synthetic structure results to be extremely well resolved in the central part, whereas the quality of the reproduction of the input values decreases toward the borders of the volume under investigation. The checkerboard test results (Figures 3.10 and 3.11) are shown both for the W-E and S-N sections already shown in

Block#	1	2	3	4	5	6	7	8
$[(Q^{900})^{-1}] \times 10^{-2}$	1,79	0,52	0,96	1,79	2,75	1,64	0	1,79
$[(Q^{900})^{-1}] \times 10^{-2}, (Q_T^{\min})^{-1}, (Q_{b\,\min}^{1800})^{-1}$	1,88	0,46	1,12	1,88	2,36	1,77	0	1,88
$[(Q^{900})^{-1}] \times 10^{-2}, (Q_T^{\max})^{-1}, (Q_{b\,\max}^{1800})^{-1}$	1.67	0,58	0,80	1,67	3,14	1,51	0	1,67

Table 3.11: Stability Test - 900 m: the value of the inverse quality factor of each resolved block is dependent on both the maximum (0.026) and minimum (0.008) average inverse quality factor allowed, and the maximum (0.0188) and minimum (0.0167) inverse quality factor of the block in which they are contained.

Figure 3.8, and for five horizontal slices in the depth range between -500 to -3500 m.

In Figure 3.10, it can be noticed that the input checkerboard structure (W-E and S-N sections in panel a)) is well reproduced everywhere except in a small area toward N-E, corresponding to the geological structure of Mt. Somma (the same sections in panel b)); this is due to the lack of seismic sensors in this area. The negative variations in the inverse quality factors under -3000 meters sometimes explode, always reconstructing well the zones with low Q_S^{-1}. In Figure 3.11, the five panels on the left present five horizontal sections of the volume containing the input checkerboard structure, imaging the HRR (see also Figure 3.8, downward left panel); the good resolution achievable by the method used is evident in the volume constrained between 0 and -2700 m (right panels of the same figure). At $Z = -3500$ m, the volume resolved at the maximum resolution heavily decreases. Both in Figure 3.10 and Figure 3.11, the effective HRR obtained using this test is marked with a white broken line.

d) Synthetic anomaly

Following Shurr et al. (2003)(Schurr et al. 2003) a second test is performed using synthetic data by tracing rays through the real 3-D V_S model, trying to check the effective availability of the results which will be discussed in the following section. This test presents a Q_S^{-1} model created using anomalies comparable in size to those observed using the real data-set (W-E and S-N sections in Figure 3.12, panel a) but with slightly different geometries. A 10% normally distributed error was applied to the spectral ratios. The test shows that the anomalies are generally well recovered

Block#	1	2	3	4	5	6	7	8
$[(Q^{300})^{-1}] \times 10^{-2}$	$5,61$	$1,78$	$1,91$	$0,39$	$1,44$	0	$2,26$	0
$[(Q^{300})^{-1}] \times 10^{-2}, (Q_{T\min})^{-1}, (Q^{1800}_{b\min})^{-1}, (Q^{900}_{b\min})^{-1}$	$2,59$	$1,76$	$1,34$	$0,05$	$1,29$	0	$2,60$	0
$[(Q^{300})^{-1}] \times 10^{-2}, (Q_{T\max})^{-1}, (Q^{1800}_{b\max})^{-1}, (Q^{900}_{b\min})^{-1}$	$6,91$	$1,99$	$2,01$	$1,59$	$1,32$	0	$1,34$	0

Table 3.12: Stability Test - 300 m: the value of the inverse quality factor of each resolved block is dependent on both the maximum (0.026) and minimum (0.008) average inverse quality factor allowed. It is also dependent on and the maximum (0.0188, for 1800 m, and 0.0177, for 900m) and minimum (0.0167, for 1800 m, and 0.0151, for 900m) inverse quality factor of the blocks in which they are contained.

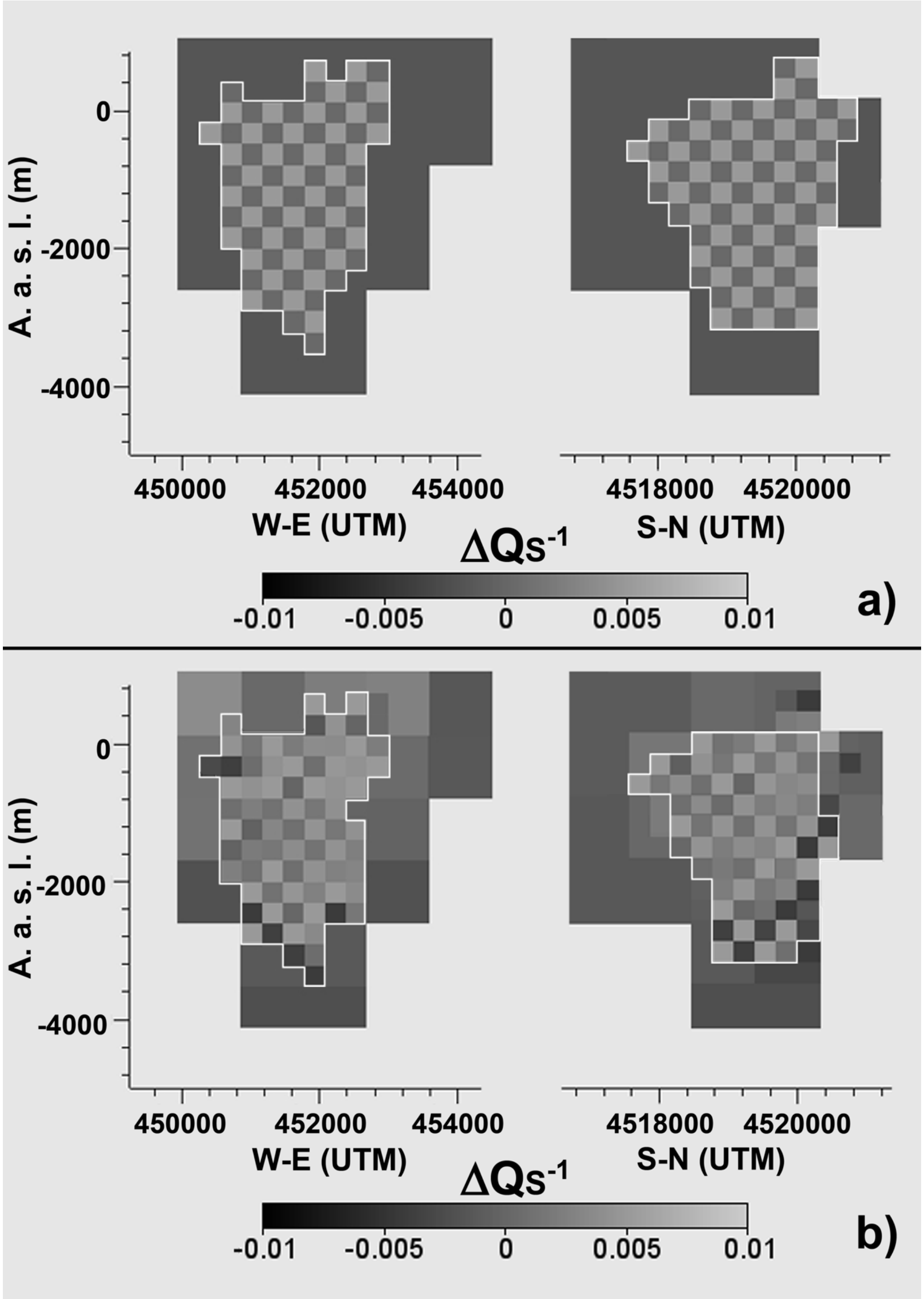

Figure 3.10: Checkerboard test in the HRR. a) Input: W-E and S-N sections (also marked in figure 1, lower right panel); the white lines include all the maximum resolution cells defined by formula (3.1). In this volume we assumed a checkerboard structure, with high Q-contrast among the blocks; a uniform attenuation medium is assumed outside HRR. b) Output: test results for a 10% error on synthetic data. The zones marked by the white broken lines include the cells where the checkerboard structure is effectively reproduced. ΔQ_S^{-1} grey scales represent the variation from the average quality factor.

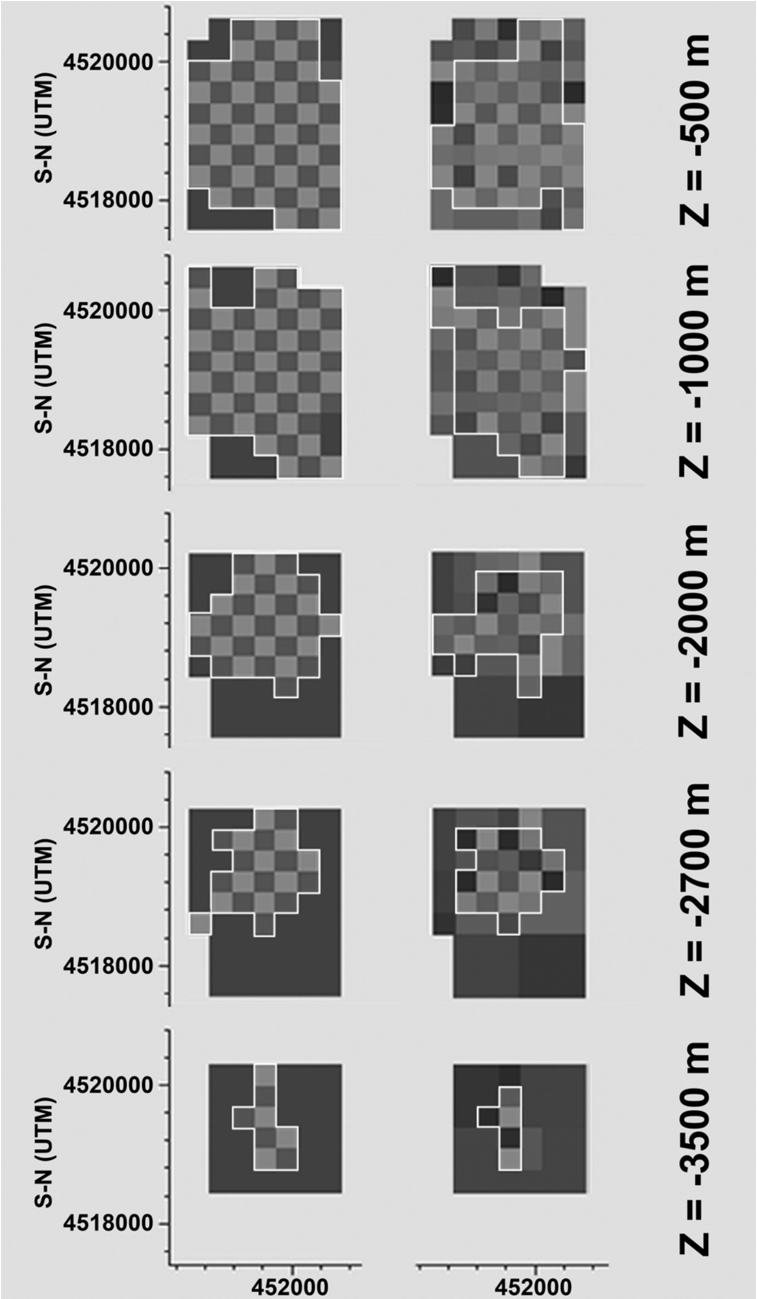

Figure 3.11: Left hand panels. Five horizontal slices at different depths (Z value respect to the sea level) of the volume containing the HRR. The white lines include all the maximum resolution cells defined by formula (3.1). The sections represent the input checkerboard structure also described in Figure (3.10), with the same colorscale. Rigth hand panels. The figures represent the test output; the zones marked by the white broken lines include the cells where the checkerboard structure is effectively reproduced.

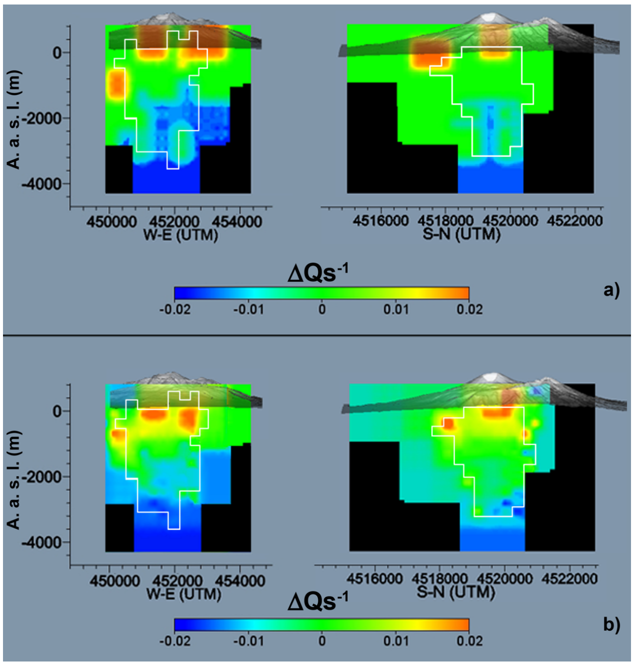

Figure 3.12: Synthetic anomaly test. The input structures (panel a) are included in a volume characterized by uniform attenuation. The output (panel b) show the reconstruction of the anomalies. Black areas are not resolved in the inversion. Colorscales refer to the variations respect to the mean inverse quality factor. The zones marked by the white broken lines include the cells where the checkerboard structure is effectively reproduced.

between the surface and -3000 m (W-E and S-N sections in Figure 3.12,b), even if their dimensions are comparable with the maximum resolution achievable. In the depth range between -3000 m and -4500 m the reproduction of Q_S^{-1} anomalies of the order of maximum resolution is more difficult; that results are consistent with the ones of the checkerboard test (Figure 3.11, $Z = -3500$ m); however, this region may be imaged at a resolution of 900 m, thanks to the new dataset.

3.3.6 Results

Using the present multi-resolution method, the attenuation structure under Mt. Vesuvius is obtained in two frequency bands (Table 3.6), centered at 12 and 18 Hz respectively. The images have a resolution of 300 meters in the sub-volumes with a higher ray coverage marked in Figures 3.10 and Figure 3.11 with a white broken line. All the results obtained are shown in Figures 3.13, 3.14 and 3.15. All the depths (negative downward), are calculated respect to the sea level. In Figures 3.14 and 3.15, the images relative to the velocity tomography (Scarpa et al. 2002) are also shown. The present database is a subset of the database used in the velocity tomography.

In Figure 3.13 the results of S-wave attenuation imaging, obtained with both CN and SD, are reported for sake of comparison. Using the CN technique, an estimate of the variation of the S-wave inverse total-Q respect to their mean was obtained for the two frequency bands (12 and 18 Hz), where the signal to noise ratio value resulted sufficiently high for this analysis (see also section 3.2.4). These images are reproduced in panels a and b of Figure 3.13. Using the SD technique, a unique image at 18 Hz was obtained (panel c).

Figures shown in panels a and b are very similar, except for an higher attenuation zone (turquoise) located in a depth range between -2500 and -3500 m centered at 452000 onto the W-E section, visible in panel b. Comparing panel b and panel c, it is evident that the images are similar in the HRR. Outside the HRR slight differences between the two images appear in the W-E section, at a depth of 1000 m, between coordinates 453000 and 454000. In this region the CN method (panel b) gives a high attenuation contrast zone, whereas the contrary occurs for SD method (panel c). The SD method produces in general a less uniform image respect to the CN method.

Figure 3.14, panel a, reports the W-E and S-N sections of the S-wave attenuation images at 18 Hz (hereafter only the S-wave attenuation images obtained with the CN method will be considered); in the same figure, the S-wave velocity (panel b), P-wave attenuation (panel c) and P-wave velocity (panel d) for the W-E and S-N sections are also represented. V_P/V_S ratio as a function of depth (calculated as an average over the slices at different depths) is superimposed to all the figures. The color scale in panels a) and c) represents the variation of the inverse quality factor respect to the mean S- or P-wave attenuation; the color scale of panels b) and d) represents the absolute S- and P-wave velocity.

Figure 3.15 represents five image slices at the depths -500, -1000, -2000, -2700 and -3500 meters. Color scales represent the differences respect to the average S-wave velocity (first column), S-wave attenuation (second column), P-wave velocity (third column) and P-wave attenuation (fourth column) calculated

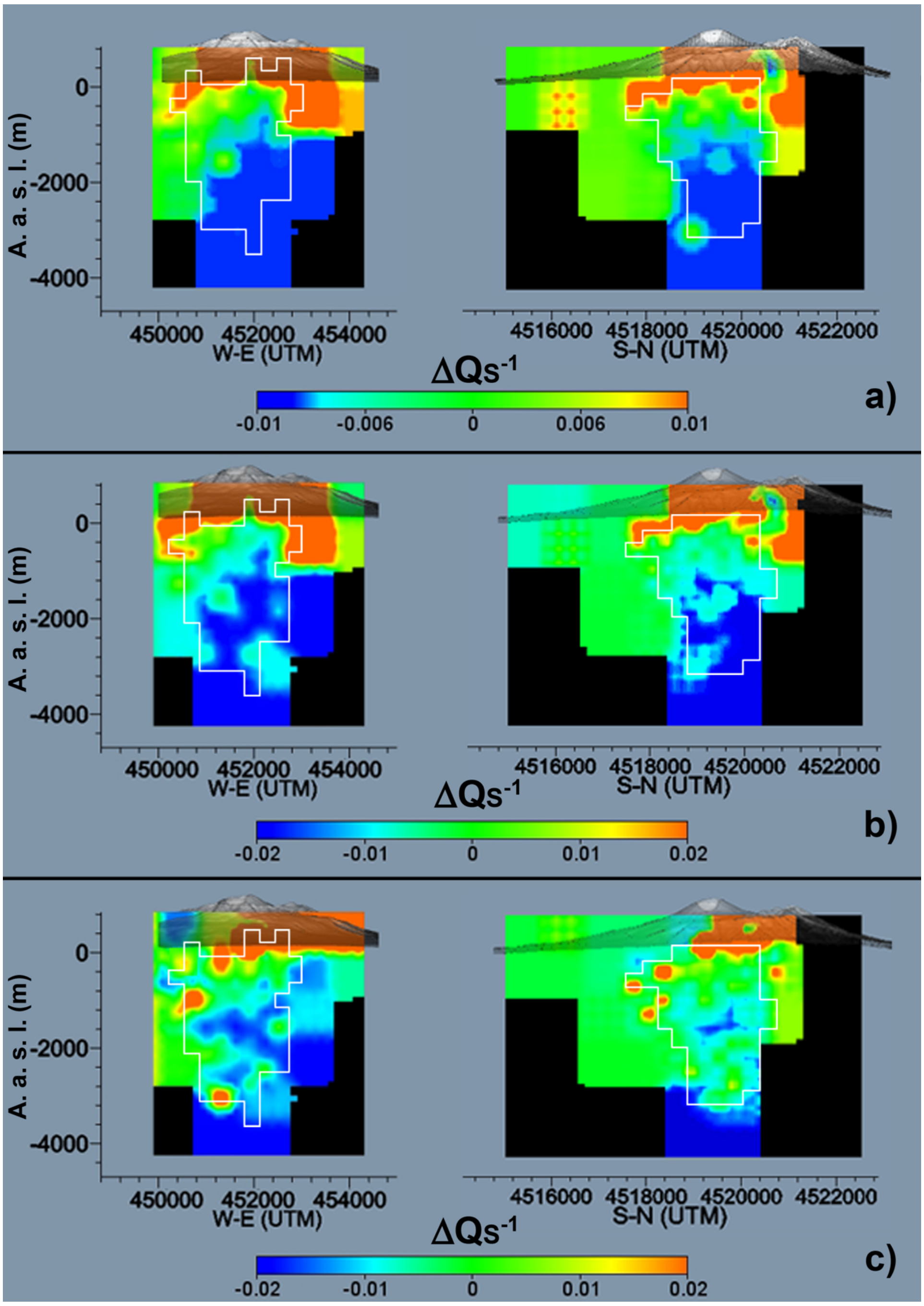

Figure 3.13: Results of the attenuation tomography inversion, in the frequency band centered at 12 Hz (panel a), and 18 Hz (panel b) for the CN method, compared with the results obtained at 18 Hz for the SD method (panel c). W-E and S-N sections are those marked in Figure (3.8, down-rigth panel). Black areas are not resolved in the inversion.Colorscales refer to the variations respect to the mean inverse quality factor. The zones marked by the white broken lines include the cells where the checkerboard structure is effectively reproduced.

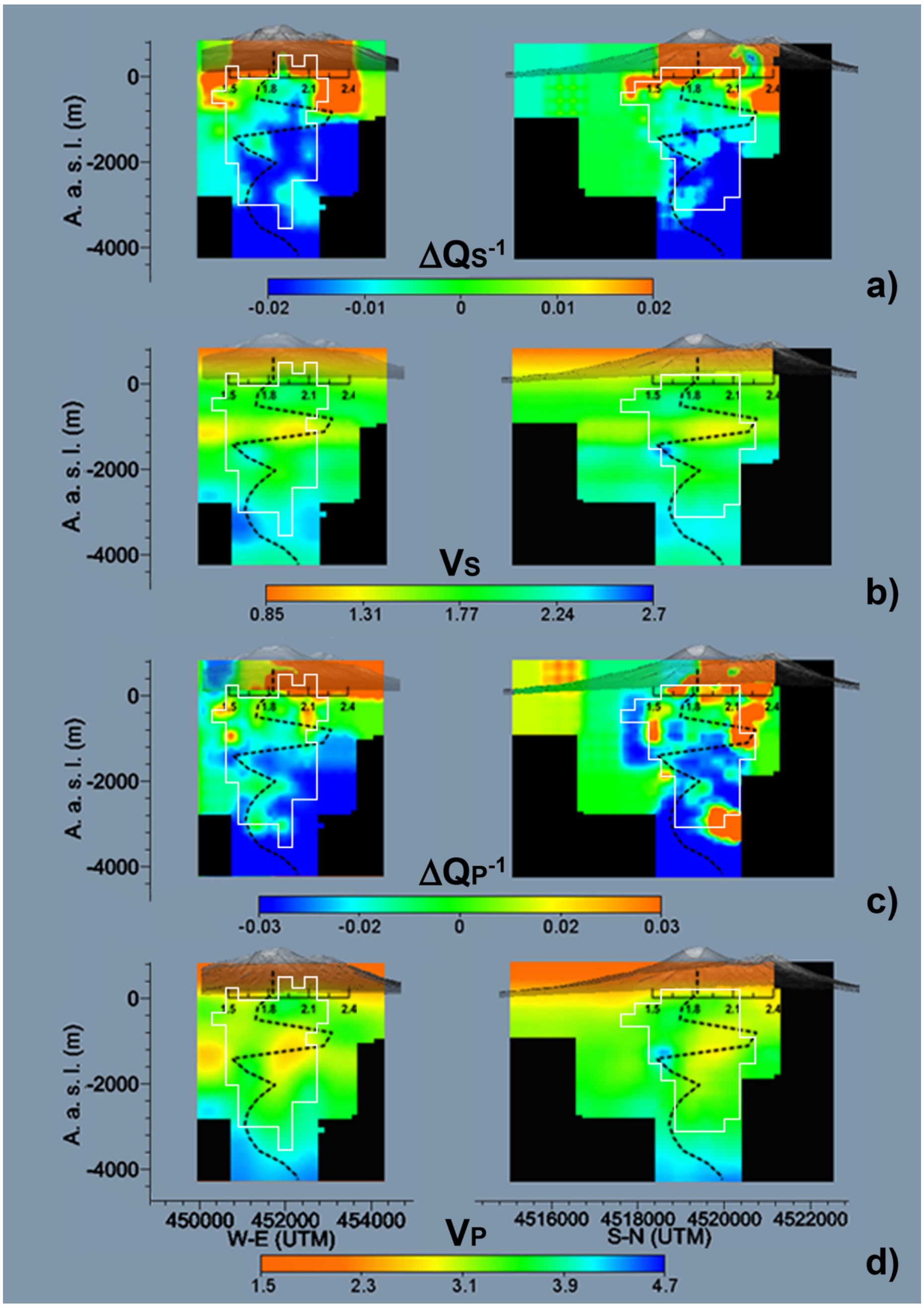

Figure 3.14: The W-E and S-N sections represent the attenuation structure inferred for S-waves (CN method), in the frequency band centered at 18 Hz (panel a), and the S-velocity structures inferred by Scarpa et al. (2002) (panel b). The dashed line represents the V_P/V_S pattern with depth and is overimposed to all Figures. The P-wave attenuation (SD method, 18 Hz) and velocity (inferred by Scarpa et al. (2002)) are also represented in panels c and d. The colorscales in panels a and c refer to the variations respect to the mean inverse quality factor obtained in the inversions for S- and P-waves. The colorscales in panels b and d represent the absolute S- and P-wave velocity. Black areas are not resolved in the inversion. The zones marked by the white broken lines include the cells where the checkerboard structure is effectively reproduced.

for each slice. This quantities follow the behavior of the absolute P- and S-wave velocities and attenuations (in the discussion any difference between the absolute quantity and the variation respect to the mean will be made), but they highlight more properly the lateral variations of this quantities.

3.3.7 Discussion

The HRR is localized essentially under the central part of the cone, till to a depth of 3.5 km (see Figures 3.10 and 3.11). Thus, in this zone, the S-wave attenuation image has a better resolution respect to that obtained using a single scale approach. Laterally, the resolution becomes lower due to the station density, which is not comparable with the cell dimension [for a wider discussion on station density and resolution see also Bai and Greenhalgh].

Frequency dependence of the S-wave attenuation

The results described in section 3.2.4 were confirmed; the results obtained using the present multi scale approach show better resolved images. In general, the 3-D attenuation pattern shows a Q which clearly increases with depth in the 12 and 18 Hz frequency bands (Figure 3.13, panels a and b), showing clearly visible attenuation contrasts localized along the borders of already known structures (see e.g. Scarpa et al. (2002)) like the carbonate basement, well visible at the maximum resolution in the Q_S^{-1}, Q_P^{-1}, V_S and V_p images at -1500 meters (see Figure 3.14, all panels). In the HRR, the independence of attenuation from frequency is confirmed in the frequency range between 12 and 18 Hz. Looking carefully at the a and b panels of Figure 3.13, it is noteworthy the relative contrast localized approximately east of the central cone between -2500 and -3000 meters. The synthetic test shown in Figure 3.12 clearly represents the damping of low variation in δQ^{-1}at the maximum resolution in this depth range, but the anomaly has clearly a size bigger than 300 meters. This contrast is not evident in panel b, for the 12 Hz image, and this is possibly due to the different linear dimensions of the anomalous region sampled by the different wavelengths.

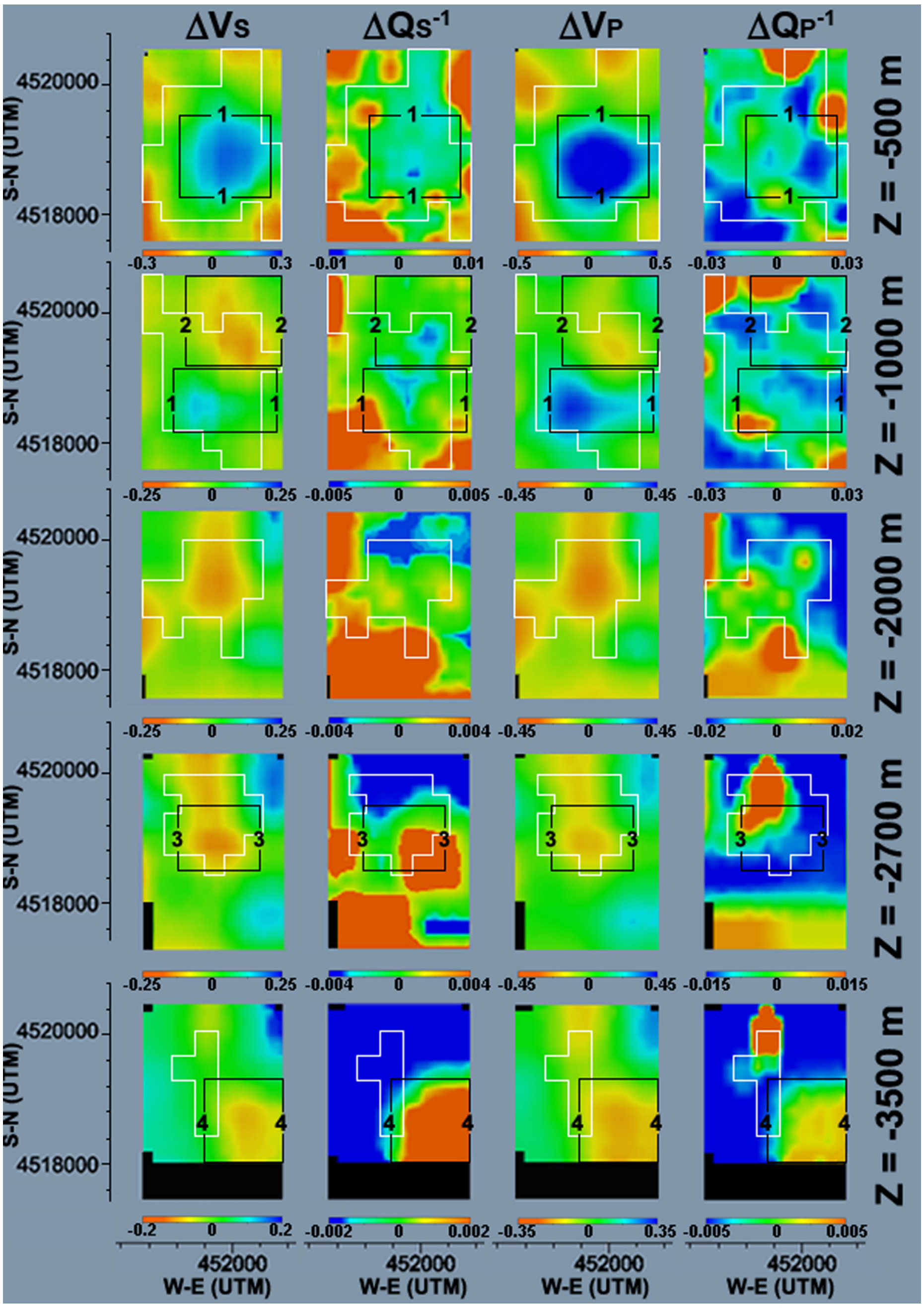

Figure 3.15: Five horizontal slices of the the volume containing HRR at different depths (Z). The colorscales for S- (first column) and P-wave (third column) attenuation images represent the variations from the mean inverse quality factor calculated on each horizontal slice at each depth. The colorscales represented in the second and fourth coloumns represent the variations of S- and P-wave velocity from the average velocity calculated at each depth, respectively. On each image we marked with numbered black rectangles, the zones characterized by important properties, widely discussed in the text. The zones marked by the white broken lines include the cells where the checkerboard structure is effectively reproduced.

Comparison between CN and SD images

The results obtained with the SD method add new information about the volcano structure at small scale. Moreover, SD method allowed to obtain a P-wave attenuation structure (in the band centered at 18 Hz) to be compared with that obtained for S-waves. Under the cone, the S-wave images obtained at 18 Hz with CN and SD method, respectively, are similar, clearly showing the same dependency of δQ^{-1} with depth (Figures multives6, panels b and c). In general the CN images appear much more smoothed than the SD ones. In the HRR most of the attenuation contrasts follow the same pattern , being sometimes different in value. The sole significant differences between CN and SD images can be observed between the depths of 1000 and 2000 m, in the N-E quadrant (corresponding at surface with the geological structure of Mt. Somma). In this volume (Figure 3.13, panels b and c) the interface between carbonate basement and the overlying volcano materials is not clearly defined in the SD image. On the other hand, this interface is clearly evidenced by SD method applied to P-waves, and very well defined by the velocity tomography (Scarpa et al. 2002, Zollo et al. 2002). The discrepancy above discussed may be due to the presence of a non-uniform scattering wave field (Wegler, 2003) that may produce a bias in the normalization of S-spectrum with coda spectrum. Despite this problem, the independence of CN of site transfer function makes CN approach particularly suitable for the application to volcanic areas, where site effects may severely affect the spectrum of S-radiation emitted by the VT earthquakes.

3.3.8 Joint interpretation of velocity and attenuation images

General pattern

The velocity images were first analyzed, isolating the volumes characterized by strong laterally and/or in depth contrasts, velocity inversions, variations from the average V_P/V_S. Then, they were associated with the corresponding volumes in all the other available images. Comparing V_P with Q_P^{-1} and V_S with Q_S^{-1} images (Figure 3.14, all panels), in general, high V_P zones clearly correspond to low Q_P^{-1}

volumes, and high V_S zones correspond to low Q_S^{-1} volumes; the unique evident exception is the volume located under the central cone,confined in the depth range between -1000 m and -2000 m, where the pattern is characterized by a low V_S and V_P corresponding to high variation in attenuation (Q_S^{-1} and Q_P^{-1} strongly increase with depth).

The shallower structures

On average, the attenuation of the S- and P-waves increases toward North and East in all the images for the volumes above the sea level (Figure 3.14, panels a and c); interestingly, the S-N section of the Q_S^{-1} image (panel a) shows a low attenuation inclusion (green surrounded by orange, not included in the HRR) of the order of a 900 meters block, corresponding with the structure of Mt. Somma. This mountain surrounds the central cone in the North and East quadrants (Figure 3.8, down left) and is characterized by higher rigidity older age lavas.

In the HRR (marked with a broken white line in Figure 3.10, panel b), velocity and attenuation images clearly evidence the presence of a contrast between the volcanic structure and the volume underneath at 0 meters; this contrast marks the first interaction between the recent products of the volcano activity and the older higher rigidity materials.

In Figure 3.15 ($Z = -500$ meters) it is evident that a low attenuation zone [roughly surrounded by the rectangle **1**] is strongly correlated with an high V_S and V_p zone in the same position. This area is located inside the HRR (see Figure 3.11, panel a) and may represent the residual lava emitted during the last eruptions, completely solidified in the present time. In the same slice (Figure 3.15, $Z = -500$) the western part is characterized by low Q_S^{-1}, high Q_P^{-1} and low V_P/V_S . This features, in particular the opposite pattern of Q_S^{-1} and Q_P^{-1} , may be compatible with the presence of a CO_2 reservoir (Hansen et al. 2004). This interpretation is corroborated by the presence of the above discussed low attenuating body in the central part of the figure. As reported by (Hansen et al. 2004), when the magma rises, the decrease in confining pressure causes the magma to decompress, and the biggest part of CO_2 exolves; however, when the magma cools, a modest amount of CO_2 can be definitely trapped in the rock matrix, and could explain the observed low V_P and low V_P/V_S anomalies. This interpretation is confirmed by the laboratory experiments of (Ito et al., 1979, Spencer, 1979, Sengupta and Rendleman, 1989). Summarizing the results from these papers, at pressure below the saturation pressure (as should be at a depth of -500 meters), the presence of gas can lead to a decrease in V_S and V_P, an increase of Q_S^{-1}, and an anomalous decrease of Q_P^{-1}, the same results obtained in our work. The presence of melt or partially melt rocks would lead to a low V_P, a low V_S, high V_P/V_S ratio, high Q_P^{-1} and high Q_S^{-1}. In the depth range around -500 m there is consequently no evidence supporting the presence of patches of magma with dimensions larger than cell size.

The intermediate structure

In the slices of Figure 3.15 ($Z = -1000$), a zone of strong lateral contrast is evident in both the V_P and V_S images [the zone surrounded by the white line marked by number **2**]. In this same zone there is no correspondence of the increasing velocity with decreasing attenuation, as already discussed in section 3.3.8. The low attenuation area marked by the white rectangle **1** in Figure 3.15 ($Z = -1000$ m) corresponds instead to an high velocity area. This area is a section of the anomalously high-velocity volume (Figure 3.14, panels b and d), which seems to intrude from depth, in agreement with the interpretation reported in several velocity tomography studies (Scarpa et al. 2002, Zollo et al. 2002, Tondi and Franco, 2003, De Natale et al., 2006), and interpreted as related to the residual part of solidified lava from the last eruption. This high attenuation and velocity area is linked to the area marked by line **1** in Figure 3.15, $Z = -500$ m.

To refine the interpretation in the depth range around -1000 m, especially for the area marked by rectangle **2** in Figure 3.15, the attention is focused on the W-E and S-N sections in Figure 3.14 [all panels]. The zone corresponding in depth with the maximum value of the V_P/V_S ratio roughly corresponds to the interface between high attenuation and low attenuation. This interface is also characterized by low V_P and low V_S. All these observations may be interpreted as due to the presence of a fractured medium permeated by fluids, as discussed in (Hansen et al. 2004) and (Eberhart-Phillips et al. 2005). This interpretation should exclude the presence of a shallow patch of magma in this depth range, in the limit of our spatial resolution: in fact, our attenuation images do not show any particular evidence of melt, that, if present, should have produced both high Q_P^{-1} and high Q_S^{-1}. This results are in agreement with previous interpretation of the velocity tomography done by Scarpa et al. (2002), and also corroborated by geochemical studies, that recognized the location of an hot aquifer under the cone located and modeled just in the same position, until a depth of -2200 m (Marianelli99 et al., 1999, Chiodini et al., 2001). The properties observed at $Z = -1000$ m can be observed also at $Z = -2000$ m (see Figure 3.15). In particular a secondary maximum in V_P/V_S ratio can be observed at -2000 m. The vertical sections of Qp-1 and Qs-1 (Figure 3.14 panels a and c) indicate the presence of lower attenuation zones around -2000 m, included in a low attenuation body. This pattern can be interpreted as an highly cracked medium filled by fluids, as also evidenced by geochemical studies (Chiodini et al. 2001).

The deepest structure

The V_P ,V_S and V_P/V_S patterns between -2500 m and -4000 m (Figure 3.14, panels b and d) are more regular. The $Z = -2700$ and $Z = -3500$ slices of Figure 3.15 help in better understanding the velocity and attenuation features. The pattern of Q_P^{-1} and Q_S^{-1} results similar at $Z = -2700$ (Figure 3.15), both in the HRR and in the LRR (see Figure 3.11 at the same depths). Focusing our attention on the central part of the attenuation images (rectangle **3**), high contrast in both Q_S^{-1} and Q_P^{-1} can be observed, not perfectly matching the contrast in both V_P and V_S. Looking at the resolution map on this slice (Figure 3.11, $Z = -2700$ m) this is not due to the lack of information achievable at the maximum resolution, but more probably to the lack of the maximum resolution in the area.

At $Z = -3500$ m, the decreasing attenuation corresponds to the increasing velocity outside rectangle **4**, for both P and S waves. A low velocity and attenuation zone corresponding to the South-East sector of Figure 3.15 at $Z = -3500$ m is clearly visible, and marked with the rectangle **4**. In this region the low V_P/V_S ratio excludes the presence of partially melt rocks or fluid inclusions, suggesting, on the contrary, the presence of a cracked volume. This zone is spatially coincident with the zone of maximum seismic energy release, as shown in Figure 3.8 (upper-left and upper-right panels, the grey ellipsoidal line marked by number **3**).

3.4 Campi Flegrei

The Campi Flegrei volcanic area is located inside the Campanian Plain, west of the city of Naples, where a marked lithospheric thinning is seen (Wang et al., 1989). The graben-like structure of the caldera is assumed to be mostly due to the collapse following the Campanian Ignimbritic eruption (about 35000 years ago) and its second period of activity (14000-10500 years ago), when Neapolitan yellow tuff covered a large part of the area (Scandone et al., 1991, Orsi et al., 1996). A third period of strong activity produced an uplift of the northern sector of the Gulf of Pozzuoli, which was probably due to shallow magma injection. There were successive eruptions until the one that resulted in the formation of Mt. Nuovo (Di Vito et al., 1987), which occurred near the local geomorphological discontinuity that is commonly known as "La Starza" (Di Vito et al., 1999), as shown in Figure 3.16,d.

The present activity is strongly dominated by slow vertical uplift (see Battaglia et al. (2006), and references therein), with three main episodes recognized in the last 40 years. The first two of these were between 1950 and the early 1970 s, and the second produced a maximum vertical displacement of 1.7 m that was associated with the seismic activity (Corrado et al., 1976). The third episode occurred in 1982-1984, with a maximum uplift of 1.6 m (Berrino et al., 1984), and was accompanied by strong seismicity. During this last period, the University of Wisconsin deployed a temporary network of portable digital seismic recorders in the proximity of the Campi Flegrei caldera, equipped with three-component, short-period sensors. Using the data recorded in 1984 from mid-March to mid-April, i. e. during the highest seismicity rate ever recorded in the area, a first velocity structure of Campi Flegrei was obtained by Aster and Meyer (1988). Later, the velocity structure was refined by adding more data in their inversion (Aster et al., 1989, Pujol and Aster, 1990). The velocity structure of Campi Flegrei has also been improved more recently on the basis of active data (Zollo et al., 2003, Vanorio et al., 2005, Battaglia et al., 2008). These studies did not show

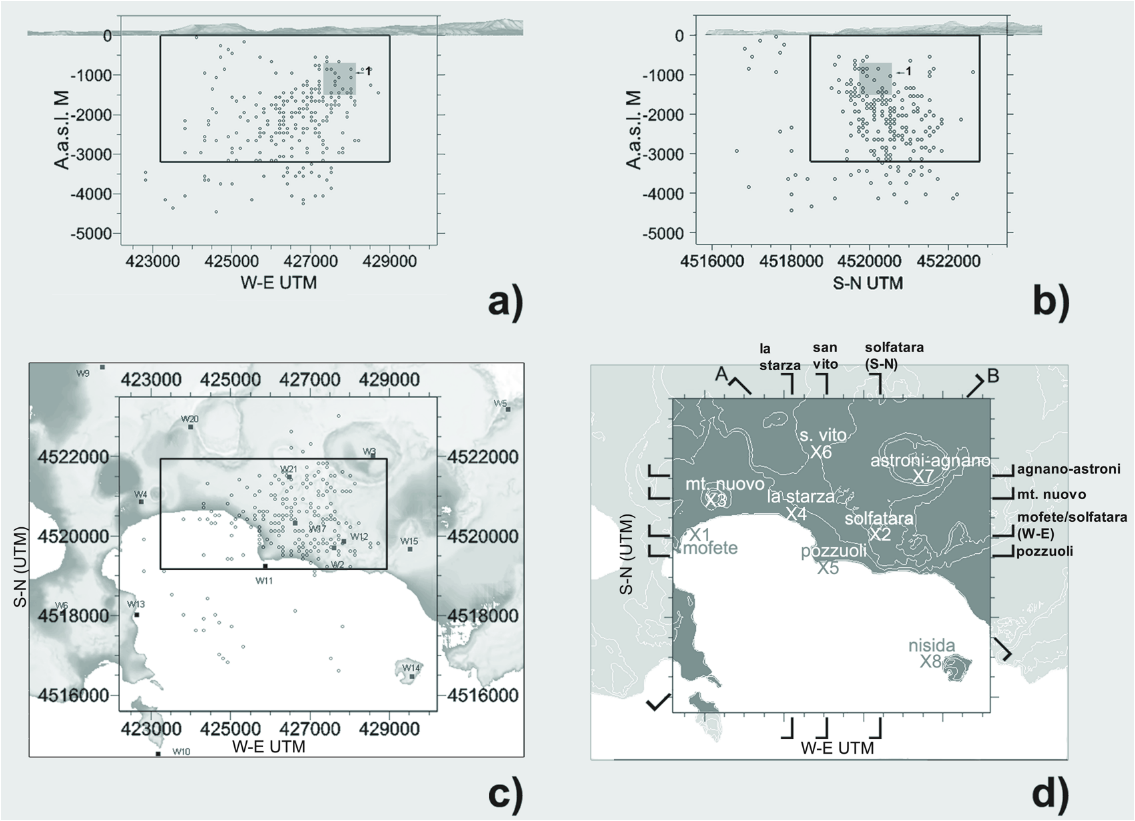

Figure 3.16: **a** and **b**: W-E and S-N sections of the seismicity pattern at Campi Flegrei. The grey square marked with **1** represents the zone for which the results of the robustness and stability tests for the maximum resolution (500 m) were performed. **c**: Map of Campi Flegrei with the station positions (black squares) and hypocentral locations (circles) of the seismic events indicated. **d**: Map of Campi Flegrei with the area investigated in the present study highlighted. The names and the capital letters at the upper and eastern sides of the area analyzed define the spatial locations of the vertical sections for which the tomographic images in Figures 3.19, 3.20, 3.21, 3.22 and 3.23 are shown.

clear evidence of extensive melting zones between 0 and 5500 m below sea level; however, magma intrusions and the migration of fluids with an increase in pressure into a hydrothermal reservoir have been considered as an adequate source for the strong ground deformations that have occurred in the area (Bonafede and Mazzanti, 1998, Gaeta et al., 1998, Gotsman et al., 2006). Recently, Battaglia et al. (2006) excluded the intrusion of magma, indicating the migration of fluid to and from the caldera hydrothermal system as the cause of the ground deformation and consequent unrest.

In 1999, a research project sponsored by the Italian Civil Defence aimed to develop advanced techniques based on active and passive data, to obtain a detailed model of the Campi Flegrei region. The data collected during the $1982 - 1984$ seismic crisis were thus combined with data obtained by a high resolution offshore reflection survey (the SERAPIS Project) that took place in 2001 into the Gulf of Pozzuoli. This combined approach greatly improved the quality of the images and their interpretation. For an extensive review of these results, see Zollo et al. (2006). Here, it is is reported a brief summary, that combines the data of the SERAPIS project with the data from previous investigations.

- Geothermal drilling has shown high temperature gradients in all of this area ($150°C\ km^{-1}$), and the presence of two distinct aquifers ($150 - 300$ m and $1250 - 1600$ m in depth) in the Agnano area.

- Magneto-telluric surveys have shown a low resistivity zone, 4000 m under the town of Pozzuoli.

- V_P/V_S ratio tomography has been interpreted using the experimental measurements of rock physical properties on Campi Flegrei samples as a constraint, and shows the presence of fluids under the city of Pozzuoli, at the depth of 1000 m. The low V_P/V_S ratio value at 4000 m in depth is not consistent with the presence of magma or fluids (see Vanorio et al. (2005) for a complete discussion).

- The attenuation of P-waves (De Lorenzo et al. 2001b) has shown important features, such as the high Q_P^{-1} anomaly between 2000 and 3000 m in the central-eastern part of the caldera, in the zone of Agnano-Solfatara.

These data, together with the S-velocity tomography described by Zollo et al. (2006), will be compared with the present data.

- Seismic reflection experiments (Zollo et al., 2008) have revealed an extended fluid-bearing rock formation at about 3000 m in depth. A 7500 m deep, 1000 m thick low velocity layer was also revealed, which has been interpreted as associated with a mid-crust, partial melting zone beneath the caldera, suggesting that a large magmatic sill is present well within the basement formation.

3.5 The estimate of the average Q frequency dependence at Campi Flegrei

The recalibration of the magnitude scales at Campi Flegrei on the basis of measured path, site and transfer functions (which yelded to the paper by Petrosino et al. (2008)), fournished the estimate the average total quality factor in the center of the Campi Flegrei caldera, namely the Solfatara area. The ordinary slope decay method has been used, taking into account the source and site terms, and measuring the spectral slope in a given frequency band, centered at f_C^1. This method has been described in section 2.3.2, and will be used to obtain the single path P-wave attenuation of the Campi Flegrei area. With this method, the data vector in the frequency band centered at f_C^1, $d_k^S(f_C^1)$, can be obtained using external data to remove the source, site and instrumental terms. Using an average slowness, s, and measuring the ray lengths, l_k, the single parameter inversion scheme:

$$d_k^S(f_C^1) = l_k s Q_T^{-1}(f_C^1) \tag{3.3}$$

can be written. $Q_T^{-1}(f_C^1)$ is the average total quality factor in the frequency band, and the problem may be solved with classical inversion techniques.

The frequency band may now be shifted to the one centered at f_C^2, obtaining the average quality factor in this frequency band, $Q_T(f_C^2)$. If the signal-to-noise ratio allows to obtain a sufficient number of Q_T at differen frequencies, the classical frequency dependence for Q_T (Aki and Richards, 1980, Sato and Fehler, 1998) may

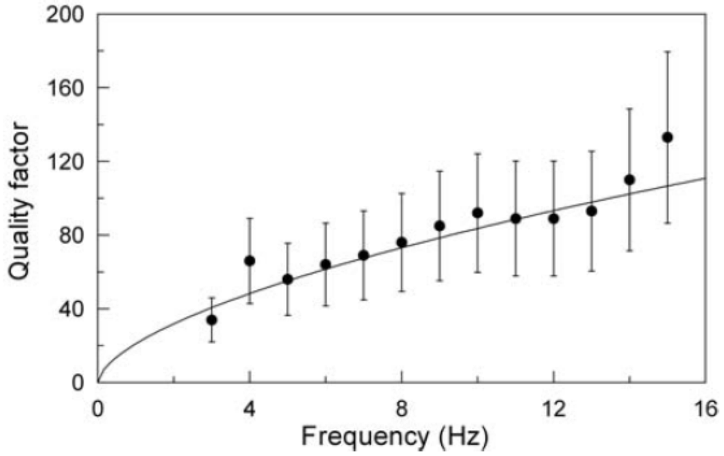

Figure 3.17: Quality factor (Q) values obtained from the attenuation analysis in the 3–15 Hz frequency range (circles), and the functional dependence on the frequency described by the law $Q(f) = 21f^{0.6}$ (solid line).

be assumed:

$$Q(f_C) = Q_0 f_C^y, \tag{3.4}$$

and a new linear inversion scheme may be defined, taking the logarithm of the quality factors:

$$\log Q(f_C^j) = \log(Q_0) + y \log(f_C^j). \tag{3.5}$$

where j refers to the $j-$th frequency band. Both a least square and a non-negative least square inversion code have been applied to find a solution of these inversion scheme (3.3) in Campi Flegrei area, without finding any particular difference. Thus, the least square algorithm, which allowed to calculate the covariance of the parameters whitout using any algorithm for calibration and adjustment of the covariance (Malick, 2005, Boyd and Xiao, 2005), has been applied. The error on the model parameter of formula (3.3) are dependent on the covariance matrix of formula (3.3). Just using the data obtained at Solfatara, the solution of the inversion scheme of formula (3.3) (Figure 3.17) is:

$$\begin{aligned} Q_0 &= 21 \pm 7 \qquad (3.6)\\ y &= 0.6 \pm 0.9. \end{aligned}$$

The results of the same inversion process obtained using the waveforms collected in the whole Campi Flegrei area are:

$$\begin{aligned} Q_0 &= 25 \pm 7 \\ y &= 0.6 \pm 0.9. \end{aligned} \tag{3.7}$$

3.6 Multi scale attenuation tomography

In this chapter, the results of the application of the tecniques developed and refined so far on the Mt. Vesuvius volcanic area to the Campi Flegrei caldera are presented. This section represents a wider description of the work which leaded to the article De Siena et al. (submitted to JGR).

Passive, high resolution attenuation tomography is used to image the geological structure in the first upper 5 km of the shallow crust beneath the Campi Flegrei caldera. Inversion was carried out using a two-step resolution method, which ensures a minimum cell size resolution of 500 m in the zones with sufficient ray coverage, and 1000 m outside these zones. Robustness, stability and checkerboard tests guarantee an optimal reproduction of the input synthetics in a wide area located in the centre of the Campi Flegrei caldera in a depth range from between the surface to about 3500 m. The attenuation images are compared with V_P, V_S and V_P/V_S images obtained by Battaglia et al. (2008), which show a general positive correlation between low (or high) velocity and low (or high) Q. High attenuation vertical structures extend between the surface and a depth of about 3000 m below sea level, where there is the hard rock layer. This is well revealed by the velocity tomography, and corresponds to a sharp contrast of the quality factor extended laterally beneath the whole area under study, to a depth of 3000 m below sea level. The vertically trending high attenuation structures are connected at the surface with the main volcanological features (Mt. Nuovo cone, erupted in 1531; the Solfatara fumarole field; the Astroni-Agnano complex; the Mofete fumarole field). The fault structure known as "La starza", where most of the recent seismicity has taken place, is well depicted by a sharp lateral change between low and high Q rocks, which extends in depth from 0 and 2000 m. The high attenuation zones corresponding to the area of maximum uplift recorded during the bradyseismic crisis of $1983 - 84$, and which are close to the town of Pozzuoli, extend towards the hard rock layer at 3000 m in depth. This zone appears densely fractured and is possibly connected with the deeper magma sill (at about 7000 m in depth) that was recently revealed by passive travel-time tomography. The interpretation based on evidence from geological, volcanological and geochemical investigations, indicates that the vertically extending, high attenuation structures correspond to gas reservoirs beneath Solfatara and San Vito, and to intense fluid circulation beneath Mofete, Mt. Nuovo and Astroni-Agnano.

3.6.1 Data, velocity model and ray-tracing.

Data

The present database is composed of 246 earthquakes that were recorded during the seismic crisis that occurred in Campi Flegrei from January to June 1984 at 15 three-component seismic stations (Table 3.13), sampled at 100 or 200 s.p.s. In all, 853 waveforms were selected (for each component) considering the best signal-to-noise ratios, the absence of spikes and other disturbances, a minimum coda duration (from origin time) of 15 s, and the absence of secondary events in the early coda. In making this selection the magnitude was implicitly restricted in the range from 1.8 to 3.0. The corner frequency, a critical parameter in the application of the ordinary slope decay method, was reestimated, calculating the intersection between the straight-lines fitting the logarithmic low frequency and high frequency spectrum, respectively. The error associated with this estimate is of the order of 25%.

Velocity model

Battaglia et al. (2008) obtained a velocity model of Campi Flegrei for P-waves and S-waves by merging passive and active datasets of travel-times, obtained during the 1984 seismic crisis and the 2001 SERAPIS experiment, respectively. Their methods used an improved finite-difference travel-time computation, jointly inverting the velocity model and the event locations. The results have confirmed the presence of an annular high P-wave velocity anomaly, which is possibly the signature of the

Station	E-W (UTM)	N-S (UTM)	altitude (a.s.l.) (m)
W02	427566	4519739	0
W03	428526	4522058	0
W04	422726	4520835	0
W05	431901	4523261	0
W06	420763	4518016	0
W09	421708	4524328	0
W10	423200	4514502	0
W11	425836	4519261	0
W12	427812	4519891	0
W13	422626	4518002	0
W14	429552	4516520	0
W15	429466	4519724	0
W17	426579	4520335	0
W20	423932	4522742	0
W21	426425	4521502	0

Table 3.13: The 15 three-component seismic stations for data collection in the present study at Campi Flegrei

buried rim of the caldera. The V_P/V_S model confirms the presence of a high V_P/V_S anomaly under the city of Pozzuoli, -1000 m above sea level, and of a low V_P/V_S body extending at about -4000 meters above sea level, below a large part of the caldera. In the present study,this model has been used as the basis for ray tracing and for localization, as well as for comparing velocity and attenuation images.

Ray-tracing

The selected events were relocated using the same non-linear localization algorithm used for Mt. Vesuvius (Lomax et al. 2001). The results confirm that most of the seismicity is located under the caldera, while a small number of the events are under the sea (Figure 3.16,c). The Thurber-modified numeric approach (section 2.2.1) was used to trace the path of each ray in the 3D velocity structure obtained by Battaglia et al. (2008). After dividing the whole structure to be investigated into two different grids (of 1000 m^3 and 500 m^3 cell sizes), the lengths of each ray, connecting each source to each receiver, and the lengths of the ray segments crossing each cell were calculated. These data are needed for application of the multiple-resolution inversion.

3.6.2 Estimate of the seismic attributes with the CN method.

The method has been fully described is chapter 2. Thus, here only formula (2.22) and formula (2.21) are reported:

$$\widetilde{d_k^C} = \frac{1}{2\pi f}\ln(\frac{1}{P(f,t_c)}) - d_k^C - Q_T^{-1}\sum_{b=1}^{N\_cells} l_{kb}s_b. \qquad (3.8)$$

$$\widetilde{d_k^C} = \sum_{b=1}^{N\_cells} l_{kb}s_b\delta Q_b^{-1} \qquad (3.9)$$

$P(f,t_c)$ has been measured experimentally for Campi Flegrei (Del Pezzo et al., 1996). The radiation pattern effects are smoothed by estimating $E_{ij}(f,r)$ in a time window containing the direct S-wave pulse plus the first 2 s of the early S-coda, which is formed by forward scattered S-wave radiation. The statistical change point test described by Mulargia and Tinti (1985) has been used to check experimentally that the radiation pattern effects are strongly reduced in the present data for a time window of 2 s. A detailed description of this test is included in section 3.3.2. So, the S-wave coda window time length is set at 2 s, starting from the S-wave onset, and the coda signal time window is set starting with a 16 s lapse time and ending at 18 s, since most of our data show a favourable signal-to-noise ratio (>3) for lapse time smaller than 20 s. A discrete Fourier transforms (DFT) is applied to the signals after windowing (a cosine taper window with tapering at 10% is used for both S and coda), for both the horizontal components of the ground motion. Then the spectra are smoothed, averaging in the frequency bands centred at the values of frequency f_c, with bandwidths ($\pm f$) reported in Table 3.14. Finally, the horizontal component spectra are log-averaged, and the ratio between the S-wave averaged spectrum and the averaged coda spectrum is calculated. The natural logarithm of this ratio estimates the quantity d_k^C of formula (3.8).

$-\Delta f$	$f_c(Hz)$	$+\Delta f$
4	6	8
10	15	20

Table 3.14: Frequency bands in which the results have been obtained

3.6.3 Estimate of the seismic attributes with the ordinary slope-decay method.

Direct P spectral amplitudes were calculated in the frequency bands centred at $f_c = 6\ Hz$ and $f_c = 15\ Hz$, with bandwidths ($\pm\Delta f$) (Table 3.14), using the inversion scheme described in section 2.3.2. A DFT is applied to a time window starting from the P-wave onset, and ending at 0.1 s before the S-wave picking, tapering each spectrum with a 10% cosine taper function. The spectra are log-averaged over the components, and the results obtained in the same area by De Natale et al. (1987) and Del Pezzo et al. (1993), who measured path-independent and path-dependent site-effects, are used in formula (2.35) to correct for these quantities. The derivatives of formula (2.35) are computed using the MATLAB "diffnew" routine.

3.6.4 Multi-resolution inversion

It is well known that the resolution of seismic imaging depends both on the wavelength (which should be smaller than the cell size) and the number of rays that sample the single cell (Bai and Greenhalgh, 2005). In the present dataset, a frequency of 6 Hz corresponds to a wavelength of about 250 m. Consequently, a minimum cell size of 500 m is assumed, to obtain robust results in the sub-volume in which the hypocentre distribution and ray coverage can be assumed to be uniform. Outside this sub-volume, a cell size of 1000 m is assumed. The same iterative inversion scheme as that used in section 3.3.4 is used, employing the results obtained at a lower resolution as input for the problem at higher resolution, as explained in section 2.4.2. The average quality factors for P- and S-waves used in the inversion scheme are reported in table 3.15. The seismic attributes are calculated (both for the CN method and the modified slope-decay method) as described in Appendix A.2.

Q_T^{-1}	$6Hz$	$15Hz$
$(Q_T^{-1})_S \pm \sigma_S$	0.013 ± 0.003	0.008 ± 0.002
$(Q_T^{-1})_P \pm \sigma_P$	0.005 ± 0.002	0.003 ± 0.001

Table 3.15: The average quality factor for S-waves and P- waves, obtained in the two frequency bands. Uncertainty is estimated assuming that each spectrum is affected by a 10 per cent of error due to noise, by the 25 of error relative error on corner frequency, and by the errors relative to each site.

Here, only the empirical master equation 2.44, used to evaluate the blocks effectively solved in the final inversion is written. These blocks are the ones crossed by a number of ray segments , n_R, given by:

$$n_R \geq \frac{4Block\_side}{\lambda}. \tag{3.10}$$

where λ is the wavelength at which the data were obtained. The coefficient $\Upsilon = 4$ was empirically set.

3.6.5 Robustness, stability and checkerboard test

a) Robustness and stability

Robustness and stability tests have been carried out for the results from the CN method at $f_C = 6$ Hz. A bootstrap approach, in analogy with the previous studies in Mt. Vesuvius volcano, has been used. The results for blocks with 1000 m and 500 m sides (the number of blocks is given by formula (3.10)) are obtained with a random reduction in the number of available formulas (rays). This reduction would reduce the number of rays with respect to the limit given by formula (3.10) from time to time; so the number of blocks solved by the inversion will be smaller at each reduction. So, the solution is forced at each data reduction for all of the blocks obtained in the inversion with the whole dataset. The quantity:

$$H = \left| \frac{Q_b^{-1}(0) - Q_b^{-1}(\%)}{Q_b^{-1}(0)} \right| \times 100, \tag{3.11}$$

represents the variation in the inverse quality factors for progressive reductions in the formulas used to solve the inverse problem. $Q_b^{-1}(\%)$ is the inverse quality

Block#	1	2	3	4	5
H^{1000}, 10%	0%	7%	3%	0%	2%
H^{1000}, 20%	16%	2%	0%	0%	0%
H^{1000}, 30%	19%	17%	25%	7%	5%
H^{1000}, 40%	33%	19%	17%	48%	0%
H^{1000}, 50%	40%	41%	41%	83%	50%

Table 3.16: Robustness test at 1000 m: H is a positive percentage; its value is an inverse measure of the robustness of the inversion at a resolution of 1000 m. The value of H is given by formula (3.11), and is represented for 5 blocks solved in the inversion. The increasing percentage in the first column is the data reduction.

factor of block b obtained for the reduced dataset, whereas $Q_b^{-1}(0)$ is the solution obtained using the whole database. H usually increases when reducing the number of formulas in the inversion problem, so its value is an inverse measure of the robustness of the inversion. The first step of the multi-resolution method images the attenuation structure of Campi Flegrei at a resolution of 1000 m. H was measured 100 times for this resolution, each time with a 10% random reduction in the formulas used to solve the inversion problem, obtaining an average H (over the 100 times). The same procedure was carried out for the other random reductions in the formulas (20%, 30%, 40%, 50%). In most of the cases, a significant increase in H is seen for a reduction of more then 40% of the dataset at 1000 meters. For the sake of the synthesis, Table 3.16 gives the results obtained for 5 blocks solved for each data reduction.

The same procedure was carried out for the last step of the multi-resolution inversion, which provides a 3D attenuation image at a resolution of 500 m. This second test shows a lower robustness: a significant change in the value of H (on average, more than 40%) is obtained for a random extraction of more than 30% of the data. In Table 3.17, the results for 8 blocks contained in a single 1000 meters side block are given. The position of the 1000 meters side block is shown in Figure 3.16,a, b, (labelled as **1**).

The stability of the method at a resolution of 1000 m is checked by substituting for the average inverse quality factor Q_{ST}^{-1} the extreme values of the interval $[(Q_{ST}^{\min})^{-1} = -3\sigma_S + Q_{ST}^{-1}, (Q_{ST}^{\max})^{-1} = +3\sigma_S + Q_{ST}^{-1}]$, where σ_S is the error on the Q_{ST}^{-1} values reported in Table 3.15. So, a new set of seismic attributes is calculated, based on a new initial parameter. For the 1000 m resolution, the changes in the

Block#	1	2	3	4	5	6	7	8
H^{500}, 10%	48%	19%	8%	27%	13%	79%	37%	4%
H^{500}, 20%	32%	5%	10%	40%	19%	$> 100\%$	$> 100\%$	12%
H^{500}, 30%	24%	4%	12%	31%	15%	$> 100\%$	$> 100\%$	60%
H^{500}, 40%	$> 100\%$	31%	5%	3%	70%	$> 100\%$	$> 100\%$	$> 100\%$

Table 3.17: Robustness test at 500 m: H is a positive percentage; its value is an inverse measure of the robustness of the inversion at a resolution of 500 m. The value of H is given by formula (3.11), and is represented for 8 blocks contained in a single 1000 meters side block of inverse quality factor 0.013, shown in Figure 3.16,a,b. The increasing percentage in the first column is the data reduction.

parameter model (Q_b^{1000}) are reported in Table 3.18 for a suite of 5 blocks.

For the solution in the inner volume (500 m), the results obtained by recalculating $(Q_b^{1000})^{-1}$ on the basis of the changed values of Q_T^{-1} are used. The changes of the inverse quality factors for the 8 blocks contained in the grey block marked by **1** in Figure 3.16,a,b are given in Table 3.19.

b) Checkerboard tests

An appraisal of the resolution is essential for a meaningful interpretation of seismic tomography images. The effective resolution of our method is tested by imposing an *a priori* attenuation structure to the area in a checkerboard test. First, some blocks of side 1000 meters sampled by an adequate number of rays are considered (given by formula (3.10)). Second, a checkerboard distribution of the inverse quality factors is assumed for these blocks (Figure 3.18,C1); the synthetic spectral ratios of formula (2.22) are generated and a Gaussian random error calculated

Block#	1	2	3	4	5
$[(Q^{1000})^{-1}] \times 10^{-2}, (Q_{ST}^{-1})$	$1,3$	$0,45$	$0,11$	$0,01$	$2,5$
$[(Q^{1000})^{-1}] \times 10^{-2}, (Q_{ST}^{\min})^{-1}$	$1,4$	$0,90$	$0,12$	$0,01$	$1,4$
$[(Q^{1000})^{-1}] \times 10^{-2}, (Q_{ST}^{\max})^{-1}$	$0,6$	$0,90$	$0,09$	$0,01$	$0,6$

Table 3.18: Stability test at the lowest resolution (1000 m); the value of the inverse quality factor of 5 blocks solved in the inversion. The value of the inverse quality factor for each block is obtained using the average S-waves quality factor (first row). Second and third rows report the values of the quality factors for the five block, obtained substituting in the multi-resolution inversion the inverse average quality factor with the minimum (0.001) and maximum (0.025) average inverse quality factor.

Block#	1	2	3	4	5	6	7	8
$[(Q^{500})^{-1}] \times 10^{-2}, (Q_{ST})^{-1}$	1,3	4,05	9,38	0,01	4,15	0,01	2,31	4,22
$[(Q^{500})^{-1}] \times 10^{-2}, (Q_{ST}^{\min})^{-1}$	1,14	3,94	9,98	0,01	4,51	0,01	2,05	4,79
$[(Q^{500})^{-1}] \times 10^{-2}, (Q_{ST}^{\max})^{-1}$	1,09	3,87	9,89	0,01	4,57	0,01	2,08	4,56

Table 3.19: Stability test at the highest resolution (500 m); the value of each inverse quality factor in the columns labelled by numbers from 1 to 8 refer to the blocks contained in the block labelled by number 1 in Figure 3.16,a,b. In the first row, the value of the inverse quality factor for each block is obtained using the average S-wave quality factor and the value of the inverse quality factor consequently obtained in the block labelled by number 1, where each of the blocks is contained (Q inverse is 0,013). The values of the inverse quality factors in the second and third rows are obtained using the minimum (0.001) and maximum (0.025) average inverse quality factor, respectively , as in the previous stability test.

with a random number generator with zero mean and 10% sigma is added to these values. Third, the inversion scheme for these synthetic data is solved using the CN method. The attenuation structure that comes out from the inversion (the output of the test where the maximum resolution is 1000 m is shown in Figures 3.20 and Figure 3.22, last rows, columns F, "la starza" and "pozzuoli") is similar to the synthetic input image, which is almost identical in the areas intensively populated by seismic events.

The cross-sections of the volume that can be effectively imaged at the maximum resolution are roughly shown in Figure 3.16,a-c, with a bold black line. A second test is performed, imposing a checkerboard distribution of the quality factors (Figure 3.18,C2) to the blocks of 500 m side always satisfying formula (3.10), and assuming the same error applied to the data of the previous test. In the Results section (Figures 3.20, 3.21, 3.22, 3.23, columns C, D, E, "mofete/solfatara", "solfatara", "mt. nuovo", "san vito", "astroni-agnano", last rows), the output of the test corresponding to the maximum resolution (1000 m or 500 m) available is reported on each cross-section.

The test confirms that the maximum resolution can be effectively obtained in the inner volume of Figure 3.16,a-c.

3.6.6 Results

The results are shown in the sections of Figure 3.19 and in the horizontal and vertical slices of Figure 3.20, 3.21, 3.22, 3.23; in these Figures, the unresolved

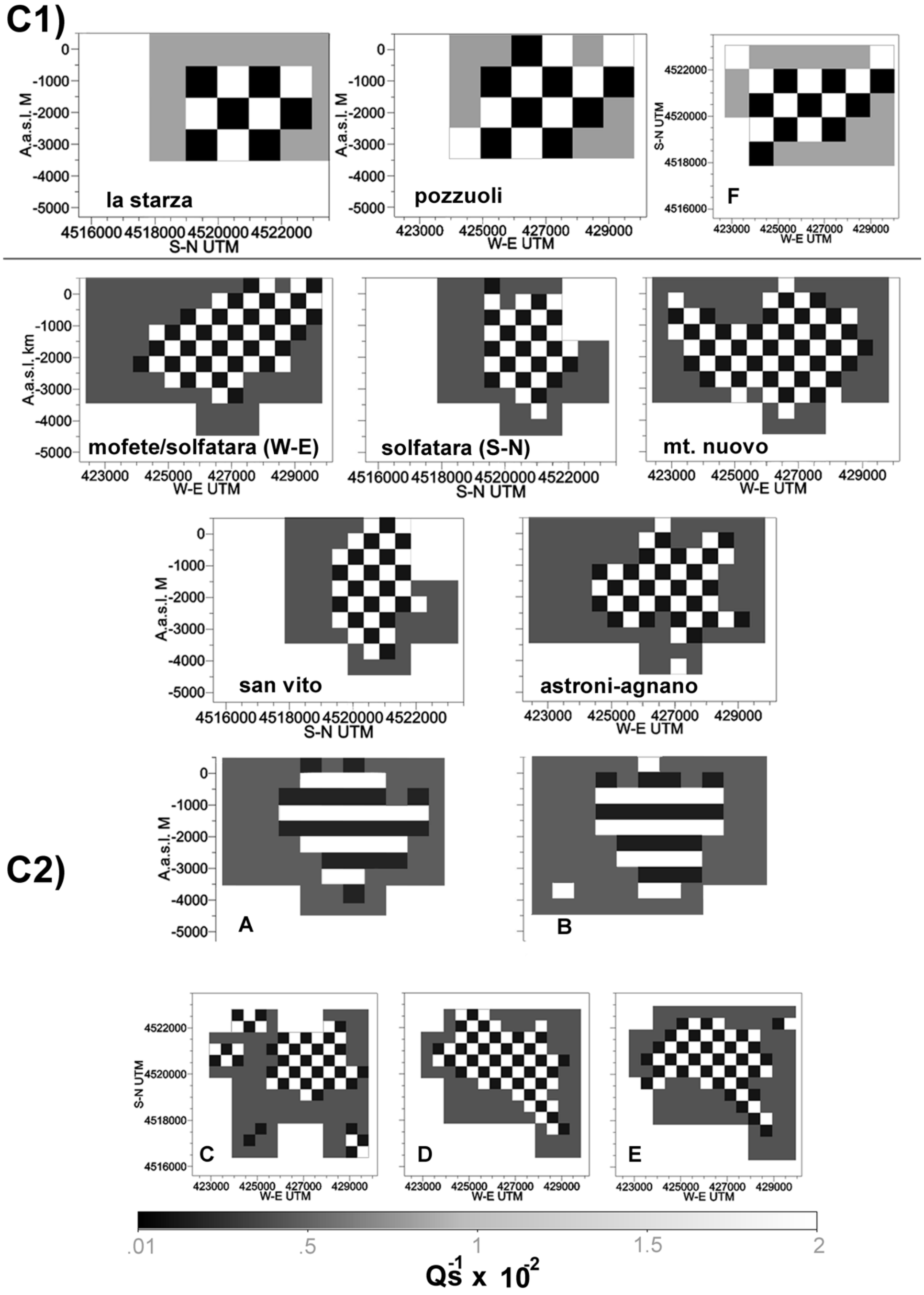

Figure 3.18: Input of the checkerboard tests performed in the volumes under study, for the planes discussed in the text and marked in Figure 3.16,d. Panels **C1**: Input of the checkerboard test at the resolution of 1000 m. Panels **C2**: Input of the checkerboard test at the maximum resolution of 500 m. All the outputs are represented in Figures 3.19, 3.20, 3.21, 3.22 and 3.23, corresponding panels. The grey scale represents the inverse quality factor of the S-waves.

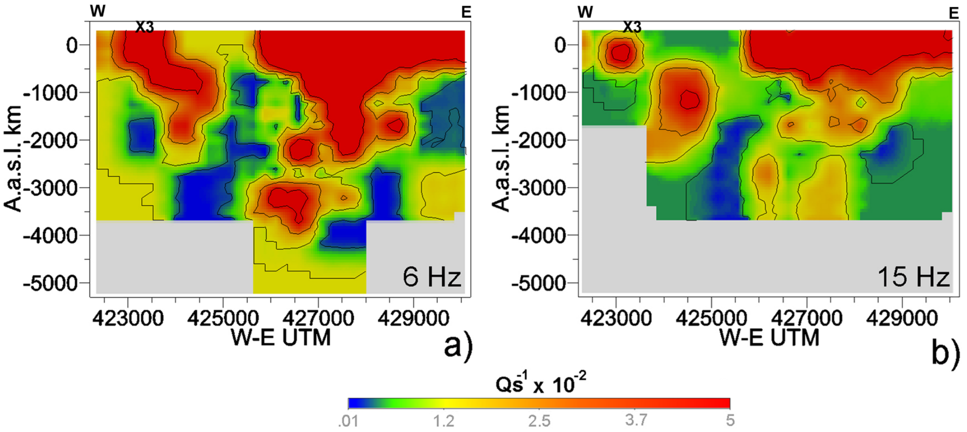

Figure 3.19: The Q_S^{-1}tomography results obtained at (**a**) 6 Hz and (**b**) 15 Hz for a W-E section crossing the areas of Mofete and Solfatara (see Figure 3.16,d).The common colour scale represents the inverse quality factor of the S-waves.

cells are coloured in light grey. The images were obtained in two frequency bands centred respectively at 6 and 15 Hz. The maximum resolution (500 m cell size) was achieved in a volume of $6 \times 3 \times 3$ km, as already discussed. The vertical cross-sections were drawn in zones selected on the basis of a compromise between the maximum resolution achievable and the presence of volcanological features at the surface. All of the depths (negative downward) are calculated with respect to the sea level.

The images at $f_C = 15$ Hz better reflect the small-scale structures than those centred at 6 Hz, due to the shorter wavelengths. Anyway, because of the longer wavelength, the data in the 6 Hz band can image a larger number of blocks, as clearly shown by formula (3.10); the volume imaged at 6 Hz is consequently greater than that at 15 Hz. Within the limits of our resolution, there is no significant difference between the images at the different frequencies, as illustrated in the example of Figure 3.19,a,b. Thus, the sole attenuation image obtained in the band centred at 6 Hz have been compared with the velocity images.

Figures 3.20, 3.21, 3.22, 3.23 show a suite of sections (tomograms) crossing the volume under study horizontally [Figure 3.20] and vertically [Figures 3.21, 3.22, 3.23]. The horizontal cross-sections of Figure 3.20 cross the volume under study, starting from a depth of −500 m and to a depth of −3500 m below sea level. The

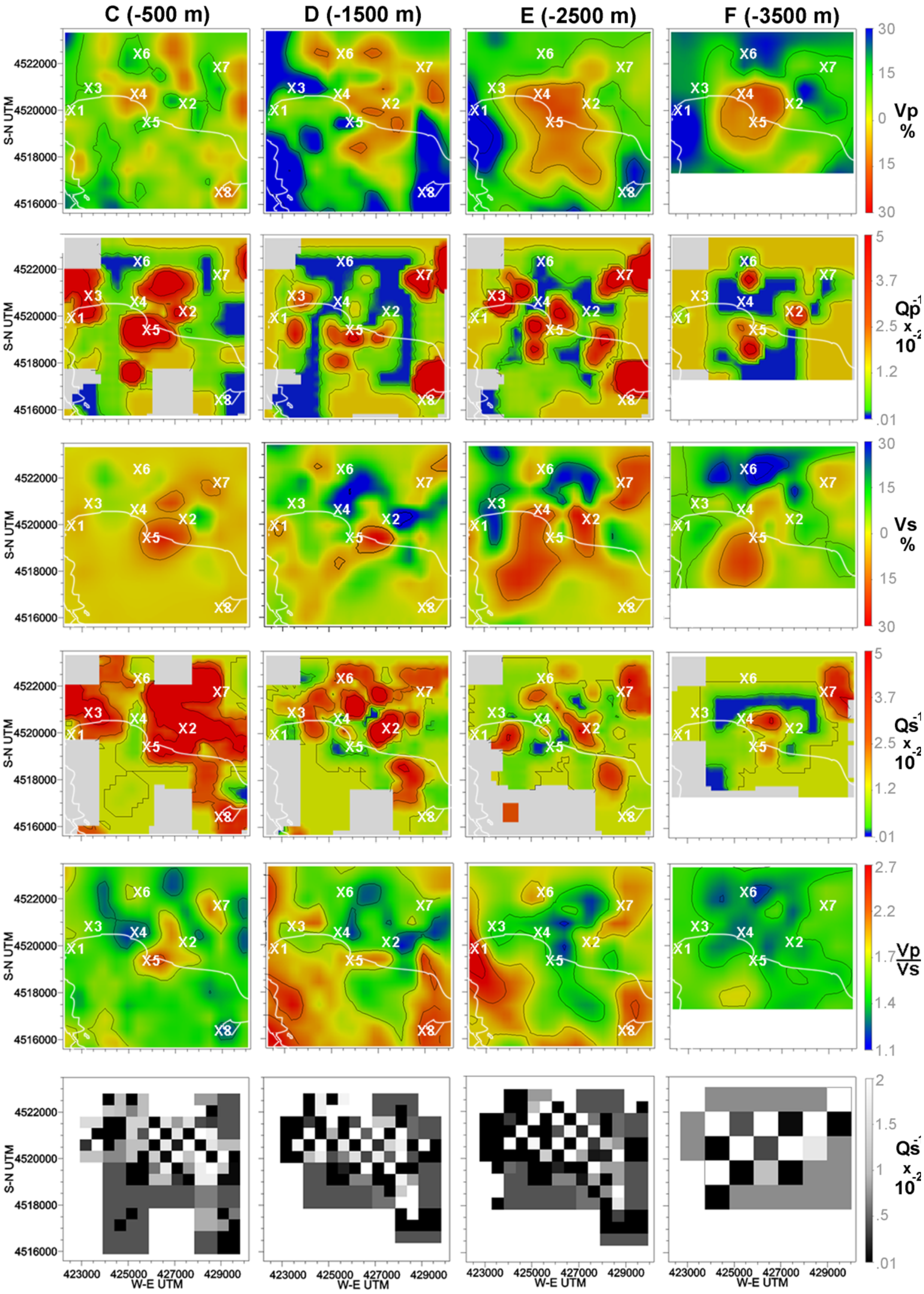

Figure 3.20: Panels **C, D, E** and **F**: Four horizontal sections crossing Campi Flegrei at different depths. First and third rows: percentage variations with respect to the average velocity (P or S) calculated on each horizontal cross-section. Second and fourth rows: wave attenuation images (P or S) for the same cross-sections. Fifth row: V_P/V_S ratio deduced by measures of absolute velocity. Sixth row: output of the resolution test for the maximum resolution available on each cross-section. The sea coast is plotted as a white line on each horizontal tomogram. The locations of the area of great volcanological interest follow the legend: X1, Mofete; X2, Solfatara; X3, Mt. Nuovo; X4, La Starza; X5, Pozzuoli; X6, San Vito; X7, Astroni-Agnano; X8, Nisida.

first and third rows represent the percent variations with respect to the average velocities calculated for each horizontal cross-section for P-waves or S-waves. The absolute velocities, as well as the V_P/V_S ratio (fifth row), have been deduced by the measures of absolute velocity made by Battaglia et al. (2008). The P-waves (second row) and S-waves (fourth row) attenuation images were plotted in the same Figure for the same cross-sections. Each parameter is at the right of each row. The sixth row shows the output of the resolution test for the maximum resolution available on each cross-section. The colour scales are represented on the right of each Figure. The sea coast, as well as the symbols corresponding to the centre of the areas of the main volcanological interest (see Figure 3.16,d) are plotted on each horizontal tomogram, except for the output of the resolution tests. The resolution test result for Q_P^{-1} are similar to the ones obtained for Q_S^{-1}. Throughout the text, only the cells with the same resolution both in Q_P^{-1} and Q_S^{-1} are discussed.

In the depth range between 0 and -2000 m (Figure 3.20,C, D) the zones of Pozzuoli (X5), Mt. Nuovo (X3), Mofete (X1) and Astroni-Agnano (X7) are characterized by high Q_P^{-1} and high Q_S^{-1}. The central and south-western parts of the volumes under Solfatara (X2) also have high P-wave and S-wave attenuation, while the northern and eastern parts have low Q_P^{-1} and high Q_S^{-1}. The San Vito region (X6) is generally characterized by low Q_P^{-1} and high or average Q_S^{-1} between -1000 m and -2000 m.

In the depth range between -2000 m and -3000 m (Figure 3.20,E) Mt. Nuovo (X3), Mofete (X1) and Astroni-Agnano (X7) are still characterized by high Q_P^{-1} and high Q_S^{-1}, while the San Vito (X6) area has low Q_P^{-1} and high Q_S^{-1}. Both the Q_P^{-1} and Q_S^{-1} attenuation images show a roughly cross-shaped high attenuation structure (red), included in a low attenuation medium (green or blue). A zone roughly located between Pozzuoli (X5) and Solfatara (X2) corresponds to the centre of the cross.

The attenuation tomograms in Figure 3.20,F, show the attenuation structure of the Campi Flegrei caldera between -3000 and -4000 m. The area is characterized by low attenuation, with two S-wave high attenuation anomalies present in this depth range. The first is located between Astroni and Agnano (X7). The P-wave attenuation in the same region is between intermediate and low. The second S-

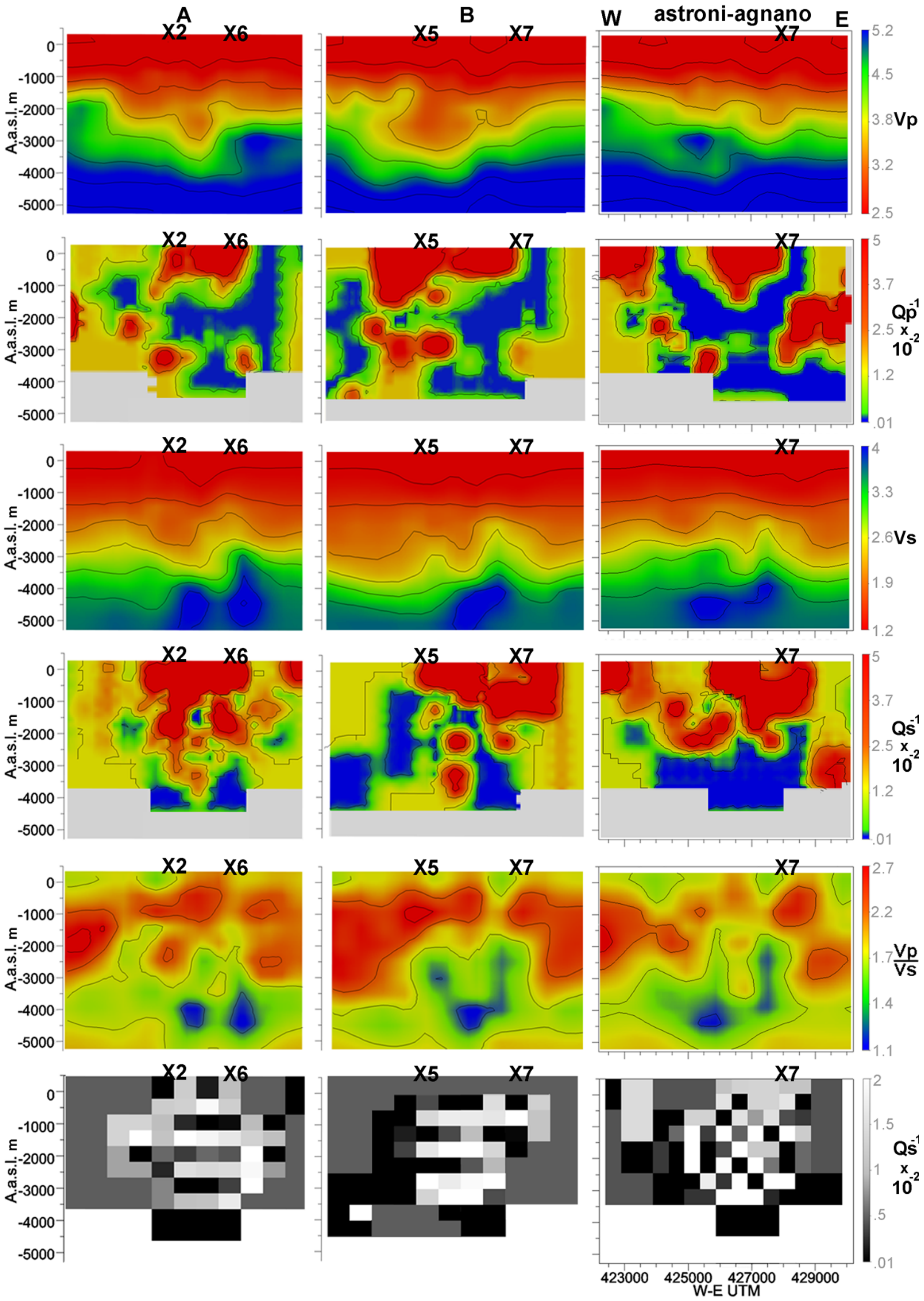

Figure 3.21: The same as figure 3.16 except for the first and third rows, where the P-wave and S-wave absolute velocity obtained by Battaglia et al. (2008) is presented. **A**, **B**: Vertical sections crossing the Campi Flegrei caldera diagonally, imaging the velocity and attenuation structures of Solfatara (X2), San Vito (X6), Pozzuoli (X5) and Astroni-Agnano (X7). No horizontal length scale is present in any tomogram. **"astroni-agnano"**: W-E section crossing the area of Astroni-Agnano, with the marker highlighting the centre of the area (X7).

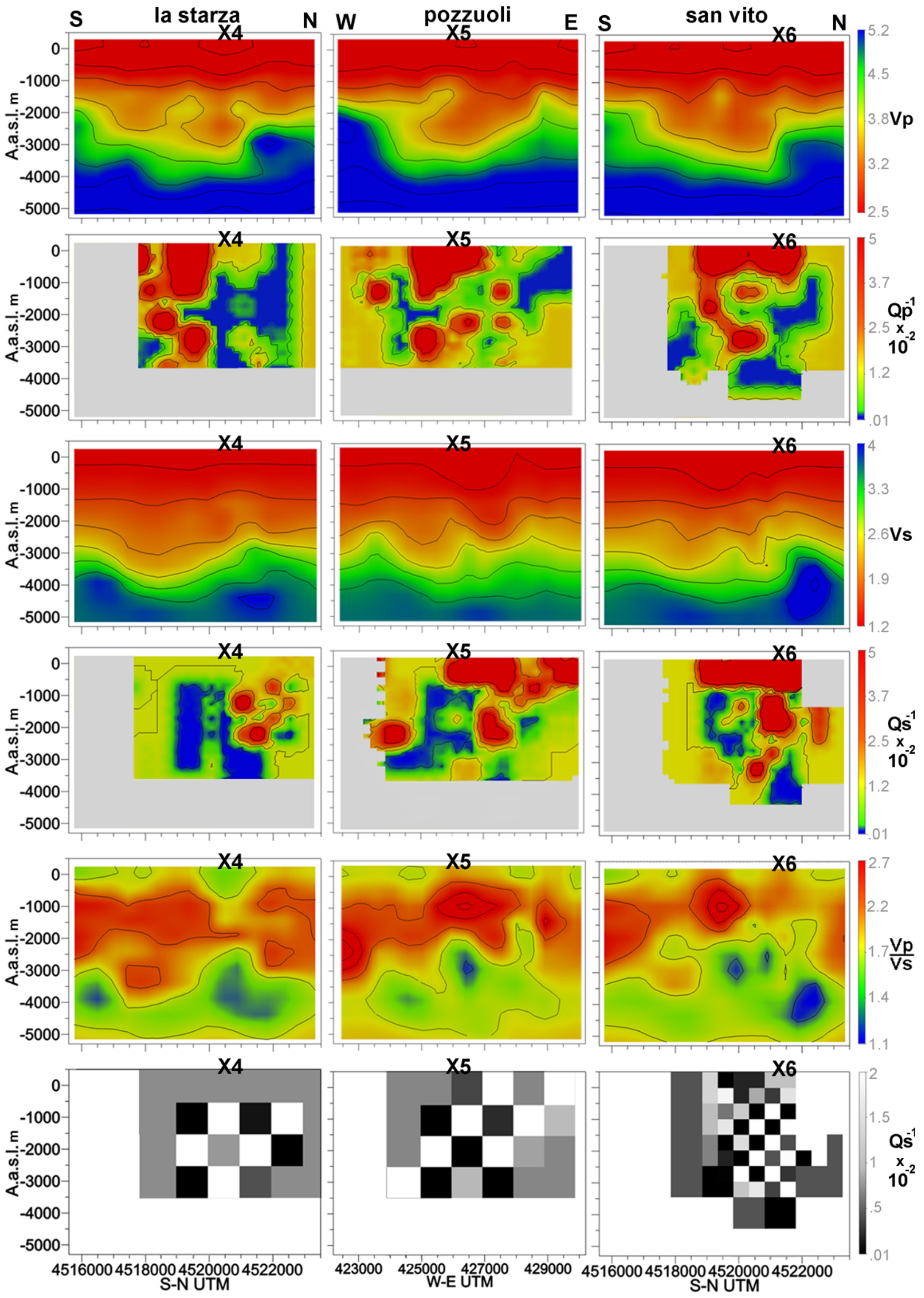

Figure 3.22: The same as Figure 3.21 for the cross-sections passing for La Starza (**"la starza"**, marker X4), Pozzuoli (**"pozzuoli"**, marker X5) and San Vito (**"san vito"**, marker X6). Each column is labelled with the name of the areas crossed by the section. Markers X4, X5 and X6 highlight the centre of La Starza, Pozzuoli and San Vito, respectively.

wave high attenuation anomaly is evident in the central part of the tomogram. The surface projection of this area is located between Pozzuoli (X5) and Solfatara (X2). This anomaly does not perfectly correlate with the P-wave high attenuation anomalies. This discrepancy might be due to a lack of resolution in this depth range.

The panels ordered in columns in Figures 3.21, 3.22, 3.23 correspond to the sections marked in Figure 3.16,d. For each column, the tomograms of V_P, Q_P^{-1}, V_S, Q_S^{-1}, $\frac{V_P}{V_S}$ and the output of checkerboard test for Q_S^{-1} are shown (top to bottom). The numbered black crosses at the top of each column mark the main features at the surface. These symbols correspond to those in Figure 3.16,d.

The tomograms in Figure 3.21,A, B, where some general important attenuation features of the Campi Flegrei caldera are revealed, are described first; then, the attenuation features of the volumes underneath the areas of main volcanological interest (Figures 3.21, 3.22 and 3.23) are discussed. Note that the Q_P^{-1} and Q_S^{-1} tomograms are always plotted in the second and fourth rows of each Figure.

In Figure 3.21, both panels A (crossing the zones of San Vito (X6) and Solfatara (X2)) and B (crossing the zones of Pozzuoli (X5) and Astroni (X7)), reveal very high attenuation regions (red) in their central parts, corresponding to the centre of the caldera, between 0 and -1000 m. Except for some small very low attenuation anomalies (blue), the Q_S^{-1} tomograms of this panels are characterized by high (red-orange) and average (yellow) attenuation between -1000 and -3000 m. Two almost vertical, nested, highly attenuative (red) structures are clearly visible in the central parts of the Q_S^{-1} images, to a depth of about -2500 m, including a small zone of low Q_S^{-1}. At the surface, these two high Q_S^{-1} structures correspond to the volcanological areas of Solfatara (X2) and San Vito (X6). The area with high S-wave attenuation under -3000 m is located at the centre of the Q_S^{-1} tomogram. The surface projection of this region corresponds to an area near Solfatara (X2). This high attenuation zone is connected with a very high S-wave attenuation structure under Solfatara (X2), located between -1000 m and -3000 m. The western side of the Q_P^{-1} tomogram has a high attenuation structure that is similar to the one shown in the left side of the Q_S^{-1} tomogram; the high Q_P^{-1} anomalies appear more heterogeneously distributed than the Q_S^{-1} anomalies. In contrast, the high Q_S^{-1} structure underneath San Vito (X6) in the depth range between -1000 and -3000

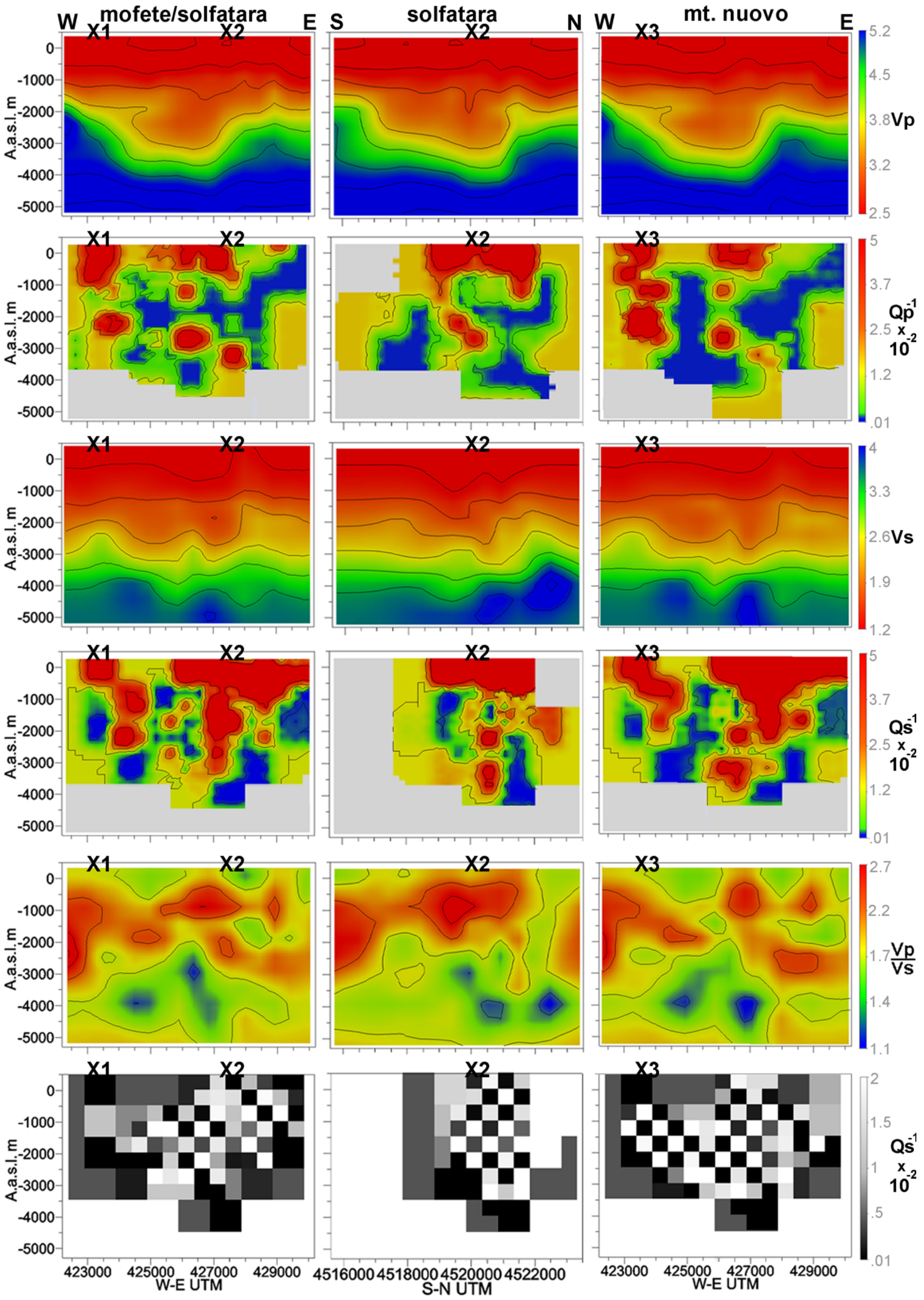

Figure 3.23: The same as Figure 3.21 for the W-E and S-N sections crossing the areas of Mofete and Solfatara (**"mofete/solfatara"**, marker X1 and X2), Solfatara (**"solfatara"**, marker X2) and Mt. Nuovo (**"mt. nuovo"**, marker X3). Each column is labelled with the name of the areas crossed by the section. Markers X1, X2 and X3 highlight the centre of Mofete, Solfatara and Mt. Nuovo, respectively.

m corresponds to a large P-wave low-attenuation area.

High P-wave and S-wave attenuation structure is evident (Figure 3.21,B) between -1000 m and -3000 m below Pozzuoli town. Below -3000 m, the sole Q_S^{-1} anomaly is evident; the area of this anomaly, to the limits of our limited resolution at this depths (compare Figure 3.20,F). It is of note that the maximum resolution is in the central parts of the tomograms of Figure 3.21,B (see sixth row).

Figure 3.21, "astroni-agnano" (marker X7), shows between 0 and -1500 m a high attenuation (P and S) surrounded by a low attenuation structure that extends down to about -3000 m.

Figure 3.22 shows the structure underneath the "La Starza" fault ("la starza", marker X4). A high Q_P^{-1} anomaly is evident in the southern part; this anomaly corresponds to very low S-wave attenuation in the same area. A low Q_P^{-1} and low Q_S^{-1} volume is seen in the central part of both tomograms, between -500 m and -4000 m. This volume corresponds to that in the western part of the Solfatara image (Figure 3.23, "mofete/solfatara") and in the "mt. nuovo" attenuation tomogram (Figure 3.22). The northern part of the "la starza" attenuation tomograms (Figure 3.22) is characterized by high S-wave attenuation between 0 m and -2500 m. The same area shows low and intermediate P-wave attenuation. The geological structure of the "La Starza" fault clearly corresponds to the vertical zone of contrast between low and high S-waves attenuation, until a depth of -2500 m (Figure 3.22, "la starza"). Below this depth, Q_P^{-1} and Q_S^{-1} are generally low.

Figure 3.22, panels "pozzuoli" (marker X5) shows a large zone of high P-wave and S-wave attenuation, extending between approximately 0 and -1000 m. Between -1000 and -3000 m the high Q_S^{-1} anomaly corresponds to a heterogeneous P-wave attenuation structure, east of the centre of Pozzuoli (X5). In the same depth range two zones of very low S-wave attenuation are located west and east of the high attenuation anomaly discussed above. The western part shows low Q_P^{-1} and Q_S^{-1}. Below -3000 m, a high Q_P^{-1} corresponding to an intermediate Q_S^{-1} area located under the centre of Pozzuoli (X5).

The northern and central parts of the "san vito" attenuation panels (Figure 3.22) show a wide area with strong P-wave and S-wave attenuation in the central part of the tomograms, between 0 and -1000 m. High attenuation anomalies also characterize the central part of the Q_S^{-1} tomogram, under the centre of San Vito

(X6), between -1000 m and -3000 m. It is of note that the volumes under the centre of San Vito (X6) have been solved at the maximum resolution (Figure 3.22, sixth row). The high Q_S^{-1} matches low-to-intermediate Q_P^{-1} between -1000 m and -3000 m. Low P-wave and S-wave attenuation is seen below -2500 m.

The W-E and S-N tomograms underneath Mofete and Solfatara are plotted in Figure 3.23; the columns are labelled with the names "mofete/solfatara" and "solfatara". The attenuation is generally strong between 0 and -1000 m, especially under the centre of Solfatara (X2) and Mofete (X1). The volume under Mofete is characterized by strong P-wave and S-wave attenuation, until a depth of -3000 m. Below -3000 m the attenuation is generally low. The volumes located under the central part of Solfatara (X2) in both "mofete/solfatara" and "solfatara" attenuation tomograms, are characterized by high (red) Q_P^{-1} and Q_S^{-1}, until around -3500 m. Figure 3.23, "mofete/solfatara" shows a zone of low Q_P^{-1} and low Q_S^{-1} between Mofete (X1) and Solfatara (X2), extending from -500 to -3500 m. This zone corresponds to the zone of maximum uplift that occurred in the 1983-84 bradyseismic crisis. The areas located eastwards (Figure 3.23, "mofete/solfatara") and northwards (Figure 3.21, "solfatara") of Solfatara (X2) show high Q_S^{-1} and high Q_P^{-1} between 0 and -1000 m. The attenuation tends to decrease at increasing depths.

Figure 3.23 shows ("mt. nuovo", marker X3) high Q_P^{-1} and high Q_S^{-1} between 0 and -3000 m. A low attenuation zone is visible below this depth. A wide zone of low Q_P^{-1} and low Q_S^{-1}, located between -500 m and -4000 m is clearly visible eastwards of Mt. Nuovo (X3). The same pattern can be seen below Mofete (X1).

A previous Q_P tomography has been obtained in the same area with a lower resolution, using a subset of the present dataset (De Lorenzo et al. 2001b). The method used in this study was based on measurement of the P-wave pulse width and rise time. Interestingly, the gross features of the images obtained by De Lorenzo (2001a) (see their Plate 1) are quite consistent with those of the present, notwithstanding the completely different approach to the estimation of the seismic signatures and the different resolution.

3.6.7 Joint interpretation of the velocity and attenuation images

From a seismological point of view, volcanic areas are complex structures that are characterized by solidified intrusions, partially molten regions, geothermally altered rocks, and intricate deposits of different shapes, thicknesses and compositions. A wide range of physical properties must be considered in discussing the results of velocity and/or attenuation tomography, as their combined interpretation is a decisive tool in discriminating volumes permeated by fluids and/or by structural discontinuities (Nakajima and Hasegawa, 2003).

In the interpretation based only on the velocity, the spatial variation of V_P mirrors the distribution of lithologies and rock properties, while the V_P/V_S ratio maps rock defects, pores and cracks, and their fluid contents. Temperature increases produce a decrease in V_P and V_S (e.g. Kern (1982)), while the causes of V_P/V_S variations with respect to temperature are still ambiguous (e.g. Christensen (1996)). Fluid-filled pores in matrix rocks affect the seismic wave velocity, causing a decrease in both V_P and V_S (e.g. Nakajima et al. (2003)). On the other hand, it has been recognized that variations in V_P/V_S of matrix rock including fluids depend not only on the kind of fluids, but also on the shape of the pores (Schmeling, 1985, Takei, 2002), which sometimes leads to ambiguous interpretations of the causes of seismic velocity anomalies. However, it is certain that melt-filled inclusions result in a high Vp/Vs (e.g. Takei (2002)).

Q_P^{-1} can be used to discriminate between water-filled media and gas reservoirs (Hansen et al. 2004), while Q_S^{-1} measures can be used to image areas of strong fracturing and melt. Both of these Q images can be used to reveal zones of hard rock and fault areas, as in Eberhart et al. (2005).

The interpretation of our findings is based on the analysis of the main features of the attenuation images, isolating the volumes characterized by strong laterally and/or in-depth contrasts. Then, these volumes are associated with those corresponding to all of the other available V_P/V_S, V_P or V_S images. The following features are found:

Hydrothermal basin under Pozzuoli

The V_S images in Figure 3.20,C, D show a minimum of V_S corresponding to high Q_P^{-1} and Q_S^{-1} in the centre of the caldera, prevalently under the city of Pozzuoli (marker X5). Looking at the "pozzuoli" panels (Figure 3.22), a very high V_P/V_S ratio (2.6) well matches the high attenuation, low velocity anomaly located east of the centre of Pozzuoli (marker X5), between 0 and -3000 m. The resolution is generally low under Pozzuoli, possibly producing the small differences in the location of the high Q_P^{-1} and high Q_S^{-1} zones. The Q_S^{-1} pattern obtained is compatible with the presence of a hydrothermal basin under the city of Pozzuoli, confirming the results of Vanorio et al. (2005).

Hydrothermal basins under Mt. Nuovo and Mofete

A zone of very strong attenuation for both P-waves and S-waves is clearly visible between the surface and -3000 m, under the Mofete (marker X1) and Mt. Nuovo (marker X3) areas (3.23,C-E). The high Q_P^{-1} and high Q_S^{-1} values of the volumes beneath the centre of these areas are very similar to the those characterizing the hydrothermal basin underneath Pozzuoli (compare the attenuation tomograms of Figure 3.23, "mt. nuovo", and Figure 3.22, "pozzuoli"). Beneath the centre of Mofete (Figure 3.23, "mofete/solfatara", marker X1) and the center of Mt. Nuovo (Figure 3.23, "mt. nuovo", marker X3), the low V_S, as well as the high V_P/V_S ratio, between 0 m and -3000 m are in good agreement with the high Q_P^{-1} and Q_S^{-1} in the attenuation tomograms. The low V_S, high V_P/V_S and high attenuation is interpreted as due to the high circulation of fluids affecting the rocks under Mofete and Mt. Nuovo, between the surface and -3000 m. Todesco et al. (2003) recognized two aquifers in the Mofete area, with good lateral continuity: a shallow one between -150 m and -300 m, with temperatures of $100 \div 130$ °C, and a deeper one between -1250 m and -1600 m, with a temperature of 300 °C. Their positions closely match with the orange-coloured volumes (high S-attenuation) in Figure 3.19,b. In our interpretation, these high attenuation zones mark a pathway of H_2O (high temperature vapours) and CO_2 up to the surface, towards the area surrounding Mt. Nuovo. The seismological characteristics of these zones are similar to those of the other hydrothermal basin located under Pozzuoli, even if its lateral and vertical dimensions are different (Figure 3.22, "pozzuoli").

Small gas reservoirs: San Vito and the north-eastern part of Solfatara

The high Q_P^{-1}, high Q_S^{-1} and high V_P/V_S zones at -500 m beneath the San Vito region (3.20,C, marker X6) correspond to zones with geomorphological evidences of shallow complex structures (Di Vito et al. 1999). The San Vito region is characterized by high temperature rocks at shallow depths, and by conductive heat transfer, as inferred by measurements in geothermal wells (Todesco et al., 2003). The V_P/V_S ratio measured in this area at -1500 m is low (between 1.2 and 1.6), due to the low V_P and high V_S (Figure 3.20,D, marker X6). The high Q_S^{-1} and low Q_P^{-1} anomalies, that are particularly evident in Figure 3.22, "san vito", at around -2000 m, together with the low V_P/V_S ratio and the low V_P (Figure 3.20,D) are compatible with the presence of gas (CO_2) (see Hansen et al. (2004) for more complete discussion). Degassing processes in the area have been interpreted by Todesco et al. (2003) as due to the escape of fluids from a magma chamber towards geothermal reservoirs, and from there to the surface.

A low Q_P^{-1}, low V_P, low V_P/V_S and high V_S zone located prevalently in the north-eastern part of Solfatara is characterized by high Q_S^{-1}, and is clearly visible at -500 and -1500 m in Figure 3.20,C, D (marker X2). The "mofete/solfatara" and "solfatara" panels (Figure 3.23, marker X2) show the vertical extensions of the volumes characterized by these parameters in their eastern and northern parts, respectively. Hansen et al. (2004) interpreted similar seismological evidence as due to the presence of gas; many manifestations of fumaroles at the surface confirm the presence of gas reservoirs in this area, between 0 and -2000 m (see e.g. Caliro et al. (2007)). The central and south-western parts of the Solfatara are characterized by high Q_P^{-1}, high Q_S^{-1}, low V_P, low V_S and high V_P/V_S, as expected for a strongly fractured medium permeated by fluids (Figure 3.23, "mofete/solfatara" and "solfatara").

Attenuation materials near the zone of maximum uplift: La Starza fault.

In the western part of the attenuation tomograms of Figure 3.20,C, the high Q_P^{-1} and high Q_S^{-1} zones of Mofete-Mt. Nuovo (markers X1 and X3) and Pozzuoli (marker X5) are separated by a S-N oriented low Q_P^{-1} and low Q_S^{-1} structure. This low attenuation volume is characterized by low-to-intermediate V_P, high V_S and low V_P/V_S. The same results can be partially retrieved in Figure 3.20,D. In Figure 3.23, "mofete/solfatara" and especially in "mt. nuovo", this almost vertical low Q_P^{-1} and low Q_S^{-1} structure is clearly evident, east of the centre of Mofete (X1) and Mt. Nuovo (X3), between -500 and -4000 m. The low Q_P^{-1} values are strictly correlated with the low Q_S^{-1} and low V_P/V_S values, (e. g. Figure 3.23, "mt. nuovo"). The zone between the centre of Mofete (X1) and the centre of Solfatara (X2) in Figure 3.23, "mofete/solfatara", suffered the maximum surface uplift in the 1983-1984 bradyseismic crisis; as clearly shown in the attenuation tomograms of Figure 3.20,C, this zone is characterized by strong vertical contrast between the low S-N attenuation structure described above and the high attenuation materials underneath Pozzuoli-Solfatara.

The vertical trace of the La Starza fault, marker X4, located west of Pozzuoli-Solfatara, is clearly depicted as a zone of strong contrast for Q_S^{-1} and V_P/V_S, between 0 and -2500 m (Figure 3.22, "la starza"). The presence of fumaroles at the surface (Di Vito et al. 1999) lead us to interpret the presence of high Q_S^{-1} and high V_P/V_S in the northern part of the tomograms as due to a hard rock medium filled with fluids (Hansen et al. 2004). The high Q_S^{-1} materials north of La Starza (Figure 3.22, "la starza", marker X4) are connected with the hydrothermal basin under the Mofete-Mt. Nuovo area (Figure 3.23, "mt. nuovo", marker X3) and to the gas reservoirs under San Vito (Figure 3.22, "san vito", marker X6).

Hydrothermal basin under Astroni-Agnano

An high Q_S^{-1} zone shows good correlation with low V_P, low V_S and high V_P/V_S under Agnano (X7), between 0 m and -3500 m (Figure 3.21, the eastern part of panels "astroni-agnano"). A relevant aquifer with temperatures of the order of 250° C has been described below the Agnano Plain at -1400 m in different studies (see Todesco et al. (2003), and references therein). For this area, high Q_P^{-1} and high Q_S^{-1} values are measured, which are in agreement with this interpretation. The high attenuation anomaly of Astroni-Agnano extends to -3500 m (Figure 3.20,F, marker X7), where it matches an intermediate (around 1.6) V_P/V_S ratio area, suggesting a hydrothermal basin extended vertically between 0 and -3000 m.

High attenuation volumes at -2500 m.

The attenuation and velocity features between -2000 m and -3000 m are shown in Figure 3.20,E. These tomograms can be interpreted as being produced by hard rock volumes (characterized by high velocity and low attenuation), surrounding a heterogeneous low velocity and high attenuation structure, with its centre located between Pozzuoli (X5) and Solfatara (X2). The low V_P/V_S ratio (lower than 1.5) in the centre of the low velocity and high attenuation structure indicates the absence of melt in the centre of the area under study, as recently highlighted by Vanorio et al. (2005) and Vanorio et al. (2008). Three zones of high Q_P^{-1}, high Q_S^{-1}, low V_P, high V_S, and high V_P/V_S in the northern and western parts of Figure 3.20,E, are situated between Mt. Nuovo (X3) and San Vito (X6) (Figure 3.20,E, north-western part), beneath Astroni-Agnano (X7) (Figure 3.20,E, north-eastern part) and beneath the sea zone north-west of Nisida (Figure 3.20,E, marker X8), respectively. Due to the combination of these parameters, these regions can be interpreted as zones where the presence of fluids or melt is possible, in agreement with previous volcanological interpretations (D'Antonio et al., 1999). However, the resolution in this areas is generally low; moreover, the extended sea areas south-west of Pozzuoli are not imaged by the present S-waves tomography, and will not be discussed.

The materials under -3000 meters

Zollo et al. (2008) recently observed a seismic interface located -2700 m under the Campi Flegrei caldera, using seismic reflection analysis; the sharp increment in both V_P and V_S at this depth was also seen in the present study in all of the velocity tomograms. It matches the S-wave attenuation contrast well in a wide area around the centre of the caldera (e.g. Figure 3.21, "astroni-agnano"). The velocity and attenuation tomograms of the caldera between -3000 m and -4000 m are discussed in Figure 3.20,F. The V_P/V_S ratio is generally low. The Q_S^{-1} tomogram shows low attenuation materials, except for two high S-wave attenuation anomalies beneath Pozzuoli-Solfatara (Figure 3.20,F, markers X4, X5 and X2) and Astroni-Agnano (Figure 3.20,F, marker X7). The anomaly under Astroni-Agnano does not clearly match any high Q_P^{-1} anomaly, and corresponds to an average value of V_P/V_S (around 1.6). This feature are interpreted due to a zone permeated by fluids that extends above -3000 m, which is resolved at a low resolution. The Q_S^{-1} anomaly beneath Solfatara and Pozzuoli reaches a maximum depth of -4500 m (Figure 3.23, "mt. nuovo", central part). Interestingly, Figure 3.21,A shows that on average the values of the Q_S^{-1} anomaly under -2500 m are of the order of $1.8 * 10^{-2}$, lower than those characteristic of the high attenuation, fluid-filled materials located -1000 meters above $(4 * 10^{-2})$. The Pozzuoli-Solfatara anomaly at -3500 m is laterally surrounded by lower attenuation materials (Figure 3.20,F), and corresponds to a low V_P and low V_S anomaly surrounded by higher velocity materials. As usual, the Q_P^{-1} tomogram is more heterogeneous, with three high attenuation zones located under San Vito, Pozzuoli and Solfatara. At the limit of our resolution, the high Q_P^{-1} anomaly of Pozzuoli and Solfatara can be related to the unique high Q_S^{-1} anomaly nearby. The attenuation pattern at this depth would indicate the presence of small magma patches in the area, even though the low V_P/V_S would not suggest a large magma batch under Pozzuoli.

Nakajima et al. (2003) have shown that a narrow conduit with low V_P and low V_S in the upper crust beneath the Naruko volcano does not have an high V_P/V_S value. Similar low-velocity ratio conduits have been reported in Redoubt volcano, Alaska (Benz et al., 1996), Mt. Etna, Italy (Villaseñor et al., 1998), Aso volcano, Japan (Sudo and Kong, 2001) and Mt. Vesuvius (Scarpa et al. 2002), and they have been interpreted as highly fractured zones and/or active magma conduit systems. Low V_P/V_S anomalies have also been detected in geo- and hydro-thermally active areas such as the Yellowstone caldera (Chatterjee et al., 1985), Coso Region, California (Walck, 1988) and Geysers geothermal area, California (Julian et al., 1996). In the present study, the velocity anomalies inside the areas of strong attenuation at -3500 m can be explained by the presence of the vapour phase in the rock matrix, on the basis of the theory of Takei (2002). Our experimental evidence suggests that the hot vapour phase has a dominant role in causing low V_P/V_S anomalies in Campi Flegrei, since the thermal activity in this area is very high. Indeed, it is likely that vapour- filled fracture zones or volcanic deposits are distributed inside the caldera, although not exactly in its centre. Water coming from the nearby fluid-filled materials, located 1000 m above may partially contribute to the cause of these anomalies, which cannot be explained by the presence of water alone, since water cannot reduce V_P/V_S to the values obtained here (V_P/V_S around 1.4).

When constrained by the results recently obtained by Zollo et al. (2008) revealing a melt reservoir at -7500 meters, the joint interpretation of the velocity and attenuation features lead us to the final concept that the attenuation anomaly around -3500 m could constitute the upper part of a vapour-filled conduit. This conduit may be connected with the sill at -7500 m, and may contribute to the transport of magmatic gases towards the surface, as schematically proposed by Nakajima et al. (2003) for the Naruko volcano. The aquifers interact with this conduit, favouring the upward circulation of hot non-magmatic vapour that constitute the main part of the fumarole gases at surface (Caliro et al., 2007).

It is important to conclude with a note that all of the attenuation images in this study were obtained with passive data recorded over a small time interval during the 1983-84 crisis. The comparisons are instead done using images obtained using a dataset spanning a larger time interval. Consequently, possible changes in the geological structure, such as those revealed at Etna (Patanè et al., 2006), due to the ongoing dynamics of Campi Flegrei (see Saccorotti et al (2007) and references therein) cannot be imaged.

3.7 Conclusions

The heterogeneity of the propagation medium in a volcanic area make difficult a robust and stable estimate of seismological related quantities. On the other hand, heterogeneity produces a diffuse wavefield which can be used to improve the stability of the seismic attributes estimates. The CN method applied to S-wave attenuation tomography results to be a robust and stable method, fully independent of the source function and the site term. Moreover, the use of adequate phenomenological forward scattering models almost allows the removal of the source radiation pattern. With the joint application of the CN (and SD) methods with a multi resolution inversion, the objective of achieving a resolution comparable with that of velocity tomography (at least in a small area) has been accomplished. The codes developed measure the attenuation parameters in block of different sizes, with a typical non-uniform cell size scheme. The codes follow a process of constraining (or updating) of the data at higher resolution. The results obtained have been interpreted jointly with the velocity tomography results and the evidences coming from geological field.

The multiresolution attenuation tomography of Mt. Vesuvius complements the single-resolution attenuation tomography results, solving a 300 m cell size in the volume beneath the central crater, located in the depth range between approximately 0 (the sea level) and -3500 m. The improved dataset (the waveforms are more than doubled) improved both stability and robustness at 900 meters resolution. The improved resolution allowed a better definition of the 3-D pattern of both Q_P^{-1} and Q_S^{-1}, thus improving the joint interpretation of previous velocity images with the present attenuation structure. The essential results show that no magma patches with dimensions larger than the cell size are visible in the images, and confirm the presence of shallow hydrothermal reservoirs (between -700 and -2300 m) evidenced by geochemical studies. The high resolution achievable between 0 and -1500 m allowed a small scale imaging of the residual solidified lava emitted during the last eruptions, leading to the interpretation in terms of large patches of gas located in the first kilometer below sea level. The low attenuation, high velocity area, located at -500 m under the cone is connected with the carbonate basement, whose interface is located around -1500 m. Interestingly, the

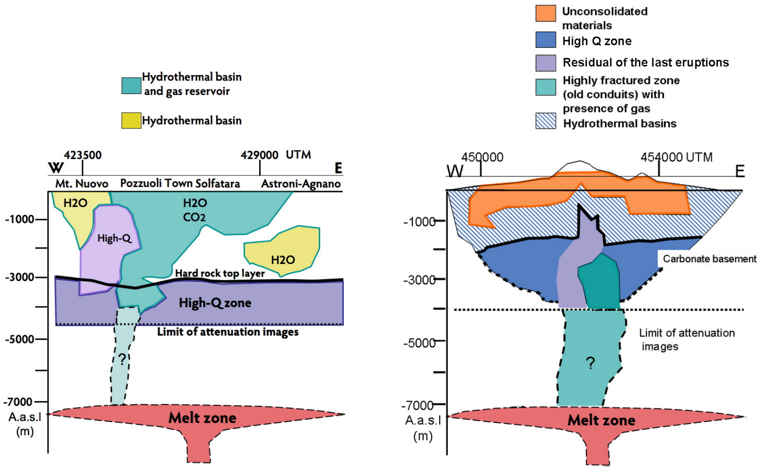

Figure 3.24: Schematic interpretation of the results obtained at Mt. Vesuvius and Campi Flegrei, based on velocity and attenuation tomographies.

zone of maximum seismic energy release, imaged for the first time at a resolution of 900 meters, coincides with a high attenuation and low velocity anomaly, easily interpretable as due to the presence of a cracked zone inside the limestone layer.

The results obtained in the Campi Flegrei are more various, due to the distribution of sources and station, that allowed the imaging of wide area centered at Pozzuoli- Solfatara. A volume characterized by high attenuation (P-waves and S-waves), low velocity (P and S) and high V_P/V_S is present beneath Pozzuoli between 0 and -3000 m, and confirms the presence of a hydrothermal basin in this area. The same characteristics are also evident for the volumes beneath Mofete and Mt. Nuovo in the upper 2500 m of crust, which suggests the presence of a one (or two) small hydrothermal basin beneath this area. Finally, a third high Q_P^{-1} and high Q_S^{-1} volume has been interpreted as a fluid-filled structure under Astroni-Agnano, between -1000 m and -3500 m. There are two volumes with high Q_S^{-1}, low Q_P^{-1} and low V_P eastward of the Solfatara crater and beneath San Vito, at a shallow depth: this evidence is compatible with the presence of a gas reservoir between 0 and -2500 m. The maximum uplift zone during the 1983-84 bradyseismic crisis is imaged as a strong S-wave attenuation contrast; in particular, the zone of high seismicity during this 1983-84 seismic sequence is practically coincident with the "La Starza" structure, which is depicted by this contrast.

High P-wave and S-wave attenuation anomalies between -2000 and -3000 m coincide with high V_P/V_S ratios in three different zones around Pozzuoli-Solfatara, and may indicate the presence of small melt or fluid batches. In the same depth range, the low V_P/V_S ratio excludes the presence of melt beneath Pozzuoli and Solfatara, as discussed by other authors, who suggested the presence of fractured, overpressured, gas-bearing formations in the same volume. The top of a laterally extended low P-wave and S-wave attenuation zone is present around -3000 m, in agreement with the discontinuity described by Zollo et al. (2008) using seismic reflection techniques, and observed by Battaglia et al. (2008) using seismic velocity tomography. This laterally extended discontinuity appears to be laterally uniform, but includes two visible high Q_S^{-1} anomalies. The attenuation anomaly located beneath Pozzuoli-Solfatara is characterized by low V_P, low V_S and a low V_P/V_S ratio. This evidence is interpreted as due to the presence of a vapour-filled conduit, as a pathway for the magmatic gas flow, possibly connected with the melt sill recently imaged by Zollo et al. (2008) at -7500 m.

In the future, the CN method will also be employed on a bigger scale to retrieve the attenuation structure of the Andes. The images obtained with the methods applied in this thesis will also be interpreted by using cluster analysis. A final sketch, retrieved from both the Mt. Vesuvius and Campi Flegrei images, is presented in Figure 3.24. The interpretation in terms of a gas filled conduit connecting the sill located around -7000 m to the surface fits well the presence of gas around -3500 m in the two areas. These results are expected to add important constraints for the numerical models that will be adopted to simulate the next eruption, and consequently to be used for Civil Defense purposes.

Appendix A

Mt. Vesuvius and Campi Flegrei multi-resolution schemes

In this Appendix the details relative to the multi-resolution schemes applied to the areas of Mt. Vesuvius and Campi Flegrei are explained. First, the three-step inversion scheme described in the points listed between 2 and 5 in section 3.3.4 is treated; afterwards, the two-step inversion scheme which leaded to the results at Campi Flegrei is fully described.

A.1 Mt. Vesuvius

Point 2: estimate of the Average inverse Quality Factor (AQF).

S-waves AQF is calculated using the coda normalization method applied to the whole data-set; formula (2.20) becomes:

$$d_k^C = \frac{1}{2\pi f} \ln(\frac{1}{P(f,t_c)}) - \sum_{b=1}^{N\_cells} l_{kb} s_b \left[Q_T^{-1}\right]^C . \tag{A.1}$$

The inverse AQF for S waves (Q_T^{-1}) is obtained:

$$(Q_T^{-1})^{12} = 0.010 \pm 0.003$$

$$(Q_T^{-1})^{18} = 0.019 \pm 0.003$$

where the above index is referred to the center frequency.

Uncertainty is estimated assuming that each spectrum is affected by a 10% of error due to the noise. This result is in good agreement with previous Q-estimate for S waves in the area (Del Pezzo et al. 2006b). P-waves AQF has been already calculated by (Bianco et al. 1999).

Point 3: cell dimension of 1800 m.

The inversion problem of formula (2.21) and formula (2.30) are solved for a grid of 1800 meters step. The equation can be rewritten as:

$$\tilde{d}_k^{C,D} = \sum_{b=1}^{N\_cells\_1800} G_{kb}^{1800}[(\delta Q_b^{1800})^{-1}]^{C,D} \tag{A.2}$$

where the superscript 1800 stands for the step of the grid, while the superscript C, D takes into account the different methods used. The elements of the inversion matrix, G_{kb}^{1800}, are the length of the $k-th$ ray segment in the 1800-meter side $b-th$ block, l_{kb}^{1800} , multiplied for his slowness s_b^{1800}:

$$G_{kb}^{1800} = l_{kb}^{1800} s_b^{1800} \tag{A.3}$$

Applying formula (3.1), only the blocks crossed by at least $n_R = 35$ rays are considered. The problem is solved separately for each frequency band, by using the least squares algorithm "lsqlin" deployed in MATLAB.

The percentage reduction of the residuals, computed using the formula in Gubbins (2004), results to be 65%. The inverse quality factor of each 1800 meters block b is given by:

$$(Q_b^{1800})^{-1} = Q_T^{-1} + (\delta Q_b^{1800})^{-1} \tag{A.4}$$

Point 4: cell dimension of 900 meters.

The data vector obtained solving the inversion schemes of formula (2.22) and formula (2.31) can be updated with the solutions obtained in the previous steps. Each ray crosses a medium whose quality factor is no more Q_T, and is affected by the quality factors of the cube that it effectively crosses. The elements of the data vector must represent the effect of the attenuation structure obtained in the previous steps. They become respectively:

$$(\widetilde{d_k^C})^{1800} =< \frac{1}{2\pi f}\ln(\frac{1}{P(f,t_c)}) > -d_k^C - Q_T^{-1}\sum_{b=1}^{N\_cells\_900} l_{kb}^{900}s_b^{900} - \sum_{b=1}^{N\_cells\_900} l_{kb}^{900}s_b^{900}(\delta Q_b^{-1})^{1800,C} \quad \text{(A.5)}$$

and

$$(\widetilde{d_k^D})^{1800} =< \frac{t_k}{Q_k} >^{1800} -d_k^D - Q_T^{-1}\sum_{b=1}^{N\_cells\_900} l_{kb}^{900}s_b^{900} - \sum_{b=1}^{N\_cells\_900} l_{kb}^{900}s_b^{900}(\delta Q_b^{-1})^{1800,D} \quad \text{(A.6)}$$

where $(\delta Q_b^{-1})^{1800,C}$ and $(\delta Q_b^{-1})^{1800,D}$ are respectively the solutions obtained with the CN method and the SD method for 1800 meters side blocks and that where assigned to the N_cells_900 blocks of 900 meters side crossed by the $k-th$ ray. In the SD method the constant value $< \frac{t_k}{Q_k} >^{1800}$ has also been updated with the informations obtained in the previous step. The inversion problem becomes, for a resolution of 900 meters:

$$(\widetilde{d_k^{C,D}})^{1800} = \sum_{b=1}^{N\_cells\_900} G_{kb}^{900}[(\delta Q_b^{900})^{-1}]^{C,D} \quad \text{(A.7)}$$

where the superscript 900 stands for the step of the grid and the $(\delta Q_b^{900})^{-1}$ are the inverse variations respect the inverse quality factor of the 1800 meters cube in which they are contained. The elements of the inversion matrix, G_{kb}^{900}, are the length of the $k-th$ ray segment in the 900-meters side $b-th$ block l_{kb}^{900} multiplied for his slowness s_b^{900}:

$$G_{kb}^{900} = l_{kb}^{900}s_b^{900} \quad \text{(A.8)}$$

where only the blocks crossed by at least $n_R = 17$ rays are3 considered (see equation (3.1)). The inversion is linear and the average of the $(\delta Q_b^{900})^{-1}$ can be constrained to be zero. The inverse quality factor of each 900 meters block b is given by:

$$(Q_b^{900})^{-1} = Q_T^{-1} + (\delta Q_b^{1800})^{-1} + (\delta Q_b^{900})^{-1} \tag{A.9}$$

while the percentage reduction is 70% in residual.

Point 5: cell dimension of 300 meters.

The last step is achieved upgrading the data vectors writing the following two formulas:

$$\begin{aligned}(\widetilde{d_k^C})^{900} =< \frac{1}{2\pi f}\ln(\frac{1}{P(f,t_c)}) > -d_k^C - Q_T^{-1}\sum_{b=1}^{N\_cells\_300} l_{kb}s_b - \\ \sum_{b=1}^{N\_cells\_300} l_{kb}s_b(\delta Q_b^{-1})^{1800,C} - \sum_{b=1}^{N\_cells\_300} l_{kb}s_b(\delta Q_b^{-1})^{900,C}\end{aligned} \tag{A.10}$$

and

$$\begin{aligned}(\widetilde{d_k^D})^{900} =< \frac{t_k}{Q_k} >^{900} -d_k^D - Q_T^{-1}\sum_{b=1}^{N\_cells\_300} l_{kb}s_b - \\ \sum_{b=1}^{N\_cells\_300} l_{kb}s_b(\delta Q_b^{-1})^{1800,D} - \sum_{b=1}^{N\_cells\_300} l_{kb}s_b(\delta Q_b^{-1})^{900,D}\end{aligned} \tag{A.11}$$

where $(\delta Q_b^{-1})^{900,C}$ and $(\delta Q_b^{-1})^{900,D}$ are the solutions obtained in the previous steps that Ire assigned to a number of N_cells_300 blocks of 300 meters side, crossed by the $k-th$ ray. As before, the constant value $< \frac{t_k}{Q_k} >^{900}$ has been updated with the informations obtained in the previous steps. The inversion problem becomes:

$$(\widetilde{d_k^{C,D}})^{900} = \sum_{b=1}^{N\_cells\_300} G_{kb}^{300}[(\delta Q_b^{300})^{-1}]^{C,D} \tag{A.12}$$

where the superscript 300 stands for the grid step, and the elements of the inversion matrix, G_{kb}^{300}, are given by the length of the $k-th$ ray segment in the $b-th$ block, l_{kb}^{300} , multiplied for his slowness s_b^{300}:

$$G_{kb}^{300} = l_{kb}^{300}s_b^{300} \tag{A.13}$$

applying formula (3.1), only blocks crossed by at least $n_R = 5$ rays are considered. The percentage reduction in residual is 94%. The inverse quality factor of each 300 meters block b is given by:

$$(Q_b^{300})^{-1} = Q_T^{-1} + (\delta Q_b^{1800})^{-1} + (\delta Q_b^{900})^{-1} + (\delta Q_b^{300})^{-1}. \tag{A.14}$$

A.2 Campi Flegrei

The inversion scheme will be described in the following points, in analogy with what has been done for Mt. Vesuvius (section 3.3.4).

1. The seismic attributes are calculated both for the CN method (the spectral ratio) and the SD method (the vector d_k^S of Equation (2.31)).

2. P-wave and S-wave inverse quality factors averaged over the entire volume (Q_{PT}, Q_{ST}) are estimated using the slope-decay method and the coda-normalization method, respectively, applied to the whole dataset for each frequency band; the results (Table 3.15) are in good agreement with previous Q estimates in the area (De Natale et al., 1987, De Lorenzo et al. 2001b).

3. The problems of formula (2.21) and formula (2.30) are solved for a volume divided into cubic blocks of 1000 m sides, using a positivity constraint, taking into account that each ray is characterized by the average attenuation factor. Then, each 1000 m side block is divided in 8 blocks with 500 m sides, and the inverse quality factors thus calculated, $(Q_b^{-1})^{1000}$, are assigned to each of these cubes.

4. The problem is solved for the 500 m cell size resolution in the inner volume of Figure 1a-c, taking into account that each ray is characterized by the attenuation factor that has been obtained in the previous step. Thus, we obtain the new quantity $(\delta Q_b^{-1})^{500}$, which represents the variation from the inverse quality factor $(Q^{-1})^{1000}$assigned to the 1000 m block in the previous step.

It is of note that while the data vectors and the coefficient matrices need to be recalculated at each scale, the inversion problem is always formally the same, and is given by formula (2.21) and formula (2.30). It is also important to note that, at each step, we accept the solutions for the blocks in which the number of ray segments , n_R, is given by:

$$n_R \geq \frac{4Block\_side}{\lambda}. \tag{A.15}$$

On the assumption that the directions of ray segments are randomly distributed in each block, This empirically determined threshold would ensure that each block is homogeneously sampled. The empirical coefficient 4 in this Equation has been determined looking at the robustness test, to obtain sufficiently robust estimates with the minimum possible coefficient value. The details regarding how the data vectors and coefficient matrices are upgraded at each scale are now described explaining the details relative to points 2-4.

Point 2: Estimation of the average inverse quality factor.

P-wave and S-wave average inverse quality factors (AQFs) are calculated using slope-decay method and the CN method, respectively, applied to the whole dataset; formula (2.20) and formula (2.37) become:

$$d_k^{S,C} = \sum_{b=1}^{N\_cells} l_{kb} s_b \left[Q^{-1}_{PT,ST}\right]^{S,C} \tag{A.16}$$

where the indices S and C refer to the method used to obtain P-wave and S-wave AQFs. The AQF for P-waves (Q^{-1}_{PT}) is obtained using the least squares algorithm:

$$(Q^{-1}_{PT})^6 = 0.005 \pm 0.002$$

$$(Q^{-1}_{PT})^{15} = 0.003 \pm 0.001$$

where the above index is referred to the centre frequency. Using the error estimates obtained by De Natale et al. (1987) and Del Pezzo et al. (1993) for the k_0 terms and the amplifications $T_j(f)$, and as the uncertainties that affect the spectral amplitudes and the corner frequencies are 10% and 25%, respectively, the percentage of standard deviation on the data vector d is 30%. Using the covariance matrix of the single parameter inversion problem (see e. g. Gubbins (2004)) a 30% error to the estimate of Q^{-1}_{PT} in each frequency band is assigned.

The AQF for S-waves (Q_{ST}^{-1}) in the same frequency bands, measured using CN method, is:

$$(Q_{ST}^{-1})^6 = 0.013 \pm 0.003$$

$$(Q_{ST}^{-1})^{15} = 0.008 \pm 0.002.$$

The uncertainty that affects the data vector d_k^C is 20%. As in the previous step the covariance matrix is used, obtaining a 20% percent error on Q_{ST}^{-1} at each frequency band. The result is in good agreement with the one obtained in section 1.2.4 using the dependence of the average quality factor from frequency.

Point 3: Cell dimension of 1000 m.

The inversion problem of formula (3.9) and formula (2.37) is solved for a grid of 1000 m steps. Both the formulas can be rewritten as:

$$\tilde{d}_k^{C,S} = \sum_{b=1}^{N\_cells\_1000} G_{kb}^{1000}[(\delta Q_b^{1000})^{-1}]^{C,S} \tag{A.17}$$

where the superscript 1000 stands for the step of the grid, while the superscript C, S takes into account the different methods used. The elements of the inversion matrix, G_{kb}^{1000}, are the length of the $k-th$ ray segment in the 1000-m side $b-th$ block, l_{kb}^{1000} , multiplied for his slowness s_b^{1000}:

$$G_{kb}^{1000} = l_{kb}^{1000} s_b^{1000} \tag{A.18}$$

Applying formula (A.15) to the inversion problem for P-waves, only blocks crossed by at least $n_R = 7$ rays for the frequency band centered at 6 Hz are considered, and $n_R = 17$ at 15 Hz. The same formula applied to the inversion problem for S-waves lead us to consider only the blocks crossed by at least $n_R = 12$ rays for the frequency band centred at 6 Hz and $n_R = 30$ at 15 Hz. The problem is solved separately for each frequency band, by using the least squares algorithm "lsqlin" deployed in MATLAB.

The percentage reduction of the residuals, computed using the formulas in Gubbins (2004), is 50%. The inverse quality factor of each 1000 meters block b for

P-waves or S-waves is given by:

$$(Q_b^{1000})^{-1} = Q_{PT,ST}^{-1} + (\delta Q_b^{1000})^{-1} \tag{A.19}$$

Point 4: Cell dimension of 500 meters.

The data vector obtained solving the inversion schemes of formula (3.8) and formula (2.35) can be updated with the solutions obtained in the previous steps. Each ray crosses a medium for which the quality factor is no more Q_T, and is affected by the quality factors of the cube that it effectively crosses. The elements of the data vector must represent the effects of the attenuation structure obtained in the previous steps. These become, respectively:

$$\begin{aligned}(\widetilde{d_k^C})^{1000} =& < \frac{1}{2\pi f}\ln(\frac{1}{P(f,t_c)}) > -d_k^C - Q_T^{-1}\sum_{b=1}^{N\_cells\_500} l_{kb}^{500} s_b^{500} \\ & - \sum_{b=1}^{N\_cells\_500} l_{kb}^{500} s_b^{500} (\delta Q_b^{-1})^{1000,C}\end{aligned} \tag{A.20}$$

and

$$\begin{aligned}(\widetilde{d_k^S})^{1000} =& < \frac{t_k}{Q_k} >^{1000} -d_k^S - Q_T^{-1}\sum_{b=1}^{N\_cells\_500} l_{kb}^{500} s_b^{500} - \\ & \sum_{b=1}^{N\_cells\_500} l_{kb}^{500} s_b^{500} (\delta Q_b^{-1})^{1000,S}\end{aligned} \tag{A.21}$$

where $(\delta Q_b^{-1})^{1000,C}$ and $(\delta Q_b^{-1})^{1000,S}$ are the solutions obtained with the CN method and the SD method, respectively, for 1000 m side blocks and that where assigned to the N_cells_500 blocks of the 500 meters side crossed by the $k-th$ ray. For a resolution of 500 meters, the inversion problems become:

$$(\widetilde{d_k^{C,S}})^{1000} = \sum_{b=1}^{N\_cells\_500} G_{kb}^{500}[(\delta Q_b^{500})^{-1}]^{C,S} \tag{A.22}$$

where the superscript 500 stands for the step of the grid and the $(\delta Q_b^{500})^{-1}$ are the inverse variations with respect to the inverse quality factor of the 1000 m cube in which they are contained. The elements of the inversion matrix, G_{kb}^{500}, are the length of the $k-th$ ray segment in the 500-meters side $b-th$ block l_{kb}^{500} multiplied for his slowness s_b^{500}:

$$G_{kb}^{500} = l_{kb}^{500} s_b^{500}. \tag{A.23}$$

For P-waves, only the blocks crossed by at least $n_R = 4$ rays ($f_C = 6\ Hz$) and $n_R = 8$ rays ($f_C = 15\ Hz$) are considered (see formula (A.15)). Formula (A.15) leads us to consider only the blocks crossed by at least $n_R = 6$ rays ($f_C = 6\ Hz$) and $n_R = 15$ rays ($f_C = 15\ Hz$) for S-waves. The inversion is linear and the average of the $(\delta Q_b^{500})^{-1}$ can be constrained as zero. The inverse quality factor of each 500 m block b for P-waves or S-waves is given by:

$$(Q_b^{500})^{-1} = Q_{PT,ST}^{-1} + (\delta Q_b^{1000})^{-1} + (\delta Q_b^{500})^{-1} \tag{A.24}$$

while the percentage reduction is 80% in residual.

Bibliography

Abercrombie, R. E., 1995, Earthquake source scaling relationships from -1 to 5 ML using seismograms recorded at 2.5 km depth, *J. Geoph. Res.* **100**, 24015–24036.

Abubakirov, I. R. and Gusev, A. A., 1990, Estimation of scattering properties of lithosphere of Kamchatka based on Monte-Carlo simulation of record envelope of a near earthquake, *Phys. Earth Planet. Inter.* **64**, 52–67.

Aki, K., 1969, Analysis of the seismic coda of local earthquakes as scattered waves, *J. Geophys. Res.* **74**, 615–631.

Aki, K., 1980a, Attenuation of shear-waves in the lithosphere for frequencies from 0.05 to 25 Hz, *Phys. Earth Planet. Inter.* **21**, 50–60.

Aki, K., 1980b, Scattering and attenuation of shear waves in the lithosphere, *J. Geophys. Res.* **85**, 6496–6504.

Aki, K., 1982, Scattering and attenuation, *Bull. Seismol. Soc. Am.* **72**, S319–S330.

Aki, K. and Chouet, B., 1975, Origin of coda waves: Source, Attenuation, and Scattering Effects, *J. Geophys. Res.* **80**, 3322–3342.

Aki, K. and Ferrazzini, V., 2000, Seismic monitoring and modeling of an active volcano for prediction, *J. Geophys. Res.* **105**, 16617–16640.

Aki, K. and Richards, P., 1980, Quantitative Seismology - Theory and Methods, W. H. Freeman, San Francisco.

Al-Shukri, H. J. and Mitchell, B. J., 1990, Three-dimensional attenuation structure in and around the New Madrid seismic zone, *Bull. Seism. Soc. Am.* **80**(3), 615–632.

Anderson, D. L., Ben-Menahem, A., and Archambeau, C. B., 1965, Attenuation of seismic energy in the upper mantle, *J. Geoph. Res.* **70**(6), 1441.

Anderson, D. L. and Hart, R. S., 1978, Attenuation models of the Earth, *Phys. Earth Plan. Int.* **16**, 289–306.

Anderson, D. L. and Kovach, R. L., 1964, Attenuation in the mantle and rigidity of the core from multiply reflected core phases, *Proc. Nat. Acad. U. S.* pp. 168–172.

Anderson, J. G. and Hough, S. E., 1984, A model for the shape of the Fourier spectrum of accelleration at high frequecies, *Bull. Seism. Soc. Amer.* **74**, 1969–1993.

Anderson, L., 1964, The Anelasticity of the Earth, *Science* **144**(3618), 559.

Andronico, D., Calderoni, G., Cioni, R., Sbrana, A., Suplizio, R., and Santacroce, R., 1995, Geological map of Somma-Vesuvius Volcano, *Per. Mineral.* **64**, 77–78.

Aster, R., Borchers, B., and Thurber, C., 2005, Parameter Estimation and Inverse Problem, Vol. 90 of *International Geophysics Series*, Elsevier.

Aster, R. and Meyer, R., 1988, Three dimensional velocity structure and hypocenter distribution in the Campi Flegrei caldera, Italy, *Tectonophysics* **149**, 195–218.

Aster, R., Meyer, R., Natale, G. D., Martini, M., Pezzo, E. D., Iannaccone, G., and Scarpa, R.: 1989, Seismic investigation of the Campi Flegrei: a synthesis and summary of results, *in* K. Aki, P. Gasparini, and R. Scarpa (eds), *Volcanic Seismology, Proc. Volc. series III*, Springer-Verlag, San Francisco.

Auger, E., Gasparini, P., Virieux, J., and Zollo, A., 2001, Seismic Evidence of an Extended Magmatic Sill Under Mt. Vesuvius, *Science* **294**, 1510–1512.

Badawy, A. and Fattah, A. K. A., 2001, Source parameters and fault plane determinations of the 28 December 1999 northeastern Cairo earthquakes, *Tectonophysics* **343**(1–2), 63–77.

Bai, C. and Greenhalgh, S., 2005, 3D multi-step travel time tomography: imaging the local, deep velocity structure of Rabaul volcano, Papua New Guinea, *Phys. of the Earth and Plan. Inter.* **151**, 259–275.

Bai, C. Y., 2004, Three-dimensional seismic kinematic inversion with application to reconstruction of the velocity structure of Rabaul volcano, Ph.d. dissertation, The University of Adelaide, Australia.

Barton, N., 2006, Rock Quality, Seismic Velocity, Attenuation and Anisotropy, CRC Press.

Battaglia, J., Troise, C., Obrizzo, F., Pingue, F., and Natale, G. D., 2006, Evidence of fluid migration as the source of deformation at Campi Flegrei caldera (Italy), *Geoph. Res. Lett.* **33**(L01307), doi:10.1029/2005GL024904.

Battaglia, J., Zollo, A., Virieux, J., and Iacono, D. D., 2008, Merging active and passive data sets in traveltime tomography: The case study of Campi Flegrei caldera (Southern Italy), *Geoph. Prosp.* **56**, 555–573.

Benz, H., Chouet, B. A., Dawson, P. B., Lahr, J. C., Page, R. A., and Hole, J. A., 1996, Three-dimensional P and S wave velocity structure of Redoubt Volcano, Alaska, *J. Geoph. Res.* **101**, 8111–8128.

Berrino, G., Coppa, U., Natale, G. D., and Pingue, F., 1993, Recent geophysical investigation at Somma–Vesuvius volcanic complex, *J. Volcanol. Geotherm. Res.* **58**, 239–262.

Berrino, G., Corrado, G., Luongo, G., and Toro, B., 1984, Ground deformation and gravity changes accompanying the 1982 Pozzuoli uplift, *Bull. Volc.* **47**, 183–200.

Bianco, F., Castellano, M., Milano, G., Ventura, G., and Vilardo, G., 1997, The Somma-Vesuvius stress field induced by regional tectonics: evidences from seismological and mesostructural data, *J. Volcanol. Geotherm. Res* **82**, 199Ű–218.

Bianco, F., Castellano, M., Pezzo, E. D., and Ibanez, J. M., 1999, Attenuation of short period seismic waves at Mt. Vesuvius, Italy, *Geophys. J. Int.* **138**, 67Ű–76.

Bianco, F., Pezzo, E. D., Castellano, M., Ibanez, J. M., and Luccio, F. D., 2002, Separation of intrinsic and scattering seismic attenuation in the Southern Apennine zone, Italy, *Geophys. J. Int.* **150**(1), 10Ű–22.

Bianco, F., Pezzo, E. D., Malagnini, L., Luccio, F. D., and Akinci, A., 2005, Separation of depth-dependent intrinsic and scattering seismic attenuation in the northeastern sector of the Italian Peninsula, *Geophys. J. Int.* **161**(1), 130Ű–142.

Bijwaard, H., Spakman, W., and Engdahl, E. R., 1998, Closing the gap between regional and global travel time tomography, *J. Geophys. Res.* **103**(B12), 30055Ű–30078.

Biswas, N. N. and Aki, K., 1984, Characteristics of coda waves: Central and south central Alaska, *Bull. Seism. Soc. Am.* **74**, 493–507.

Bleistein, N., 1984, Mathematicals methods for wave phenomena, Academic Press, New York.

Block, L. V., 1991, Joint hypocenter–velocity inversion of local earthquake arrival time data in two geothermal regions, Ph.d. dissertation, Massachusetts Institute of Technology, Cambridge.

Boatwright, J., 1980, A spectral theory fo circular seismic sources: simple estimates of source dimension, dynamic stress drop and radiated energy, *Bull. Seismol. Soc. Am.* **70**, 1–27.

Bonafede, J. and Mazzanti, M., 1998, Modeling gravity variations consistent with ground deformation in the Campi Flegrei caldera, Italy, *J. of Volc. and Geoth. Res.* **81**, 137–157.

Bonasia, V., Pezzo, E. D., Pingue, F., Scandone, R., and Scarpa, R., 1985, Eruptive history, seismic activity and ground deformations at Mt. Vesuvius, Italy, *Ann. Geophys.* **3**, 395–406.

Bourbie, T., 1985, Intrinsic Attenuation of Seismic Waves. Part Two: Theory and Models Oil and Gas Science and Technology, *Oil and Gas Science and Technology – Rev. IFP* **40**(1), 15–32.

Boyd, S. and Xiao, L., 2005, Least–Squares Covariance Matrix Adjustment, *SIAM Journal on Matrix Analysis and Applications* **27**(2), 532–546.

Brenguier, F., Shapiro, N. M., Campillo, M., Ferrazzini, V., Duputel, Z., Coutant, O., and Nercessian, A., 2008, Towards forecasting volcanic eruptions using seismic noise, *Nature Geoscience* **January**, doi :10.1038/ngeo104.

Brenguier, F., Shapiro, N. M., Campillo, M., Nercessian, A., and Ferrazzini, V., 2007, 3-D surface wave tomography of the Piton de la Fournaise volcano using seismic noise correlations, *Geoph. Res. Lett.* **34**(L02305), doi:10.1029/2006GL028586.

Brennan, B. J.: 1981, Linear viscoelastic behaviour in rocks, *Anelasticity in the Earth*, AGU Geodynamic Series 4, pp. 13–22.

Brennan, B. J. and Stacey, F. D., 1977, Frequency dependence of elasticity of rock–test of seismic velocity dispersion, *Nature* **268**, 220–222.

Caliro, S., Chiodini, G., Moretti, R., Avino, R., Granieri, D., Russo, M., and Fiebig, J., 2007, The origin of the fumaroles of La Solfatara (Campi Flegrei, South Italy), *Geoch. et Cosm. Acta* **71**, 3040–3055.

Campillo, M. and Paul, A., 2003, Long–Range Correlations in the Diffuse Seismic Coda, *Science* **299**, 547–549.

Cao, A. and Romanowicz, B., 2004, Hemispherical transition of seismic attenuation at the top of the earth's inner core, *Earth Plan Scie. Lett.* **228**, 243–253.

Capuano, P., Gasparini, P., Zollo, A., Virieux, J., Casale, R., and Yeroyanni, M., 2003, The internal structure of Mt. Vesuvius, Liguori, Napoli.

Chatterjee, S. N., Pitt, A. M., and Iyer, H. M., 1985, Vp/Vs ratios in the Yellowstone National Park region, Wyoming, *J. Volcanol. Geotherm. Res.* **26**, 213–230.

Chernov, L. A., 1960, Wave Propagation in a Random Medium, McGraph–Hill, New–York.

Cherveny, V., 2001, Seismic ray theory, Cambridge University Press, Cambridge.

Chiao, L. Y. and Kuo, B. Y., 2001, Multiscale seismic tomography, *Geoph. J. Int.* **145**, 517–527.

Chiodini, G., Gasparini, P., Zollo, A., Virieux, J., Casale, R., and Yeroyanni, M., 2001, The internal structure of Mt. Vesuvius, Liguori, Napoli.

Chouet, B.: 1996, New methods and future trends in seismological volcano monitoring, *in* R. Scarpa and R. I. Tilling (eds), *Monitoring and Mitigation of Volcano Hazards*, Springer, Berlin, pp. 23–97.

Chouet, B., 2003, Volcano Seismology, *Pageoph* **160**, 739–788.

Christensen, N. I., 1996, Poisson's ratio and crustal seismology, *J. Geoph. Res.* **101**, 3139–3156.

Cioni, R., Santacroce, R., and Sbrana, A.: 1994, Polyphased collapse of the Somma–Vesuvius caldera, *Volcano instability on the Earth and other planets*, Geol. Soc. London.

Coleman, T. F. and Li, Y., 1992, A reflective Newton method for minimizing a quadratic function subject to bounds on some of the variables, *SIAM J. Optim.* **6**, 1040–1058.

Cormier, V. F. and Li, X., 2002, Frequency-dependent seismic attenuation in the inner core 2. A scattering and fabric interpretation, *J. Geoph. Res.* **107**(B12), doi:10.1029/2002JB001796.

Corrado, G., Guerra, I., Bascio, A. L., Luongo, G., and Rampoldi, R., 1976, Inflation and microearthquake activity at Phlegrean Fields, Italy, *Bull. Volc.* **40**, 1Ű–20.

D'Antonio, M., Civetta, L., Orsi, G., Pappalardo, L., Piochi, M., Carandente, A., de Vita, S., Vito, M. A. D., and Isaia, R., 1999, The present state of the magmatic system of the Campi Flegrei caldera based on a reconstruction of its behavior in the past 12 ka, *J. of Volc. and Geoth. Res.* **91**, 247–268.

De Gori, P., Chiarabba, C., and Patanè, D., 1999, Qp structure of Mount Etna: Constraints for the physics of the plumbing system, *J. of Geoph. Res.* **110**(B05303), doi:10.1029/2003JB002875.

De Lorenzo, S., Gasparini, P., Mongelli, F., and Zollo, A., 2001a, Thermal state of the Campi Flegrei Caldera inferred from seismic attenuation tomography, *J. Geodynamics* **32**, 476–486.

De Lorenzo, S., Zollo, A., and Mongelli, F., 2001b, Source parameters and three-dimensional attenuation structure from the inversion of microearthquake pulse width data: Qp imaging and inferences on the thermal state of the Campi Flegrei caldera (southern Italy), *J.Geophys. Res.* **106**, 16265–16286.

De Natale, G., Capuano, P., Troise, C., and Zollo, A., 1998, Seismicity at Somma-Vesuvius and its implications for the 3D tomography of the volcano, *J. Volcanol. Geotherm. Res., Special Issue Vesuvius* **82**, 175–197.

De Natale, G., Iannaccone, G., Martini, M., and Zollo, A., 1987, Seismic Sources and Attenuation Properties at the Camppi Flegrei Volcanic Area, *Pageoph* **125**(6).

De Natale, G., Troise, C., Pingue, F., Mastrolorenzo, G., and Pappalardo, L., 2006, The Somma–Vesuvius volcano (Southern Italy): Structure, dynamics and hazard evaluation, *Earth Sci. Rev.* **74**, 73–111.

De Siena, L., Pezzo, E. D., and Bianco, F.: submitted to JGR, Campi Flegrei seismic attenuation image: evidences of gas resevoirs, hydrotermal basins and feeding systems.

De Siena, L., Pezzo, E. D., Bianco, F., and Tramelli, A., 2008, Multiple resolution seismic attenuation imaging at Mt. Vesuvius, *Phys. Earth Plan. Int.* **doi:10.1016/j.pepi.2008.10.015**.

Del Pezzo, E., 2008, Seismic wave scattering in volcanoes, Vol. 50 of *Advances in Geophysics*, Academic Press, chapter 13.

Del Pezzo, E., Bianco, F., De Siena, L., and Zollo, A., 2006a, Small scale shallow attenuation structure at Mt. Vesuvius, *Phys. Earth Planet. Interiors* **157**, 257–268.

Del Pezzo, E., Bianco, F., and Saccorotti, G., 2001, Separation of intrinsic and scattering Q for volcanic tremor: an application to Etna and Masaya Volcanoes, *Geoph. Res. Lett.* **28**(16), 3083–3086.

Del Pezzo, E., Bianco, F., and Saccorotti, G., 2004, Seismic source dynamics at Vesuvius volcano, Italy, *J. Volcanol. Geotherm. Res.* **133**, 23–39.

Del Pezzo, E., Bianco, F., and Zaccarelli, L., 2006b, Separation of Qi and Qs from passive data at Mt. Vesuvius: A reappraisal of the seismic attenuation estimates, *Phys. Earth Planet. Interiors* **159**, 202–212.

Del Pezzo, E., Martino, S. D., Parrinello, M., and Sabbarese, C., 1993, Seismic site amplification factors in Campi Flegrei, Southern Italy, *Phys. Earth Planet. Interiors* **78**, 105–117.

Del Pezzo, E., Simini, M., and Ibanez, J., 1996, Separation of intrinsic and scattering Q for volcanic areas: a comparison between Etna and Campi Flegrei, *J. Volcanol. Geoth. Res.* **70**, 213–219.

Derode, A., Larose, E., Tanter, M., de Rosny, J., Tourin, A., Campillo, M., and Fink, M., 2003, Recovering the Green's function from field-field correlations in an open scattering medium (L), *J. Acous. Soc. Am.* **113**(6), 2973–2976.

Di Maio, R., Mauriello, P., Patella, D., Petrillo, Z., Piscitelli, S., and Siniscalchi, A., 1998, Electric and electromagnetic outline of the Mount Somma Vesuvius structural setting, *J. Volcanol. Geotherm. Res.* **82**, 219–238.

Di Vito, M. A., Isaia, R., Orsi, G., Southon, J., de Vita, S., D'Antonio, M., Pappalardo, M., and Piochia, L. M., 1999, Volcanism and deformation since 12,000 years at the Campi Flegrei caldera (Italy), *J. Volc. Geotherm. Res.* **91**, 221–246.

Di Vito, M. A., Lirer, L., Mastrolorenzo, G., and Rolandi, G., 1987, The Monte Nuovo eruption (Campi Flegrei, Italy), *Bull. of Volc.* **49**, 608–615.

Dziewonski, A. M., 1979, Elastic and anelastic structure of the earth, *Geophys. Space Phys.* **17**, 303–312.

Eberhart-Phillips, D., 1990, Three-dimensional P and S velocity structure in the Coalinga region, California, *J. Geophys. Res.* **95**, 15343–15363.

Eberhart-Phillips, D., Reyners, M., Chadwick, M., and Chiu, J. M., 2005, Crustal heterogeneity and subduction processes: 3–D VP, VP/VS and Q in the southern North Island, New Zealand, *Geophys. J. Int.* **162**, 270–288.

Evans, J. R. and Zucca, J. J., 1993, Active source, high-resolution (NeHT) tomography: velocity and Q, Chapman and Hall, pp. 695–732.

Fedi, M., Florio, G., and Rapolla, A., 1998, 2D modelling of Somma Vesuvius structure by aeromagnetic data, *J. Volcanol. Geotherm. Res.* **82**, 239–247.

Fehler, M. C., Hoshiba, M., Sato, H., and Obara, H., 1992, Separation of scattering and intrinsic attenuation for the Kanto-Tokai region, Japan, using mesurements of S-wave energy versus hypocentral distance, *Geophys. J. Int.* **108**, 787–800.

Frankel, A. and Clayton, R. W., 1986, Finite difference simulations of seismic scattering Implications for the propagation of short-period seismic waves in the crust and models of crustal heterogeneity, *J. Geophys. Res.* **91**, 6465–6489.

Frankel, A. and Wennerberg, L., 1987, Energy-flux model of seismic coda: separation of scattering and intrinsic attenuation, *Bull. Seismol. Soc. Am.* **77**, 1223–1251.

Fuchs, K., 1997, Upper Mantle Heterogeneities from Active and Passive Seismology, Springer.

Futterman, W. I., 1962, Dispersive Body Waves, *J. Geoph. Res.* **67**, 5279–5291.

Gaeta, S. G., Natale, G. D., Peluso, F., Mastrolorenzo, G., Castagnolo, D., Troise, C., Pingue, F., Mita, G., and Rossano, S., 1998, Genesis and evolution of unrest episodes at Campi Flegrei caldera: the role of thermal fluid-dynamical processes in the geothermal system, *J. of Geoph. Res.* **103**, 20921–20933.

Galluzzo, D., Pezzo, E. D., Maresca, R., Rocca, M. L., and Castellano, M.: 2005, Site effects estimation and source-scaling dynamics for local earthquakes at Mt. Vesuvius, Italy, *Congress acts ESG2006, Grenoble.* 36.

Gao, L. S., Lee, L. C., Biswas, N. N., and Aki, K., 1983, Comparison of the effects between single and multiple sacttering on coda waves for local earthquakes, *Bull. Seismol. Soc. Am.* **73**, 377–389.

Giampiccolo, E., Gresta, S., and Rasconà, F., 2004, Intrinsic and scattering attenuation from observed seismic codas in Southeastern Sicily (Italy), *Phys. Earth Plan. Int.* **145**, 55–66.

Gotsman, J., Rymer, H., and Berrino, G., 2006, Unrest at the Campi Flegrei caldera (Italy): A critical evaluation of source parameters from geodetic data inversion, *J. of Volc. and Geoth. Res.* **150**, 132–145.

Gubbins, D., 2004, Time series analysis and inverse theory for geophysicists, Cambridge University Press, Cambridge.

Gudmundsson, Ó., Finlayson, D. M., Itikarai, I., Nishimura, Y., and Johnson, W. R., 2004, Seismic attenuation at Rabaul volcano, Papua New Guinea, *J. of Volc. and Geoth. Res.* **130**, 77–92.

Gung, Y. and Romanowicz, B., 2004, Q tomography of the upper mantle using three component long–period waveforms, *Geoph. J. Int.* **157**(2), 813–830.

Gusev, A. A. and Abubakirov, I. R., 1996, Simulated envelopes of non-isotropically scattered body waves as compared to observed ones: Another manifestation of fractal heterogeneity, *Geophys. J. Int.* **127**, 49–60.

Gusev, A. A. and Abubakirov, I. R., 1999, Vertical profile of effective turbidity reconstructed from broadening of incoherent body-wave pulses, *Geophys. J. Int.* **136**, 309–323.

Haberland, C. and Rietbrock, A., 2001, Attenuation tomography in the western central Andes: A detailed insight into the structure of a magmatic arc, *J. Geophys. Res.* **106**(B6), 11151–11167.

Hansen, S., Thurber, C. H., Mandernach, M., Haslinger, F., and Doran, C., 2004, Seismic Velocity and Attenuation Structure of the East Rift Zone and South Flank of Kilauea Volcano, Hawaii, *Bull. Seismol. Soc. Am.* **94**, 1430–1440.

Heinz, D. L. and Jeanloz, R., 1983, Inhomogeneity parameter of a homogeneous Earth, *Nature* **301**, 138–139.

Herraiz, M. and Espinosa, A. F., 1987, Coda waves: a review, *PAGEOPH* **125**, 499–577.

Ho-Liu, P., Kanamori, H., and Clayton, R. W., 1988, Applications of attenuation tomography to Imperial Valley and Coso-Indian Wells region, southern California, *J. Geoph. Res.* **93**(B9), 10501–10520.

Hong, T. K. and Wu, R. S., 2005, Scattering of elastic waves in geometrically anisotropic random media and its implication to sounding of heterogeneity in the Earth's deep interior, *Geoph. J. Int.* **163**(1), 324–338.

Hoshiba, M., 1991, Simulation of multiple–scattered coda wave excitation based on the energy conservation law, *Phys. Earth Planet. Inter.* **67**, 123–136.

Hoshiba, M., 1993, Separation of scattering attenuation and intrinsic absorption in Japan using the multiple lapse time window analysis of full seismogram envelope, *J. Geophys. Res.* **98**, 15809–15824.

Hoshiba, M., 1995, Estimation of nonisotropic scattering in western Japan using coda wave envelopes: Application of a multiple nonisotropic scattering model, *J. Geophys. Res.* **100**, 645–657.

Imanishi, K., Ellsworth, W. L., and Prejean, S. G., 2004, Earthquake source parameters determined by the SAFOD Pilot Hole seismic array, *Geoph. Res. Lett.* **31**(L12S09), 10.1029/2004GL019420.

Ishimaru, A., 1997, Wave Propagation and Scattering in Random Media, The IEEE/OUP Series on Electromagnetic Wave Theory, second edn, Oxford University Press and IEEE Press, Oxford.

Ito, H., Vilbiss, J. D., and Nur, A., 1979, Compressional and shear waves in saturated rock during water–steam transition, *J. Geophys. Res.* **84**, 4731–4735.

Iyer, H. M. and Dawson, P. B., 1993, Imaging volcanoes using teleseismic tomography, Chapman and Hall, pp. 466–392.

Jackson, D. D. and Anderson, D. L., 1970, Physical mechanisms of seismic wave attenuation, *Rev. Geophys. Space Phys.* **8**, 1–63.

Jackson, I., 1998, Elasticity, composition and temperature of the Earth's lower mantle: a reappraisal, *Geoph. J. Int.* **134**(1), 291–311.

Jackson, I. and Paterson, M. S., 1993, A High–pressure, High–temperature Apparatus for Studies of Seismic Wave Dispersion and Attenuation, *PAGEOPH* **141**(2–3–4).

Jacobson, R. S., 1987, An investigation into the fundamental relationships between attenuation, phase dispersion, and frequency using seismic refraction profiles over sedimentary structures, *Geophysics* **52**, 72–87.

Jin, A. and Aki, K., 1986, Temporal change in coda Q before the Tangshan earthquake of 1976 and the Haicheng earthquake of 1975, *J. Geophys. Res.* **96**, 18215–18231.

Jin, A., Mayeda, K., Adams, D., and Aki, K., 1994, Separation of intrinsic and scattering attenuation in southern California using TERRAscope data, *J. Geophys. Res.* **99**, 17835–17848.

Johnston, D. H.: 1981, Attenuation: A state-of-the-art summary, *in* M. N. Toksoz and D. H. Johnston (eds), *Seismic Wave Attenuation*, SEG reprint series No. 2, pp. 123–139.

Julian, B. R., Ross, A., Foulger, G. R., and Evans, J. R., 1996, Three-dimensional seismic image of a geothermal reservoir: The Geysers, California, *Geoph. Res. Lett.* **23**, 685–688.

Karato, S. B. K., 2001, Origin of lateral variation of seismic wave velocities and density in the deep mantle, *J. Geoph. Res.* **106**(B10), 21771–21784.

Kern, H., 1982, Elastic-wave velocity in crustal and mantle rocks at high pressure and temperature: the role of the high-lowquartz transition and of dehydration reactions, *Phys. of the Earth and Plan. Int.* **29**, 12–23.

Kinoshita, S., 1994, Frequency-dependent attenuation of shear waves in the crust of the southern Kanto area, Japan, *Bull. Seism. Soc. Am.* **84**(5), 1387–1396.

Knopoff, L., 1964, Q, *Rev. Geophys.* **2**(4), 625–660.

Kovach, R. L. and Anderson, L., 1964, Attenuation of shear waves in the upper and lower mantle, *Bull. seism. Soc. Am.* **54**(6A), 1855–1864.

La Rocca, M., Del Pezzo, E., Simini, M., Scarpa, R., and De Luca, G., 2001, Array analysis of seismograms for explosive sources: evidence for surface waves scattered at the main topographical features, *Bull. Seismol. Soc. Am.* **91**, 219–231.

Lawson, C. L. and Hanson, R. J., 1974, Solving Least Square Problems, Prentice-Hall, Englewood Cliffs, New Jersey.

Lay, T. and Wallace, T. C., 1995, Modern Global Seismology, Academic Press.

Lees, J. M. and Crosson, R. S., 1989, Tomographic inversion for threedimensional velocity structure at Mount St. Helens using earthquake data, *J. Geophys. Res.* **94**, 5716Ű5728.

Lees, J. M. and Lindley, G. T., 1994, Three-dimensional Attenuation Tomography at Loma Prieta: Inverting t* for Q, *J. Geophys. Res.* **99**(B4), 6843–6863.

Lerche, I. and Menke, W., 1986, An inversion method for separating apparent and intrinsic attenuation in layered media, *Geophys. J. R. Astron. Soc.* **87**, 333–347.

Li, B., Qin, J., Qian, X., and Ye, J., 2002, The coda attenuation of the Yao'an area in Yunnan Province, *Act. Seis. Sin.* **17**, 47–53.

Li, X. and Cormier, V. F., 2002, Frequency-dependent seismic attenuation in the inner core 1. A viscoelastic interpretation, *J. Geoph. Res.* **107**(B12), 10.1029/2002JB001795.

Lomax, A., Zollo, A., Capuano, P., and Virieux, J., 2001, Precise, absolute earthquake location under Somma Vesuvius volcano using a new three dimensional velocity model, *Geophys. J. Int.* **146**, 313–331.

Malagnini, L., Mayeda, K., Akinci, A., and Bragato, P. L., 2004, Estimating absolute site effects, *Bull. Seism. Soc. Am.* **94**, 1343–1352.

Malick, J., 2005, A Dual Approach to Semidefinite Least–Squares Problems, *SIAM Journal on Matrix Analysis and Applications* **26**(1), 272–284.

Margaris, B. N. and Boore, D. N., 1998, Determination of ?? and ?? from Response Spectra of Large Earthquakes in Greece, *Bull. of the Seism. Soc.* **88**, 170–182.

Margerin, L., 2006, Attenuation, transport and diffusion of scalar waves in textured media, *Tectonophysics* **416**, 229–244.

Margerin, L., Campillo, M., and Tiggelen, B. V., 1998, Radiative transfer and diffusion of waves in a layered medium: New insight into coda Q, *Geophys. J. Int.* **134**, 596–612.

Marianelli99, P., Mt’etrich, N., and Sbrana, A., 1999, Shallow and deep reservoirs involved in magma supply of the 1944 eruption of Vesuvius, *Bull. Volcanol.* **61**, 48–63.

Matsumoto, S., 1995, Characteristics of Coda Waves and Inhomogeneity of the Earth, *Geophys. J. Int.* **67**, 101–108.

Matsunami, K., 1991, Laboratory tests of excitation and attenuation of coda waves using 2-D models of scattering media, *Phys. Earth Planet. Inter.* **67**, 36–47.

Mayeda, K., Koyanagi, S., and Aki, K., 1991, Site amplification from S-wave coda in the Long Valley Caldera region, California, *Bull. Seism. Soc. Am.* **81**, 2194–2213.

Mayeda, K., Koyanagi, S., Hoshiba, M., Aki, K., and Zeng, Y., 1992, A comparative study of scattering, intrinsic and coda Q for Hawaii, Long Valley, and Central California between 1.5 and 15.0 Hz, *J. Geophys. Res.* **97**, 6643–6659.

Mayeda, K. and Walter, W. R., 1996, Moment, energy,stress drop and source spectra of western United States earthquakes from regional coda envelopes, *J. Geophys. Res.* **101**, 11195–11208.

Menke, W., 1984, Geophysical Data Analysis: Discrete Inverse Theory, Academic Press.

Mitchell, B. J., 2005, Anelastic Structure and Evolution of the Continental Crust and Upper Mantle From Seismic Surface Wave attenuation, *Rev. Geoph.* **33**(4), 441–462.

Mulargia, F. and Tinti, S., 1985, Seismic sample areas defined from incomplete catalogues; an application to the Italian territory, *Phis. Earth Plan. Int.* **40**, 273–300.

Nakajima, J. and Hasegawa, A., 2003, Tomographic imaging of seismic velocity structure in and around the Onikobe volcanic area, northeastern Japan: implications for fluid distribution, *J. of Volc. and Geoth. Res.* **127**, 1–18.

Nakamura, Y., 1970, Seismic energy transmission in an intensively scattering medium, *J. Geophys. Res.* **43**, 389–399.

Newton, R. C., 1989, Metamorphic fluids inthe deep crust, *Annu. Rev Earth Plan. Sci.* **17**, 385–412.

Niazi, M. and Johnson, L. R., 1992, Q in the inner core, *Phys. Earth Plan. Int.* **74**, 55–62.

Nishigami, K., 1991, A new invertion method of coda waveforms to determine spatial distribution of coda scatterers in the crust and uppermost mantle, *Geophys. Res. Lett.* **12**(18), 2225–2228.

Nishigami, K., 2006, Crustal Heterogeneity in the Source Region of the 2004 Mid Niigata Prefecture Earthquake: Inversion Analysis of Coda Envelopes, *Pure Appl. Geophys.* **163**, 601–616.

Ordaz, M. and Singh, S. K., 1992, Source spectra and spectral attenuation of seismic waves from Mexican earthquakes, and evidence of amplification in the hill zone of Mexico City, *Bull. Seism. Soc. Am.* **82**(1), 24–43.

Orsi, G., Vita, S. D., and Vito, M. D., 1996, The restless resurgent Campi Flegrei caldera (Italy): constraints on its evolution and configuration, *J. Volcanol. Geoth. Res.* **74**, 179–214.

Paasschens, J. C. L., 1997, Solution of the time-dependent Boltzmann equation, *Phys. Rew.* **56**(1), 1135–1141.

Patanè, D., Barberi, G., Cocina, O., Gori, P. D., and Chiarabba, C., 2006, Time-Resolved Seismic Tomography Detects Magma Intrusions at Mount Etna, *Science* **313**, 821–823.

Petrosino, S., Siena, L. D., and Pezzo, E. D., 2008, Recalibration of the Magnitude Scales at Campi Flegrei, Italy, on the basis of Measured Path and Site and Transfer Functions, *Bull. of the Seism. Soc. of Amer.* **98**(4), 1964–1974.

Phillips, W. S. and Aki, K., 1986, Site amplification of coda waves from local earthquakes in central California, *Bull. Seismol. Soc. Am.* **76**, 627–648.

Ponko, S. C. and Sanders, C. O., 1994, Inversion for P and S wave attenuation structure, Long Valley caldera, California, *J. Geophys. Res.* **99**(B2), 2619–2635.

Press, F., 1957, Rigidity of the Earth's core, *Science* **124**, 1204.

Pujol, W. S. and Aster, R., 1990, Joint hypocentral determination and the detection of low-velocity anomalies. An example from the Phlegrean Fields earthquakes, *Bull. Seismol. Soc. Am.* **80**(1), 129–139.

Quan, Y. and Harris, J. M., 1996, Seismic tomography using the frequency shift method, *Geophysics* **62**, 895–905.

Rautian, T. G. and Khalturin, V. I., 1978, The use of the coda for determination of the earthquake source spectrum, *Bull. Seismol. Soc. Am.* **68**, 923–948.

Rietbrock, A., 2001, P wave attenuation structure in the fault area of the 1995 Kobe earthquake, *J. Geoph. Res.* **106**, 4141–4154.

Romanowicz, B. and Durek, J. J., 2000, Seismological constrainyìts on attenuation in the earth: a review, *Geophys. Monog.* **117**, 161–179.

Romero, A. E. J., McEvilly, T. V., and Majer, E. L., 1997, 3–D microearthquake attenuation tomography at the Northwest Geysers geothermal region, California, *Geophysics* **62**, 149–167.

Roth, E. G., Wiens, D. A., Dorman, L. M., Hildebrand, J., and Webb, S. C., 1999, Seismic attenuation tomography of the Tonga-Fiji region using phase pair method, *J. Geophys. Res.* **104**(B3), 4795–4809.

Saccorotti, G., Petrosino, S., Bianco, F., Castellano, M., Galluzzo, D., Rocca, M. L., Pezzo, E. D., Zaccarelli, L., and Cusano, P., 2007, Seismicity associated with the 2004–2006 renewed ground uplift at Campi Flegrei Caldera, Italy, *Phys. Earth Plan. Int.* **165**, 14–24.

Sambridge, M. S. and Gudmundusson, O., 1998, Tomographic systems of equation with irregular cells, *J. Geophys. Res.* **103**, 773–781.

Sanders, C. O.: 1993, Local earthquake tomography: attenuation – theory and results, *in* H. M. Iyer and H. K. (eds), *Seismic Tomography: Theory and Practice*, Chapman and Hall.

Sanntacroce, R.: 1993, Somma–Vesuvius, *Technical report*, Quaderni di Ricerca Scientifica, CNR.

Sato, H., 1977, Energy propagation including scattering effects single isotropic scattering approximation, *J. Phys. Earth* **25**, 27–41.

Sato, H., 1995, Formulation of the multiple non-isotropic scattering process in 3-D space on the basis of energy transport theory, *Geophys. J. Int.* **121**, 523–531.

Sato, H. and Fehler, M. C., 1998, Seismic Wave Propagation and scattering in the heterogeneous earth, Springer and Verlag, New York.

Scandone, R., Bellucci, F., Kirer, L., and Rolandi, G., 1991, The structure of the Campanian Plain and the activity of the Napolitan volcanoes, *J. Volcanol. Geotherm. Res.* **48**, 1–31.

Scandone, R., Giacomelli, L., and Gasparini, P., 1993, Mt. Vesuvius: 2000 years of volcanological observations, *J. Volcanol. Geotherm. Res.* **58**, 5–26.

Scarpa, R., Tronca, F., Bianco, F., and Pezzo, E. D., 2002, High resolution velocity structure beneth Mount Vesuvius from seismic array data, *Geophys. Res. Lett.* **21**(29), 2040.

Scherbaum, F., 1990, Combined inversion for the Three-Dimensional Q Structure and Source Parameters Using Microearthquake Spectra, *J. Geophys. Res.* **95**(B8), 12423–12438.

Schmeling, H., 1985, Numerical models on the influence of partial melt on elastic, anelastic and electric properties of rocks. Part I: Elasticity and anelasticity, *Phys. Earth Planet. Inter.* **41**, 34–57.

Schurr, B., Asch, G., Rietbrock, A., Trumbull, R., and Haberland, C. H., 2003, Complex patterns of fluid and melt transport in the central Andean subduction zone revealed by attenuation tomography, *Earth and Plan. Scie. Lett.* **215**, 105–119.

Sengupta, M. K. and Rendleman, C. A., 1989, Case study: the importance of gas leakage in interpreting amplitude-versus-offset (AVO) analysis, *Soc. Explor. Geophys.* **59**, 848–850.

Shang, T. and Gao, L., 1988, Transportation theory of multiple scattering and its application to seismic coda waves of impulsive source, *Scientia Sinica (series B, China)* **31**, 1503–1514.

Shapiro, N. M., Singh, S. K., Iglesias-Mendoza, A., Cruz-Atienza, V. M., and Pacheco, J. F., 2000, Evidence of low Q below Popocatépetl volcano, and its implication to seismic hazard in Mexico City, *Geoph. Res. Lett.* **27**(17), 2753–2756.

Shearer, P. M., 1999, Introduction to Seismology, Cambridge University press, Cambridge.

Shito, A., Karato, S., and Park, J., 2004, Frequency dependence of Q in Earths upper mantle inferred from continuous spectra of body waves, *Geophys. Res. Lett.* **31**(L1), 2603.

Shon, J. H., 1996, Physical properties of rock: fundamentals and principles of petrophysics, Pergamon–Elsevier Science, Oxford.

Snieder, R., 2006, The theory of coda wave interferometry, *Pure Appl. Geophys.* **163**, 455–473.

Spencer, J., 1979, Bulk and shear attenuation in Berea sandstone: the effects of pore fluids, *J. of Geoph. Res.* **84**, 7521–7523.

Stacey, F. D., 1995, Theory of thermal and elastic properties of the lower mantle and core, *Phys. Earth Plan. Int.* **89**, 219–245.

Stacey, F. D., Gladwin, M. T., McKavanagh, B., Linde, A. T., and Hastic, L. M., 1975, Anelastic damping of acoustic and seismic pulses, *Geophys. Surv.* **2**, 133–157.

Stachnick, J. C., 2004, Seismic attenuation and mantle wedge temperatures in the Alaska subduction zone, *J. Geoph. Res.* **109**(B10304), doi: 10.1029/2004JB003018.

Su, F., Aki, K., and Biswas, N., 1991, Discriminating quarry blast from earthquakes using coda waves, *Bull. Seismol. Soc. Am.* **81**, 162–178.

Sudo, Y. and Kong, L. S. L., 2001, Three-dimensional seismic velocity structure beneath Aso Volcano, Kyushu, Japan, *Bull. of Volc.* **63**, 326–344.

Takei, Y., 2002, Effect of pore geometry on VP/VS: From equilibrium geometry to crack, *J. Geophys. Res.* **107**, doi:10.1029/2001JB000522.

Thurber, C. H.: 1987, Seismic structure and tectonics of Kilauea volcano Hawaii, *in* R. Decker, T. Wright, and P. H. Stauffer (eds), *Volcanism in Hawaii*, US Geological Survey, pp. 919–934.

Tichelaar, B. and Ruff, L. R., 1989, How good are our best models?, *EOS* **70**, 593Ű–606.

Todesco, M., Chiodini, G., and Macedonio, G., 2003, Monitoring and modelling hydrothermal fluid emission at La Solfatara (Phlegrean Fields, Italy). An interdisciplinary approach to the study of diffuse degassing, *J. of Volc. and Geotherm. Res.* **125**, 57–79.

Tondi, R. and Franco, R. D., 2003, Three-dimensional modeling of Mount Vesuvius with sequential integrated inversion, *J. Geophys. Res.* **108**(B5), 2256.

Tramelli, A., 2008, Elastic propagation in random media: applications to the imaging of volcano structures, Ph.d. thesis, Graduate school of Science, Bologna University.

Tramelli, A., Pezzo, E. D., Bianco, F., and Boschi, E., 2006, 3D scattering image of the Campi Flegrei caldera (Southern Italy). New hints on the position of the old caldera rim, *Phys. Earth Planet. Interiors* **155**, 269–280.

Tsujiura, M., 1978, Spectral analysis of the coda waves from local earthquakes, *Bull. Earthquake Res. Inst., Tokyo Univ.* **53**, 1–48.

Um, J. and Thurber, C. H., 1987, A fast algorithm for two-point seismic ray tracing, *Bull. Seismol. Soc. Am.* **77**, 972–986.

Vanorio, T., Virieux, J., Capuano, P., and Russo, G., 2005, Three-dimensional tomography from P wave and S wave microearthquake travel times and rock physics characterization of the Campi Flegrei Caldera, *J. Geoph. Res.* **110**(B03201), doi:10.129/2004JB003102.

Vanorio, T., Virieux, J., and Latorre, D.: 2008, Pore pressure prediction based on passive seismic and rock physics modeling, *in* W. Marzocchi and A. Zollo (eds), *Conception, verification and application of innovative techniques to study active volcanoes*, Istituto Nazionale di Geofisica e Vulcanologia, pp. 321–334.

Vesnaver, A., 1996, Irregular grids in seismic tomography and minimum-time ray tracing, *Geophys. J. Int.* **126**, 147–165.

Villaseñor, A., Benz, H. M., Filippi, L., Luca, G. D., Scarpa, R., Patané, G., and Vinciguerra, S., 1998, Three-dimensional P-wave velocity structure of Mt. Etna, Italy, *Geophys. Res. Lett.* **25**, 1975–1978.

W., H., 1756–1794, Philosophycal transactions, Royal Society, London.

Walck, M., 1988, Three-dimensional Vp/Vs variations for the Coso region, California, *J. Geophys. Res.* **93**, 2047–Ű2052.

Wang, C. Y., Wang, W. T., and Shi, Y., 1989, Thermal evolution of a rift basin: The Tyrrhenian Sea, *J. Geophys. Res.* **94**, 3991–Ű4006.

Warren, L. M. and Shearer, P. M., 2002, Mapping lateral variations in upper mantle attenuation by stacking P and PP spectra, *J. Geophys. Res.* **105**(B11), 25391–Ű25402.

Watanabe, T. and Sassa, K., 1996, Seismic attenuation tomography and its application to rock mass evaluation, *Int. J. Rock Mech. Min. Sci. and Geomech* **33**(5), 467–Ű477.

Weaver, R. L., 1990, Diffusivity of ultrasound in polycrystals, *J. Mech. Phys. Solids* **1**(38), 55–Ű86.

Weaver, R. L. and Lobkis, O. I., 2006, Diffuse fields in ultrasonic and seismology, *Geophysics* **71**(4), doi:10.1190/1.2212246.

Wegler, U., 2003, Analysis of Multiple Scattering at Vesuvius Volcano, Italy, Using Data of the TomoVes active seismic experiment, *J. Volcanol. Geotherm. Res.* **128**, 45–63.

Wegler, U., 2004, Diffusion of seismic waves in a thick layer: Theory and application to Vesuvius volcano, *J. Geophys. Res.* **109**, B07303.

Wegler, U. and Luhr, B. G., 2001, Scattering behaviour at Merapi Volcano (Java) revealed from an active seismic experiment, *Geophys. J. Int.* **145**, 579–592.

Wei, C. and Muraleetharan, K. K., 2007, Linear viscoelastic behaviour of porous media with non-uniform saturation, *Int. J. Engin. Sci.* **45**, 698–715.

Wen, L. and Niu, F., 2002, Seismic velocity and attenuation structures in the top of the Earth's inner core, *J. Geoph. Res.* **107**(B11), 10.1029/2001JB000170.

Wu, H. and Lees, J. M., 1996, Attenuation structure of Coso Geothermal Area, California, from wave pulse widths, *Bull. Seism. Soc. Am.* **86**, 1574–1590.

Wu, R. S., 1985, Multiple scattering and energy transfer of seismic waves - Separation of sacttering effect for intrinsic attenuation, I, *Geophys. J. R. Astron. Soc.* **82**, 57–80.

Wu, R. S. and Aki, K., 1988, Introduction: Seismic wave scattering in three-dimensionally heterogeneous Earth, *PAGEOPH* **128**, 1–6.

Yoshimoto, K., 2000, Monte Carlo simulation of seismogram envelopes in scattering media, *J. Geophys. Res.* **B3**(105), 6153–6162.

Yoshimoto, K. and Jin, A.: 2008, Coda Energy Distribution and Attenuation, *in* R. Dmowska, H. Sato, and M. Fehler (eds), *Earth Heterogeneity and Scattering Effects of Seismic Waves*, Academic Press.

Yoshimoto, K., Sato, H., and Ohtake, M., 1993, Frequency-dependent attenuation of P and S waves in the Kanto area, Japan, based on the codanormalization method, *Geophys. J. Int.* **114**, 165–Ű174.

Zeng, Y., 1991, Compact solution for multiple scattered wave energy in time domain, *Bull. Seismol. Soc. Am.* **81**, 1022–1029.

Zeng, Y., 1996, Scattered surface wave energy in the seismic coda, *Pure Appl. Geophys.* **163**, 533–548.

Zeng, Y., Su, F., and Aki, K., 1991, Scattering wave energy propagation in a random isotropic scattering medium I. Theory, *J. Geophys. Res.* **96**, 607–619.

Zollo, A., Capuano, P., and Corciulo, M., 2006, Geophysical Exploration of the Campi Flegrei (Southern Italy) Caldera Interiors: Data, Methods and Results, GNV.

Zollo, A., D'Auria, L., Matteis, R. D., andJ. Virieux, A. H., and Gasparini, P., 2002, Bayesian estimation of 2-D P-velocity models from active seismic arrival time data: imaging of the shallow structure of Mt Vesuvius (Southern Italy), *Geophys. J. Int.* **151**, 566–582.

Zollo, A., Gasparini, P., Virieux, J., le Meur, H., de Natale, G., Biella, G., Boschi, E., Capuano, P., de Franco, R., dell'Aversana, P., de Matteis, R., Guerra, I., Iannaccone, G., Mirabile, L., and Vilardo, G., 1996, Seismic Evidence for a Low–Velocity Zone in the Upper Crust Beneath Mount Vesuvius, *Science* **274**, 592–594.

Zollo, A., Judenherc, S., Auger, E., D'Auria, L., Virieux, J., Capuano, P., Chiarabba, C., de Franco, R., Makris, J., Michelini, A., and Musacchio, G., 2003, Evidence for the buried rim of Campi Flegrei caldera from 3-d active seismic imaging, *Geophys. Res. Lett.* **30**(19), doi:10.1029/2003GL018173.

Zollo, A., Maercklin, N., Vassallo, M., Iacono, D. D., Virieux, J., and Gasparini, P., 2008, Seismic reflections reveal a massive melt layer feeding Campi Flegrei caldera, *Geophys. Res. Lett.* **35**(L112306), doi:10.1029/2008GL034242.

Zucca, J. J., Hutchings, L. J., and Kasameyer, P. W., 1994, Seismic velocity and attenuation structure of the Geysers Geothermal Field, California, *Geothermics* **23**, 111–126.